LA-14346

From Model Conception to Verification and Validation, A Global Approach to Multiphase Navier-Stoke Models with an Emphasis on Volcanic Explosive Phenomenology

Los Alamos
NATIONAL LABORATORY
EST. 1943

This work was supported by the Yucca Mountain Project at Sandia National Laboratories.

Los Alamos National Laboratory, an affirmative action/ equal opportunity employer, is operated by Los Alamos National Security, LLC, for the National Nuclear Security Administration of the U.S. Department of Energy under contract DE-AC52-06NA25396.

LA-14346
Issued: October 2007

From Model Conception to Verification and Validation, A Global Approach to Multiphase Navier-Stoke Models with an Emphasis on Volcanic Explosive Phenomenology

Sébastian Dartevelle

Los Alamos
NATIONAL LABORATORY
EST. 1943

Table of Contents

Figures and Tables

Abstract

Large-scale volcanic eruptions are hazardous events that cannot be described by detailed and accurate *in situ* measurement: hence, little to no real-time data exists to rigorously validate current computer models of these events. In addition, such phenomenology involves highly complex, nonlinear, and unsteady physical behaviors upon many spatial and time scales. As a result, volcanic explosive phenomenology is poorly understood in terms of its physics, and inadequately constrained in terms of initial, boundary, and inflow conditions. Nevertheless, code verification and validation become even more critical because more and more volcanologists use numerical data for assessment and mitigation of volcanic hazards.

In this report, we evaluate the process of model and code development in the context of geophysical multiphase flows. We describe: (1) the conception of a theoretical, multiphase, Navier-Stokes model, (2) its implementation into a numerical code, (3) the verification of the code, and (4) the validation of such a model within the context of turbulent and underexpanded jet physics. Within the validation framework, we suggest focusing on the key physics that control the volcanic clouds—namely, momentum-driven supersonic jet and buoyancy-driven turbulent plume. For instance, we propose to compare numerical results against a set of simple and well-constrained analog experiments, which uniquely and unambiguously represent each of the key-phenomenology.

Key words: plinian column; multiphase turbulent plumes; underexpanded jets; Mach disk; verification, validation.

1. Introduction

A large-scale explosive volcanic eruption cloud is one of the most enthralling yet hazardous phenomenon one can witness in Nature (Figure 1). Such catastrophic events potentially pose a major threat to human life, livestock, the environment at large, and aircraft safety. They can also potentially disrupt all social and economic activities for many years after the eruption.

Figure 1

Ascending eruption cloud from Redoubt Volcano as viewed to the west from the Kenai Peninsula, Alaska, USA. The mushroom-shaped plume rose from pyroclastic flows that cascaded down the north flank of the volcano (Photograph from R. Clucas, April 21, 1990).

Typically, volcanic clouds consist of hot magmatic fragments and lithic clasts dispersed in a carrying gas phase. Initially, this hot multiphase mixture is expelled subvertically from a volcanic vent at speeds up to a few hundred of seconds and with densities greater than the surrounding atmosphere (i.e., negative buoyancy). As this momentum-driven jet thrusts upwards into the atmosphere, it expands, hence dilutes itself and decreases its own bulk density with respect to the ambient atmosphere. Consequently, the jet becomes a buoyancy-driven turbulent

plume [*Valentine, 1998; Dartevelle et al., 2004; Dartevelle, 2005*]. The exact fate of this buoyant plume will be controlled by a balance between three major forces, viz., (1) the buoyancy force, which pulls the cloud upward to higher altitudes, (2) the gravity force, which exerts a downward pull, and (3) turbulence, which has an overall dissipative effect on the clouds and slows it down (this is often characterized as the "atmospheric drag" effect). In addition to the natural dissipative effects, turbulence may also have important supplementary nonlinear effects upon the rising plume. For instance, turbulence causes important entrainment of atmospheric "fresh" ambient into the volcanic dusty cloud. As such, turbulence further dilutes the flow, which potentially increases its buoyancy; yet, at the same time, turbulence entrains colder air into the cloud, which decreases the buoyancy of the plume with respect to the atmospheric ambient [Dartevelle et al., 2004]. Other nonlinear feedbacks may control the final fate of the rising plume. For instance, the thrust-jet at the bottom of the plume is fundamentally controlled by shock dynamic (i.e., like an underexpanded jet), which in turn controlled the expansion dynamic of the multiphase jet and plume (i.e., rate of cooling and dilution) and hence offering a mighty control upon the buoyancy balance of the whole plume [*Dartevelle et al., 2004*]. At the end, either the plume further rises to higher altitudes till it exhausts its excess of buoyancy and, then, radially spreads like a gigantic mushroom (the cloud is named "plinian"), or the plume is not buoyant and, eventually, collapses back to the ground forming destructive high-velocity hot ash-and-gas avalanches propagating around the volcano (these avalanches are named "pyroclastic" flows and surges) [*Valentine and Wohletz, 1989; Druitt, 1998; Dartevelle et al., 2004; Dartevelle, 2005*]. The whole phenomenology can last from a few minutes to a few hours and covers spatial scales from a few kilometers to tens of kilometers (Figure 1).

Since the pioneer work of volcanologists from Los Alamos National Laboratory (LANL) [*Wohletz et al., 1984; Valentine and Wohletz, 1989; Valentine et al., 1991*], multiphase codes and supercomputer simulations have been used more and more often to capture the whole volcanic phenomenology [e.g., *Dobran et al., 1993; Neri et al., 2003; Oberhuber et al., 1998; Dartevelle et al., 2004; Suzuki et al., 2005*]; yet with little evidence that the produced numerical results accurately and correctly capture the physics of these eruptions. So far, numerical "Verification and Validation" (V&V) in volcanology tends to be more qualitative [e.g., *Dartevelle and Valentine, 2007*] rather than to be truly quantitative, as one would expect.

However, because of the enormous scale of these volcanological events and their often destructive and lethal nature, only indirect, remote methods (e.g., satellites, remote sensors, photography, and acoustic-pressure sensors) can be used to infer some information about the dynamic and physical properties. Consequently, little is known about the exact dynamics of these gigantic volcanic clouds and there is insufficient real-time data that can be accurately used to validate computer codes [*Dartevelle et al., 2004; Dartevelle and Valentine, 2007*]. Yet, more and more often, these codes and numerical results are used for assessing volcanic hazards and for mitigating the associated volcanic risks [e.g., *Todesco et al., 2002; Esposti et al., 2002; Dartevelle and Valentine, 2005*]. Without any rigorous quantitative V&V studies, one may question the intrinsic value of such "unverified and "invalidated" numerical studies. V&V analyses are therefore needed; not only would volcanologists gain more confidences in their newly developed numerical tools, but would also be empowered to better convince policymakers of the usefulness of their approaches to mitigate potential volcanic hazards.

Verifying and validating codes within this specific volcanic contest is possible if one recognizes the key physics that dominates and controls the dynamics of these clouds, viz., (1) expansion and development of supersonic jets, and (2) development of turbulence within multiphase jets and plumes [*Valentine, 1998; Dartevelle, 2005*]. In a typical plinian cloud, the lower, thrusting, momentum-driven part has all the properties of underexpanded jets expanding into the atmosphere [*Kieffer and Sturtevant, 1984; Valentine, 1998*]; while the upper, turbulent, buoyantly-driven part is controlled by the atmospheric drag and the dissipation is induced by multiphase turbulence [*Dartevelle, 2005*]. As a matter of fact, the physics of underexpanded jets [e.g., *Ladenburg et al., 1949; Lewis and Carlson, 1964; Kieffer and Sturtevant, 1984*] and multiphase turbulent jets [e.g., *Hishida et al., 1987; Violet et al., 1992*] is well known and documented with accurate measurements to be used for validation purposes.

Our challenge is therefore threefold: (1) to describe the process of conceptualizing a physically sound multiphase Navier-Stokes model for geophysical flows, (2) to implement this conceptual model into a multiphase computer code, and (3) to formalize with a geophysical perspective the verification and validation (V&V) analysis given the conceptual model, its implementation into a

code, and the set of physics aimed to be simulated. Hence, this manuscript is organized as follows:

First, in §2, we thoroughly describe the process of conceptualizing a physically sound multiphase Navier-Stokes model for geophysical flows following *Dartevelle* [*2005*]. Then, in §3, we describe the numerical implementation of such a theoretical model into an open-source computer code, GMFIX. GMFIX codes (Geophysical Multiphase Flow with Interphase eXchange, v1.62) is a set of multiphase-Computational Fluid Dynamic (CFD) Fortran codes, which have been recently redeveloped from [*Dartevelle, 2004; Dartevelle et al., 2004*] initial work to meet the strict Quality Assurance (QA), verification, and validation requirements from the Office of Civilian Radioactive Waste Management (OCRWM) and the Yucca Mountain Project (YMP) of the U.S. Department of Energy (DOE) [*Dartevelle, 2006a,b*]. GMFIX is a Los Alamos National Laboratory (LANL) code derived from the MFIX project managed by the National Energy Technology Laboratory and Oak Ridge National Laboratory (http://www.mfix.org) [*Syamlal et al., 1993; Syamlal, 1998*], itself derived from an earlier LANL code, KFIX [*Rivard and Torrey, 1979*]. Finally, in §4, we explore the formal process of "gaining confidence" in numerical results, known as the "Verification and Validation" or, simply, "V&V" analysis. The verification process aims to verify to "correctness" of the implementation of the model into the GMFIX codes, i.e., to demonstrate that the conceptual model is correctly solved by the code. The validation process aims to demonstrate that the model and its implementation is suitable for "correctly" solving the physics of interests (e.g., multiphase turbulence, shock dynamics) in explosive volcanology, i.e., to demonstrate the "correct" problem is being solved by the code.

In the following, all operators, tensors, invariants, and symbols in this manuscript are thoroughly defined in Appendix B & C. The sign convention for stress is such that it follows the same convention as Fick and Fourier laws [*Bird et al., 1977; Dartevelle, 2004, 2005*]. In other words, viscous stress is positive in the direction of decreasing velocities. Hence compressive stress, compressive strain, and their rates are taken positive. Unless specified otherwise, vectors (e.g., $\mathbf{q}$, $\mathbf{y}$, $\mathbf{u}$) and tensors (e.g., $\mathbf{T}$, $\boldsymbol{\tau}$) are denoted in bold, while scalar functions (e.g., ρ, ε, T, y) are noted with normal fonts. Appendix A provides a description of the multiphase turbulence model applied to a two-phase flow system.

2. *Phase 1* – The conception of a geophysical multiphase fluid dynamic model

Since most of geophysical multiphase systems of interest are made up of a large number of particles, it is impractical to solve the motion of each individual particle; hence GMFIX model [*Dartevelle, 2006a,b*] is based upon the Implicit Multi-Field formalism (IMF) which treats all phases in the system as interpenetrating continua. Each instantaneous local point variable (mass, velocity, temperature, pressure, etc.) must be treated in a way to acknowledge the fact that any given arbitrary volume can be shared by different phases at the same time. This treatment may involve, for instance, an "averaging" or a "smoothing" process [*Dartevelle, 2004; Dartevelle 2005*]. The process of deriving a *single-phase* Navier-Stokes system of Partial Differential Equations into a *multiphase* system is a critical task, particularly when multiphase turbulence must be accounted for. However, even though the Navier-Stokes model may be well-known and accepted for a single phase, it remains far from clear what would be the final resulting form of the Navier-Stokes equations to model different interpenetrated phases altogether. In other words, the Navier-Stokes Partial Differential Equations must be somehow conceptualized furthermore to account for the multiphase nature of the system under consideration. We have chosen to follow the *single* to *multi*phase methodologies of *Dartevelle* [*2005*] because it leads to a final multiphase Navier-Stokes model compatible with different approaches to turbulence, viz., Reynolds Average Navier-Stokes (RANS) or Large Eddy Simulation (LES) and, at the same time, this model fulfills the second law of thermodynamic and the necessary requirements for a well-posed initial-value problem.

Let the i^{th} phase *function of presence*, $X_i(\mathbf{x},t)$, at location $\mathbf{x}$ and at time t be [*Drew 1983*]:

$$X_i(\mathbf{x},t) = \begin{cases} 1 & \text{if location } \mathbf{x} \text{ is inside phase i at time t,} \\ 0 & \text{otherwise} \end{cases} \quad (1)$$

Hence, in a two-phase gas-solid flow system of interests for this manuscript, we must have $X_g=1-X_s$. In addition to being a unique material identifier, X_i has some important properties [*Drew 1983; Lhuillier 1996; Drew and Passman 1999*].

First Property

$$\nabla X_i = -\mathbf{n}_i \delta_{Int} \quad , \tag{2}$$

where $\mathbf{n}_i$ is a unit normal vector pointing outward to the i^{th} phase at the location $\mathbf{x}$ and time t. The gradient of the phase function must be zero everywhere except exactly at the interface between phases. This gradient vector points towards the direction of maximum increase that is towards phase i itself in a direction opposite to $\mathbf{n}_i$. Obviously, at location $\mathbf{x}$ and time t in a two-phase flow, we have $\nabla X_g = -\nabla X_s$, or more generally, $\sum_{i=1}^{n} \nabla X_i = 0$. In Eq. (2), δ_{Int} is Dirac delta function at the interface location as it directly results from the step-like behavior of the interface as seen in Eq. (1). Hence, δ_{Int} acts as a function of presence of the interface itself (it is zero at any location where there is no interface).

The gradient in Eq. (2) can be used to sort out mass, molecular, and heat fluxes (and their directions) at the interface between gas and solid phases. Indeed, let us use an "angular operator," $\langle\rangle$, which will be thoroughly defined in the next sections (within RANS, it will be an ensemble averaged operator; within LES, it will be a filter operator). Ensemble-averaging or filtering Eq. (2), we have

$$\begin{aligned} \left\langle \nabla X_i \right\rangle &= \left\langle -\mathbf{n}_i \delta_{Int} \right\rangle \\ &= \nabla \left\langle X_i \right\rangle = \nabla \varepsilon_i \end{aligned} \quad , \tag{3}$$

where ε_i is a "bulk" volumetric concentration of phase i. Clearly, the product of any property ϕ with the gradient of the phase function, e.g., $\left\langle \phi_i \nabla X_i \right\rangle$, must give a bulk contributory effect of fluxes of ϕ of phase i at its "bulk" interface over the whole domain of integration. By definition, in a two-phase system at location $\mathbf{x}$ and time t, we must have $\nabla \varepsilon_g = -\nabla \varepsilon_s$, or more generally, $\sum_{i=1}^{n} \nabla \varepsilon_i = 0$.

Second Property

The volumetric concentration of the interfacial area, A_i, can be defined as the "angular operator" upon the scalar product of $\mathbf{n}_i$ and ∇X_i :

$$A_i = \left\langle -\mathbf{n}_i \cdot \nabla X_i \right\rangle \tag{4}$$

Again, the angular operator may be either an ensemble-averaged operator (RANS) or a filter operator (LES). Clearly, in a system made of two phases (gas and solid) at location **x** and time t, we have $A_s=A_g$.

Third Property

$$\begin{aligned} &\frac{\partial X_i}{\partial t} + \mathbf{u}_{Int} \cdot \nabla X_i = 0 \\ &\Leftrightarrow \frac{\partial X_i}{\partial t} = \mathbf{u}_{Int} \cdot \mathbf{n}_i \delta_{Int} \end{aligned} \quad , \tag{5}$$

where $\mathbf{u}_{Int}$ is the velocity of the interface between phases. Eq. (5) indicates that the material (Lagrangian) derivative of X_i is always nil ($\frac{dX_i}{dt} = 0$) no matter where it occurs. Indeed, being exactly at the interface and moving with its local velocity ($\mathbf{u}_{Int}$), X_i represents a *constant* jump and Eq. (5) must equal zero [*Lhuillier 1996*]. Being at any a location other than the interface, either $X_i=1$ (inside the material) or $X_i=0$ (outside the material), and therefore all the partial derivatives (time and space) must vanish [*Drew and Passman 1999*]. This result, of course, justifies the second line of Eq. (5) because the transient term of X_i ($\frac{\partial X_i}{\partial t}$) must vanish at any location except when an interface crosses that specific location.

Fourth Property

In a multiphase flow made of two and only two phases, the interface is straightforward to define (e.g., between the solid particles and the gas phase). In a mixture made of n phases (n>2), one must distinguish n-1 interfaces separating each phase from the other. Let us write the function of

presence of interfaces in Eq. (2) between phase i and j as $\delta_{Int,i,j}$ where $i \neq j$; then the function of presence of *all interfaces between all phases* in the system is

$$\delta_{Int} = \sum_{i=1}^{n-1} \sum_{j=i+1}^{n} \delta_{Int,i,j} \tag{6}$$

And the function of presence of the interface between *phase i only and all the other phases* in the system is

$$\delta_{Int,i} = \sum_{\substack{j=1 \\ j \neq i}}^{n} \delta_{Int,i,j} \tag{7}$$

Hence each phase's interface can be easily tracked without any confusion between different interfaces of different phases. With these new definitions, $\mathbf{u}_{Int}$ in Eq. (5) would represent a "bulk mean" interfacial velocity of *all interfaces between all phases* making up the multiphase system.

In order to properly manipulate the multiphase Navier-Stokes equations within different turbulence frameworks (RANS and LES), we must define a mathematical operator that must own *at least* the three following properties [*Dartevelle, 2005*]:

Conservation of constant

Let c be a constant, then

$$\langle c \rangle = c \tag{8}$$

Linearity

Let α and β be scalars, vectors, or tensors, then

$$\langle \alpha + \beta \rangle = \langle \alpha \rangle + \langle \beta \rangle \tag{9}$$

Commutativity with respect to derivations

Let 'ι' be either a space (x) or time (t) variable. Let α be a scalar, vector, or tensor, then

$$\left\langle \frac{\partial \alpha}{\partial \iota} \right\rangle = \frac{\partial \left\langle \alpha \right\rangle}{\partial \iota} \qquad . \tag{10}$$

As we will see hereafter, the commutativity property is guaranteed within the RANS framework but required some discussions and further work within LES. Generally speaking and unlike the RANS angular operator, a LES angular operator is not a Reynolds operator. This is an important difference between LES and RANS, leading to a different Navier-Stokes set of equations (see a complete discussion on this in *Dartevelle* [*2005*]).

2.1. Definition of the RANS operator ⟨⟩

Let $\phi(\mathbf{x},t)$ be an instantaneous local (microscopic) fluid property at some specific punctual position **x** in space and at time t (ϕ can be a scalar, vector, or tensor). Let us achieve N identical experiments (replicas) with the same initial and boundary conditions. For each replica, we systematically measure at the same location **x** and time t the property $\phi(\mathbf{x},t)$. Of course, we may expect to measure slightly different values of $\phi(\mathbf{x},t)$ in each of these experiments. However, our prime interest is to capture a *bulk* property of the system or an *averaged* value of $\phi(\mathbf{x},t)$, which would be a "macroscopic" characteristic value for the whole ensemble of experiments. This ensemble average over the N replicas is

$$\left\langle \phi(\mathbf{x},t) \right\rangle = \begin{cases} \lim\limits_{N\to\infty} \sum\limits_{n=1}^{N} \phi_n(\mathbf{x},t)\, P_n \\ \int\limits_{-\infty}^{\infty} \phi(\mathbf{x},t)\, f(\phi)\, d\phi \end{cases} , \tag{11}$$

where $\phi_n(\mathbf{x},t)$ is the n^{th} realization of $\phi(\mathbf{x},t)$ with an observed probability P_n (if each realization of ϕ is equiprobable, then $P_n = 1/N$); the product $f(\phi)\cdot d\phi$ is the element of probability of observing a

given specific realization of ϕ (f is the probability density function of ϕ). Both definitions (sum *vs*. integral) are strictly identical depending on whether $\phi(\mathbf{x},t)$ is seen as a continuous or discrete random function.

Other averaging methods are possible, such as volume-averaged, which is performed *around* a fixed point **x** at time t, or the time-averaged, which is performed at the location **x** in a *time interval* around t. However, in many instances, time and volume average may be seen as a special case of the ensemble average. For instance, if the flow is homogenous (on the average, the flow is uniform in all directions) and stationary (on the average, the flow does not vary with time), time, volume, and ensemble are just identical averages (i.e., the ergodicity hypothesis).

The ensemble average of the function of presence of a given phase, X_i, must give the probability of presence of the i^{th} phase at **x** and t as it represents the averaged occurrence of phase i:

$$\varepsilon_i = \left\langle X_i(\mathbf{x},t) \right\rangle = \int_{-\infty}^{+\infty} X_i(\mathbf{x},t)\, dF(X_i) \quad . \tag{12}$$

If the spatial distribution of phase i is homogenous within the Control Volume, then ε_i can be seen as the volumetric concentration of the i^{th} phase. We may now define the phasic bulk density:

$$\hat{\rho}_i = \varepsilon_i \overline{\rho}_i = \left\langle X_i(\mathbf{x},t)\ \rho_i(\mathbf{x},t) \right\rangle \quad , \tag{13}$$

where the ensemble-averaged density of the i^{th} phase is weighted by the ensemble-averaged phasic function of presence, i.e.,

$$\overline{\rho}_i = \frac{\left\langle X_i(\mathbf{x},t)\ \rho_i(\mathbf{x},t) \right\rangle}{\left\langle X_i(\mathbf{x},t) \right\rangle} = \frac{\left\langle X_i(\mathbf{x},t)\ \rho_i(\mathbf{x},t) \right\rangle}{\varepsilon_i} = \frac{1}{\varepsilon_i} \int_{-\infty}^{\infty}\int_{-\infty}^{\infty} X_i(\mathbf{x},t)\ \rho_i(\mathbf{x},t)\, dF(X_i,\rho_i) \quad , \tag{14}$$

where ρ_i is the microscopic density of the i^{th} phase (for the solid phase, it will be assumed to be constant).

2.2. Definition of the LES operator $\langle\rangle$

A key idea of LES is the separation of the simulated large-scale properties of the flow from the modeled (subgrid, SG) small-scale properties. The limit (or cutoff) between large scales and subgrid scales is "supposed" to take place in the inertial subrange. This decomposition is obtained using a spatial filter with a characteristic width, ξ, equal to (or of the order of) the computational mesh-size or using a temporal filter with a characteristic time, τ, equal to (or of the order of) the time interval.

As previously, let $\phi(\mathbf{x},t)$ be an instantaneous local (microscopic) fluid property at some specific punctual position $\mathbf{x}$ in space and at time t. The LES space- and time-filtering process of ϕ is formally defined as [*Sagaut 1998*]:

$$\left\langle \phi(\mathbf{x},t) \right\rangle = \int_{-\infty}^{\infty}\int_{-\infty}^{\infty}\int_{-\infty}^{\infty}\int_{0}^{\infty} G(\xi,\tau)\,\phi(\mathbf{x}',t')\;dt'd\mathbf{x}' \quad , \tag{15}$$

where the spatial integration is produced over the entire flow domain, Ω (or any of its subdomains of constant grid-size), at any time. Eq. (15) filters $\phi(\mathbf{x},t)$ at a point $\mathbf{x}=\mathbf{x}'$ (spatial filtering), and at a time t=t' (time filtering) and weights $\phi(\mathbf{x},t)$ by $G(\xi,\tau)$. In mathematics, this process is called the "mollification" of $\phi(\mathbf{x},t)$. Eq. (15) defines a "regulariser" or "mollifier" [*Galdi 1994*]. The filter kernel, $G(\xi,\tau)$, is defined by its spatial width ξ, $\xi=\mathbf{x}-\mathbf{x}'$, over which the smoothing process takes place and by its time interval τ, $\tau=t-t'$ during which the filtering process occurs. It can be seen that for the most commonly used spatial filters (e.g., box, Gaussian, or spectral filters), G is centered in ξ, symmetric around ξ, and keeping the same shape in space as $\mathbf{x}'$ varies (see *Dartevelle* [*2005*]).

The filter kernel, $G(\xi,\tau)$, has a few key properties, such as (i) being normalized to preserve the constants, (ii) being obtained by tensorizing two kernels in space, $G_x(\xi)$ in $\Re^3$, and in time, $G_t(\tau)$

in $\Re$, and (iii), at the limit of ξ and τ going to zero, Eq.(15) becomes a Dirac delta sequence function (see *Dartevelle* [*2005*] for further details). In LES engineering and single-flow atmospheric literatures, it is far more common to use a spatial filter rather than a time filter because it separates spatial scales (large *vs*. subgrid) with obvious ease. This is formally expressed as $\lim_{\tau\to 0} G_x(\xi)\, G_t(\tau) = G_x(\xi)\,\delta(\tau)$. It should be kept in mind that whenever a spatial filtering is achieved, an implicit time filtering is achieved as well [*Sagaut 1998*], which imposes supplementary conditions over the time step of any LES simulations [*Dartevelle*, *2005*].

The spatial-filtering of X_i must give the filtered occurrence of phase i at some cutoff-scale over the whole domain Ω,

$$\varepsilon_i = \left\langle X_i(\mathbf{x},t)\right\rangle = \iiint_{\Omega} G_x(\xi)\, X_i(\mathbf{x}',t)\, d\mathbf{x}' \quad , \tag{16}$$

where ε_i is now the filtered volumetric concentration of the i^{th} phase. Hereafter in this manuscript, we will not make any symbolic difference between the volumetric concentrations obtained by an ensemble averaging (RANS) or by a filtering (LES) process. The filtered phasic bulk density is

$$\hat{\underset{\smile}{\rho}}_i = \varepsilon_i \bar{\underset{\smile}{\rho}}_i = \left\langle X_i(\mathbf{x},t)\ \rho_i(\mathbf{x},t)\right\rangle \quad , \tag{17}$$

where the bottom "smile" symbol is used to emphasize that the variable has been filtered (instead of being averaged as in RANS). The filtered density of the i^{th} phase is weighted by the filtered phasic function of presence,

$$\bar{\underset{\smile}{\rho}}_i = \frac{\left\langle X_i(\mathbf{x},t)\ \rho_i(\mathbf{x},t)\right\rangle}{\left\langle X_i(\mathbf{x},t)\right\rangle} = \frac{\left\langle X_i(\mathbf{x},t)\ \rho_i(\mathbf{x},t)\right\rangle}{\varepsilon_i} = \frac{1}{\varepsilon_i}\iiint_{\Omega} G_x(\xi)\left(X_i(\mathbf{x}',t)\,\rho_i(\mathbf{x}',t)\right) d\mathbf{x}' \ , \tag{18}$$

where ρ_i is the microscopic density of the i^{th} phase.

Although, we have formally reviewed the filtering operation within LES, one should be careful of filtering LES with nonhomogenous explicit spatial filters as reviewed by *Dartevelle* [*2005*]. Such filters are common and easy to use, but may pose a serious problem to the *commutativity with respect to derivations* property. One easy fix is to only use perfectly homogenous spatial filter upon the whole computational domain.

2.3. RANS and LES Favre Decompositions

Within the RANS framework, each time an idealized experiment is achieved, we may measure deviations (fluctuations) between the calculated ensemble average over all the experiments and the instantaneous local variable measured at position **x** and t. As we are mostly interested in the bulk flow, the approach of taking the ensemble average of each variable in the system is fully justified. However, the ensemble-averaged value of a given variable and its factual instantaneous local value may differ. Hence, it becomes critical to "properly" recover the lost information during the averaging process that will be supplied by a RANS model. Each instantaneous local variable, $\phi(\mathbf{x},t)$, is split into an ensemble-averaged part ($\overline{\phi}$ or $\tilde{\phi}$) and a fluctuating part (ϕ' or ϕ'') using two different Favre decompositions (density-weighted and volumetric concentration-weighted) [*Favre, 1965*]. Within the LES framework, a formal scale separation by means of filter functions is achieved between the anisotropic large scales and the more isotropic small scales. The filtering process between scales can be achieved either in space (spatial filter, the most common approach) or in time (temporal filter). Each instantaneous local variable, $\phi(\mathbf{x},t)$, is split into a filtered (or resolved, simulated) part ($\underset{\sim}{\overline{\phi}}$ or $\underset{\sim}{\tilde{\phi}}$) and an unresolved (or unfiltered within the subgrid) part ($\underset{\sim}{\phi'}$ or $\underset{\sim}{\phi''}$) that needs to be modeled. The same two kinds of Favre decompositions used in RANS—mass-weighted and phasic-weighted [*Favre 1965*]— complete this decomposition. The unresolved part can be seen as all the fluctuations caused by, for instance, turbulence within the subgrid. In this manuscript, and within the LES framework only, all Favre decompositions are noted by a "smile" symbol under the variable (e.g., $\underset{\sim}{\overline{\phi}}, \underset{\sim}{\tilde{\mathbf{u}}}, \underset{\sim}{\overline{\rho}}, \underset{\sim}{\overline{\mathbf{T}}}, \ldots$).

The Favre *phasic*-weighted decompositions are given:

$$\phi_i = \begin{cases} \overline{\phi}_i + \phi_i' & \text{RANS framework} \\ \underset{\frown}{\phi}_i + \underset{\frown}{\phi}_i' & \text{LES framework} \end{cases} . \tag{19}$$

Within the RANS framework, the prime stands for the fluctuating part and the horizontal bar stands for the mean part obtained from the Favre *phasic*-weighted ensemble averaging. Within the LES framework, the horizontal bar stands for the resolved (the filtered field that is simulated), while the prime stands for the unresolved subgrid (residual) field (that needs to be modeled). The phasic-weighted ensemble-averaged or filtered decompositions are given by:

$$\begin{cases} \overline{\phi}_i \\ \text{or} = \dfrac{\left\langle X_i(\mathbf{x},t)\,\phi_i(\mathbf{x},t)\right\rangle}{\left\langle X_i(\mathbf{x},t)\right\rangle} = \dfrac{\left\langle X_i(\mathbf{x},t)\,\phi_i(\mathbf{x},t)\right\rangle}{\varepsilon_i} \\ \underset{\frown}{\phi}_i \end{cases} . \tag{20}$$

Of course the operator ⟨⟩ is not the same for RANS, given by Eq.(11), and for LES, given by Eq.(15). The Favre mass-weighted decompositions are given by:

$$\phi_i = \begin{cases} \tilde{\phi}_i + \phi_i'' & \text{RANS framework} \\ \underset{\frown}{\tilde{\phi}}_i + \underset{\frown}{\phi}_i'' & \text{LES framework} \end{cases} , \tag{21}$$

where the double prime stands for the fluctuating (or unresolved residual) part and the tilde stands for the mean (or resolved) part. The Favre *mass*-weighted ensemble-averaged and filtered decompositions are:

$$\begin{aligned} \tilde{\phi}_i &= \frac{\left\langle X_i(\mathbf{x},t)\,\rho_i(\mathbf{x},t)\,\phi_i(\mathbf{x},t)\right\rangle}{\left\langle X_i(\mathbf{x},t)\,\rho_i(\mathbf{x},t)\right\rangle} = \frac{\left\langle X_i(\mathbf{x},t)\,\rho_i(\mathbf{x},t)\,\phi_i(\mathbf{x},t)\right\rangle}{\hat{\rho}_i} \\ \underset{\frown}{\tilde{\phi}}_i &= \frac{\left\langle X_i(\mathbf{x},t)\,\rho_i(\mathbf{x},t)\,\phi_i(\mathbf{x},t)\right\rangle}{\left\langle X_i(\mathbf{x},t)\,\rho_i(\mathbf{x},t)\right\rangle} = \frac{\left\langle X_i(\mathbf{x},t)\,\rho_i(\mathbf{x},t)\,\phi_i(\mathbf{x},t)\right\rangle}{\underset{\frown}{\hat{\rho}}_i} \end{aligned} . \tag{22}$$

On a cautious note [e.g., *Dartevelle, 2005*], within the LES framework, filtering a variable twice does not give the same results as the initial filtered variable, and filtering the unresolved subgrid (residual) field of the variable will not necessarily give a nil result. The consequence is that modeling subgrid fields (stress, heat flux, and so forth) will be more complicated than for the RANS approach [*Ferziger 1997*].

With all this in mind, it is now possible to derive in a "*one-step ensemble-averaging process*" (RANS) or in a "*one-step filtering process*" (LES) a full set of Navier-Stokes equations for all the phases in the system as demonstrated in *Dartevelle* [*2005*].

2.4. RANS and LES Hydrodynamic and Thermodynamic Model

It is therefore possible to derive hydrodynamic and thermodynamic models that would be able to accommodate both the Large-Eddy Simulation and Reynolds-Favre ensemble-averaged Navier-Stokes frameworks of turbulence. Of course, the constitutive equations for turbulent or subgrid phenomena (stress, dissipation, heat conduction, and so forth) and possibly the interfacial terms may differ.

In the following, we will not make any distinction between the LES and RANS symbols; however, we will retain the symbols for Favre *phasic*-weighted decomposition ($\overline{\phi}$), *mass*-weighted decomposition ($\tilde{\phi}$) variables, and their subsequent fluctuating or unfiltered parts, i.e., ϕ' or ϕ'', respectively. The equations are written in terms of the ensemble-averaged or filtered variable for each phase, where $\hat{\rho}$, $\tilde{\mathbf{u}}$, and $\tilde{y}$ pertain to averaged or filtered macroscopic density, velocity vector, and mass fraction. The indices 's' and 'g' are for the solid and gas phase. Because each phase is modeled as a continuum, they can be present at the same time in the same control volume, CV [*Harlow and Amsden 1975*]. Hence, we must distinguish the microscopic density of a particular material, ρ, from the macroscopic bulk density, $\hat{\rho}_i = \varepsilon_i \overline{\rho}_i$, where ε is the volumetric fraction of the phase under consideration and $\overline{\rho}_i$ is the phasic-averaged or filtered

density. Within any CV, we must have $\sum_{i=1}^{n} \varepsilon_i = 1$ for all n phases and for all m species of a given phase, $\sum_{j=1}^{m} y_j = 1$.

Phasic and Species Continuity

As an easy working example, let us derive a multiphase continuity PDE using the angular operator either within RANS or LES. To do so, we must start with the well-known continuity PDE for a *single*-phase system only (n=i=1):

$$\frac{\partial \rho_i}{\partial t} + \nabla \cdot \rho_i \, \mathbf{u}_i = 0 \quad . \tag{23}$$

In a multiphase system, we must modify this Eq.(23) to account for all the possible occupations by the different phases in the system anywhere and anytime (n > 1). Let us multiply Eq.(23) by the phasic function of presence, X_i:

$$X_i \left[\frac{\partial \rho_i}{\partial t} + \nabla \cdot \rho_i \mathbf{u}_i \right] = 0$$

$$\Leftrightarrow \frac{\partial X_i \rho_i}{\partial t} + \nabla \cdot X_i \rho_i \mathbf{u}_i = \rho_i \frac{\partial X_i}{\partial t} + \rho_i \mathbf{u}_i \cdot \nabla X_i$$

$$\Leftrightarrow \frac{\partial X_i \rho_i}{\partial t} + \nabla \cdot X_i \rho_i \mathbf{u}_i = \rho_i \left(\mathbf{u}_{Int} - \mathbf{u}_i \right) \cdot \mathbf{n}_i \delta_{Int}$$

With the angular operator, $\langle\rangle$, let us either ensemble-average (RANS) or spatially filtered (LES):

$$\left\langle \frac{\partial X_i \rho_i}{\partial t} + \nabla \cdot X_i \rho_i \mathbf{u}_i \right\rangle = \left\langle \rho_i \left(\mathbf{u}_{Int} - \mathbf{u}_i \right) \cdot \mathbf{n}_i \delta_{Int} \right\rangle$$

$$\Leftrightarrow \frac{\partial \left\langle X_i \rho_i \right\rangle}{\partial t} + \nabla \cdot \left\langle X_i \rho_i \mathbf{u}_i \right\rangle = R_i \quad ,$$

where R_i is the mass-production or mass-destruction rate of the i^{th} phase and must be specified in a specific context; δ_{Int} is the function of presence of all the interfaces. R_i must follow the jump condition, $\sum_{i=1}^{n} R_i = 0$. Knowing that $\left\langle X_i \rho_i \right\rangle = \hat{\rho}_i$ and that $\left\langle X_i \rho_i \mathbf{u}_i \right\rangle = \hat{\rho}_i \tilde{\mathbf{u}}_i$, the phasic continuity equation valid within both RANS and LES frameworks in a multiphase system must now read [*Dartevelle, 2005*]:

$$\frac{\partial \hat{\rho}_i}{\partial t} + \nabla \cdot \hat{\rho}_i \tilde{\mathbf{u}}_i = R_i \quad , \tag{24}$$

where, for instance, i=1 for the carrier, gas, phase and i≥2 for the dispersed phases.

Finally, in the case where one of the phases would be made up of different species (e.g., for the gas phase, dry air and water vapor), the species continuity for both RANS and LES framework is

$$\frac{\partial \hat{\rho}_i \tilde{y}_j}{\partial t} + \nabla \cdot \hat{\rho}_i \tilde{y}_j \tilde{\mathbf{u}}_i = -\nabla \cdot \hat{\rho}_i \left(\mathbf{y}_j + {}^{tur/SG}\mathbf{y}_j \right) + \varepsilon_i \bar{\Gamma}_j + C_{i,j} \quad , \tag{25}$$

where $\tilde{y}_j$ is the averaged or filtered mass fraction of the j^{th} species; $\bar{\Gamma}_j$ is the averaged/filtered mass source or sink rate because of chemical or physical processes between species; and $C_{i,j}$ is the interfacial species mass transfer rate and has two contributions, viz., one from the mass transfer between phases and one from the "diffusion" of the interface belonging to species j of the i^{th} phase. The latter contribution is very often ignored [*Syamlal et al., 1993; Veynante and Poinsot 1997*]; hence, in most circumstances, $C_{i,j}$ can be written as a simple function of mass transfer between phases, $C_{i,j} \approx \tilde{y}_j R_i$, with the mean jump condition between the m species of phase i and all other phases as $\sum_{i=1}^{n} \sum_{j=1}^{m} C_{i,j} = 0$. In Eq.(25), the species mass fraction flux has two contributions: one from the averaged or filtered flux (i.e., $\mathbf{y}_j$) and one from turbulence (RANS, ${}^{tur}\mathbf{y}_j$ or from the subgrid (LES, ${}^{SG}\mathbf{y}_j$) (see *Dartevelle* [*2005*] for a detailed formulation):

$$\mathbf{y}_j = \varpi \nabla \tilde{y}_j$$

$$^{tur}\mathbf{y}_j = \widetilde{y_j'' \mathbf{u}_i''} \qquad \text{RANS framework} \quad , \tag{26}$$

$$^{SG}\mathbf{y}_j = \left(\widetilde{\tilde{y}_j \tilde{\mathbf{u}}_i} - \tilde{y}_j \tilde{\mathbf{u}}_i \right) + \left(\widetilde{\tilde{y}_j \mathbf{u}_i''} + \widetilde{y_j'' \tilde{\mathbf{u}}_i} \right) + \left(\widetilde{y_j'' \mathbf{u}_i''} \right) \qquad \text{LES framework}$$

where ϖ is the molecular diffusion coefficient of species j in the mixture. It can be recognized in $^{SG}\mathbf{y}_j$, from left to right between parenthesis, the LES Leonard-, Cross-, and Reynolds-terms. Clearly, the turbulent contribution must be modeled within a specific context of turbulence (either RANS or LES).

Momentum

The phasic momentum equation within both RANS and LES frameworks must be [see justification in *Dartevelle, 2005*]:

$$\frac{\partial \hat{\rho}_i \tilde{\mathbf{u}}_i}{\partial t} + \nabla \cdot \hat{\rho}_i \tilde{\mathbf{u}}_i \tilde{\mathbf{u}}_i = -\nabla \cdot \varepsilon_i \left(\bar{\mathbf{T}}_i + {}^{tur/SG}\mathbf{T}_i \right) + \hat{\rho}_i \tilde{\mathbf{G}}_i + \mathbf{M}_i \tag{27}$$

where $\mathbf{M}_i$ is the interfacial momentum transfer rate between phases; $\tilde{\mathbf{G}}_i$ represents a body force (e.g., gravity); and $\bar{\mathbf{T}}_i$ and $^{tur/SG}\mathbf{T}_i$ are respectively the phasic mean/averaged stress and the Reynolds (RANS) or the subgrid (LES) stress tensors. As seen in *Dartevelle* [*2005*], $\mathbf{M}_i$ may be decomposed into a contribution from mass transfer between phases and a contribution from the interfacial forces at the interfaces (e.g., drag force, added mass forces, interfacial shear stress, and pressure), $\mathbf{M}_i = \bar{\mathbf{u}}_{Int} R_i + \bar{P}_{Int,i} \nabla \varepsilon_i + \bar{\boldsymbol{\tau}}_{Int,i} \cdot \nabla \varepsilon_i + \mathbf{M}_i^{drag}$, where $\mathbf{M}_i^{drag}$ represents the contribution of drag forces between phase; $\bar{\mathbf{u}}_{Int}$ is the averaged/filtered bulk velocity of all interfaces; and $P_{Int,i}$ and $\boldsymbol{\tau}_{Int,i}$ are the interfacial pressure and stress between phase i and all the other phases. $\mathbf{M}_i$ can be simplified knowing that $\left\langle \boldsymbol{\tau}_{Int,i} \cdot \nabla X_i \right\rangle$, which represents the interfacial shear stress, is expected to be important only in separated phase flows; hence, for most geophysical-atmospheric applications where all phases are well mixed, it can be safely ignored. So,

$$\frac{\partial \hat{\rho}_i \tilde{\mathbf{u}}_i}{\partial t} + \nabla \cdot \hat{\rho}_i \tilde{\mathbf{u}}_i \tilde{\mathbf{u}}_i = -\nabla \cdot \varepsilon_i \left(\overline{\mathbf{T}}_i + {}^{tur/SG}\mathbf{T}_i \right) + \hat{\rho}_i \tilde{\mathbf{G}}_i + \overline{\mathbf{u}}_{Int} R_i + \overline{P}_{Int,i} \nabla \varepsilon_i + \mathbf{M}_i^{drag}$$

$$\Leftrightarrow \qquad . \qquad (28)$$

$$\frac{\partial \hat{\rho}_i \tilde{\mathbf{u}}_i}{\partial t} + \nabla \cdot \hat{\rho}_i \tilde{\mathbf{u}}_i \tilde{\mathbf{u}}_i = \left(\overline{P}_{Int,i} \nabla \varepsilon_i - \nabla \varepsilon_i \overline{P}_i \right) - \nabla \cdot \varepsilon_i \left(\overline{\boldsymbol{\tau}}_i + {}^{tur/SG}\mathbf{T}_i \right) + \overline{\mathbf{u}}_{Int} R_i + \mathbf{M}_i^{drag} + \hat{\rho}_i \tilde{\mathbf{G}}_i$$

The first two terms on the RHS need to be developed in a specific phasic context. For instance, for the gas phase, the pressure is simple to define, and it is clear that $P_i=P_g$; hence, $\nabla \varepsilon_i \overline{P}_i \equiv \nabla \varepsilon_g \overline{P}_g = \varepsilon_g \nabla \overline{P}_g + \overline{P}_g \nabla \varepsilon_g$. For the solid phase, defining the pressure is more complicated, but it is generally thought that there must be a contribution from the carrier phase and possibly a contribution from the dispersed phase itself. Because the concept of "granular pressure" in this manuscript is entirely defined from a specific turbulence context (RANS vs. LES), we formally write $\nabla \varepsilon_i \overline{P}_i$ as $\nabla \varepsilon_i \overline{P}_i \cong \nabla \varepsilon_s \overline{P}_g + \nabla \varepsilon_s \overline{P}_s = \varepsilon_s \nabla \overline{P}_g + \overline{P}_g \nabla \varepsilon_s + \nabla \varepsilon_s \overline{P}_s$. The first term, $\nabla \varepsilon_s \overline{P}_g$, represents three-dimensional buoyancy effects on the particle (the gas pressure gradient exerts a buoyancy force on a population of grains), and the second term, $\nabla \varepsilon_s \overline{P}_s$, represents "granular pressure" effects that must be defined in a specific solid-phase turbulence and/or rheological model. Within the RANS framework, either ${}^{tur}P_s$ represents the collisional part of the solid pressure (while the kinetic granular pressure would represent the true turbulent motions of the grains), or ${}^{tur}P_s$ simply represents both the kinetic and the collisional pressures. A third more complete approach [e.g., *Dartevelle 2004*] is to consider the effects from an averaged bulk frictional plastic pressure, so that the total solid phase pressure would now read as $P_s = {}^{f}P_s + {}^{tur}P_s$, with ${}^{f}P_s$ (or $\overline{P}_s$) being a frictional pressure and ${}^{tur}P_s$ being a pressure from a turbulence model (e.g., kinetic-collisional model within RANS). Within LES, it is usually assumed that the granular subgrid pressure is negligible. In the following, we will assume that it is always possible to define a filtered or an ensemble-averaged solid-phase stress (i.e., $\overline{P}_s$ and $\overline{\boldsymbol{\tau}}_s$) from, for instance, a plastic rheology as achieved by *Dartevelle* [*2004*], but other interpretations can be given to $\overline{P}_s$ and $\overline{\boldsymbol{\tau}}_s$. Finally, within a two-phase flow context, Eq.(28) can be, for instance, rearranged into:

$$\begin{cases} \dfrac{\partial \hat{\rho}_g \tilde{\mathbf{u}}_g}{\partial t} + \nabla \cdot \hat{\rho}_g \tilde{\mathbf{u}}_g \tilde{\mathbf{u}}_g & = -\varepsilon_g \nabla \bar{P}_g - \nabla \cdot \varepsilon_g \left(\bar{\boldsymbol{\tau}}_g + {}^{tur/SG}\mathbf{T}_g \right) + \mathbf{M}_g^{drag} + \bar{\mathbf{u}}_{Int} R_g + \hat{\rho}_g \tilde{\mathbf{G}}_g \\ \dfrac{\partial \hat{\rho}_s \tilde{\mathbf{u}}_s}{\partial t} + \nabla \cdot \hat{\rho}_s \tilde{\mathbf{u}}_s \tilde{\mathbf{u}}_s & = -\varepsilon_s \nabla \bar{P}_g - \nabla \varepsilon_s \bar{P}_s - \nabla \cdot \varepsilon_s \left(\bar{\boldsymbol{\tau}}_s + {}^{tur/SG}\mathbf{T}_s \right) + \mathbf{M}_s^{drag} + \bar{\mathbf{u}}_{Int} R_s + \hat{\rho}_s \tilde{\mathbf{G}}_s \end{cases} \quad (29)$$

Eq.(29) is valid for both the LES and RANS frameworks. Within a specific turbulence framework, different constitutive equations must be specified for the turbulence/subgrid stress tensor of the gas phase (${}^{tur/SG}\mathbf{T}_g$), the stress tensor of the solid phase (${}^{tur/SG}\mathbf{T}_s$), and the drag vector for all the phases ($\mathbf{M}_i^{drag}$). It should be noted that in this two-phase flow context, we systematically had a term, $\left(\bar{P}_{Int,i} - \bar{P}_g \right) \nabla \varepsilon_i$, that represents the pressure difference between the interface and the carrier phase. In a well-mixed multiphase flow system, this term is negligible [*Ishii, 1975*]. Within the RANS and LES frameworks, the stress tensors from turbulence/subgrid can be defined as

$$\begin{aligned} {}^{tur}\mathbf{T}_i &= \bar{\rho}_i \widetilde{\mathbf{u}_i'' \mathbf{u}_i''} && \text{RANS framework} \\ {}^{SG}\mathbf{T}_i &= \bar{\rho}_i \left[\underbrace{\left(\widetilde{\tilde{\mathbf{u}}_i \tilde{\mathbf{u}}_i} - \tilde{\mathbf{u}}_i \tilde{\mathbf{u}}_i \right)}_{\text{Leonard}} + \underbrace{\left(\widetilde{\tilde{\mathbf{u}}_i \mathbf{u}_i''} + \widetilde{\tilde{\mathbf{u}}_i \mathbf{u}_i''} \right)}_{\text{Cross}} + \underbrace{\left(\widetilde{\mathbf{u}_i'' \mathbf{u}_i''} \right)}_{\text{Reynolds}} \right] && \text{LES framework} \end{aligned} \quad . \quad (30)$$

It should be noted that the viscous stress tensor, $\bar{\boldsymbol{\tau}}_i$, is not easy to calculate because it involves unknowns in terms of Favre phasic-weighted viscosities ($\bar{\mu}_i$ and $\overline{{}^{b}\mu_i}$) and velocities ($\bar{\mathbf{u}}_i$ instead of $\tilde{\mathbf{u}}_i$) both within the RANS and LES frameworks. As shown in *Dartevelle* [*2005*], it is common to assume that $\bar{\boldsymbol{\tau}}_i$ may be written as

$$\bar{\boldsymbol{\tau}}_i \approx -\mu_i \left(\nabla \tilde{\mathbf{u}}_i + \nabla \tilde{\mathbf{u}}_i^{\,T} \right) + \frac{2}{3} \mu_i \nabla \cdot \tilde{\mathbf{u}}_i \mathbf{I} - {}^{b}\mu_i \nabla \cdot \tilde{\mathbf{u}}_i \mathbf{I} \quad (31)$$

where the viscosities acts as a constant with respect to the LES/RANS integral operators; hence, $\bar{\mu}_i \approx \tilde{\mu}_i \approx \mu_i$ and $\overline{{}^{b}\mu_i} \approx \widetilde{{}^{b}\mu_i} \approx {}^{b}\mu_i$. Eq.(31) is, of course, a simplification that is nevertheless very common, even for compressible turbulent flows [e.g., *Gatski 1997*].

Energy

Dartevelle [*2005*] derived the energy PDE in terms of the enthalpy for the RANS and LES frameworks. However, expressing the energy in terms of the temperature is more practical for most geophysical and engineering applications. Since many forms exist for the temperature Partial Differential Equation, let us derive this multiphase PDE following the methodologies of *Dartevelle* [*2005*].

Let the specific internal energy of a single phase be $I_i = I_i(V_i, T_i)$; the thermodynamical pressure, $P_i = P_i(V_i, T_i)$, and the specific volume, $V_i = V_i(P_i, T_i)$. By chain rules and taking the material derivative, we have:

$$\begin{aligned} \frac{dI_i}{dt} &= \frac{\partial I_i}{\partial V_i}\frac{dV_i}{dt} + \frac{\partial I_i}{\partial T_i}\frac{dT_i}{dt} \\ &= \left(-P_i + T_i \frac{\partial P_i}{\partial T_i} \right)_T \frac{d\,1/\rho_i}{dt} + C_{v,i}\frac{dT_i}{dt} \end{aligned} \quad , \tag{32}$$

where P_i is a thermodynamic pressure and $C_{v,i}$ is the specific heat at constant volume. We note that if P_i is a simple linear function of T_i (typically an ideal gas), $\frac{\partial I_i}{\partial V_i}$ is zero [*Bird et al., 1960; Kashiwa, 2001*]. Using the continuity equation of a single phase, we know that $\frac{d\,1/\rho_i}{dt} = -\frac{1}{\rho_i^2}\frac{d\rho_i}{dt} = \frac{1}{\rho_i}\nabla\cdot\mathbf{u}_i$. Therefore, we conclude:

$$\frac{dI_i}{dt} = \left(-P_i + T_i \frac{\partial P_i}{\partial T_i} \right)_T \frac{d\,1/\rho_i}{dt} + C_{v,i} \frac{dT_i}{dt}$$

$$\Leftrightarrow$$

$$\frac{dI_i}{dt} = \frac{\left(-P_i + T_i \frac{\partial P_i}{\partial T_i} \right)}{\rho_i} \nabla \cdot \mathbf{u}_i + C_{v,i} \frac{dT_i}{dt} \quad .$$

$$\Leftrightarrow$$

$$\frac{d\rho_i I_i}{dt} = -I_i \rho_i \nabla \cdot \mathbf{u}_i - P_i \nabla \cdot \mathbf{u}_i + T_i \frac{\partial P_i}{\partial T_i} \nabla \cdot \mathbf{u}_i + \rho_i C_{v,i} \frac{dT_i}{dt}$$

As a reminder, we have not yet averaged or smoothed out anything, yet and we still only see one phase (which is labeled "i") in the system. From *Dartevelle* [*2005*], the equation of internal energy of only one phase in the system (n=i=1):

$$\frac{\partial \rho_i I_i}{\partial t} + \nabla \cdot \rho_i I_i \mathbf{u}_i = -\mathbf{T}_i : \nabla \mathbf{u}_i - \nabla \cdot \mathbf{q}_i + \rho_i S_i$$

$$\Leftrightarrow \quad ,$$

$$\frac{d\rho_i I_i}{dt} + \rho_i I_i \nabla \cdot \mathbf{u}_i = -\mathbf{T}_i : \nabla \mathbf{u}_i - \nabla \cdot \mathbf{q}_i + \rho_i S_i$$

where $-\mathbf{T}_i : \nabla \mathbf{u}_i = -P_i \nabla \cdot \mathbf{u}_i - \boldsymbol{\tau}_i : \nabla \mathbf{u}_i$ (see Appendix B). Hence,

$$\frac{d\rho_i I_i}{dt} + \rho_i I_i \nabla \cdot \mathbf{u}_i = -\mathbf{T}_i : \nabla \mathbf{u}_i - \nabla \cdot \mathbf{q}_i + \rho_i S_i$$

$$\Leftrightarrow$$

$$-\rho_i I_i \nabla \cdot \mathbf{u}_i - P_i \nabla \cdot \mathbf{u}_i + T_i \frac{\partial P_i}{\partial T_i} \nabla \cdot \mathbf{u}_i + \rho_i C_{v,i} \frac{dT_i}{dt} + \rho_i I_i \nabla \cdot \mathbf{u}_i = -\mathbf{T}_i : \nabla \mathbf{u}_i - \nabla \cdot \mathbf{q}_i + \rho_i S_i$$

$$\Leftrightarrow$$

$$C_{v,i} \left[\frac{\partial \rho_i T_i}{\partial t} + \nabla \cdot \rho_i T_i \mathbf{u}_i \right] = -\boldsymbol{\tau}_i : \nabla \mathbf{u}_i - T_i \frac{\partial P_i}{\partial T_i} \nabla \cdot \mathbf{u}_i - \nabla \cdot \mathbf{q}_i + \rho_i S_i$$

Following *Dartevelle* [*2005*], let us account for the presence of all n phases in the system in multiplying the last equation by the phasic function of presence (X_i). After development and rearranging all the terms:

$$X_i C_{v,i}\left[\frac{\partial \rho_i T_i}{\partial t}+\nabla\cdot\rho_i T_i\mathbf{u}_i\right]=X_i\left[-\boldsymbol{\tau}_i:\nabla\mathbf{u}_i-T_i\frac{\partial P_i}{\partial T_i}\nabla\cdot\mathbf{u}_i-\nabla\cdot\mathbf{q}_i+\rho_i S_i\right]$$

$$\Leftrightarrow$$

$$C_{v,i}\frac{\partial X_i\rho_i T_i}{\partial t}+C_{v,i}\nabla\cdot X_i\rho_i T_i\mathbf{u}_i=X_i\left(-\boldsymbol{\tau}_i:\nabla\mathbf{u}_i\right)-X_i\left(T_i\frac{\partial P_i}{\partial T_i}\nabla\cdot\mathbf{u}_i\right)-\nabla\cdot X_i\mathbf{q}_i+X_i\rho_i S_i$$
$$+\left[\rho_i T_i\frac{\partial X_i}{\partial t}+\left(\rho_i T_i\mathbf{u}_i+\mathbf{q}_i\right)\cdot\nabla X_i\right] \quad ,$$

$$\Leftrightarrow$$

$$C_{v,i}\frac{\partial X_i\rho_i T_i}{\partial t}+C_{v,i}\nabla\cdot X_i\rho_i T_i\mathbf{u}_i=X_i\left(-\boldsymbol{\tau}_i:\nabla\mathbf{u}_i\right)-X_i\left(T_i\frac{\partial P_i}{\partial T_i}\nabla\cdot\mathbf{u}_i\right)-\nabla\cdot X_i\mathbf{q}_i+X_i\rho_i S_i$$
$$+\left[\rho_i T_i\left(\mathbf{u}_{Int}-\mathbf{u}_i\right)\cdot\mathbf{n}_i\delta_{Int}-\mathbf{q}_i\cdot\mathbf{n}_i\delta_{Int}\right]$$

where the terms between brackets represent the energy properties at the interface between phases. Let us apply the mathematical angular operator and apply a *Favre mass-weighted* decomposition upon the temperature (which is either an ensemble-average operator within RANS or a spatial filter operator within LES):

$$C_{v,i}\frac{\partial\left\langle X_i\rho_i T_i\right\rangle}{\partial t}+C_{v,i}\nabla\cdot\left\langle X_i\rho_i T_i\mathbf{u}_i\right\rangle=\left\langle X_i\left(-\boldsymbol{\tau}_i:\nabla\mathbf{u}_i\right)\right\rangle-\left\langle X_i\left(T_i\frac{\partial P_i}{\partial T_i}\nabla\cdot\mathbf{u}_i\right)\right\rangle$$
$$-\nabla\cdot\left\langle X_i\mathbf{q}_i\right\rangle+\left\langle X_i\rho_i S_i\right\rangle$$
$$+\left\langle\left[\rho_i T_i\left(\mathbf{u}_{Int}-\mathbf{u}_i\right)\cdot\mathbf{n}_i\delta_{Int}-\mathbf{q}_i\cdot\mathbf{n}_i\delta_{Int}\right]\right\rangle$$

$\Leftrightarrow$

$$C_{v,i}\frac{\partial\left\langle X_i\rho_i T_i\right\rangle}{\partial t}+C_{v,i}\nabla\cdot\left\langle X_i\rho_i\left(\tilde{T}_i+T_i''\right)\left(\tilde{\mathbf{u}}_i+\mathbf{u}_i''\right)\right\rangle=\left\langle X_i\left(-\boldsymbol{\tau}_i:\nabla\mathbf{u}_i\right)\right\rangle-\left\langle X_i\left(T_i\frac{\partial P_i}{\partial T_i}\nabla\cdot\mathbf{u}_i\right)\right\rangle\quad,$$
$$-\nabla\cdot\left\langle X_i\mathbf{q}_i\right\rangle+\left\langle X_i\rho_i S_i\right\rangle$$
$$+\left\langle\left[\rho_i T_i\left(\mathbf{u}_{Int}-\mathbf{u}_i\right)\cdot\mathbf{n}_i\delta_{Int}-\mathbf{q}_i\cdot\mathbf{n}_i\delta_{Int}\right]\right\rangle$$

$\Leftrightarrow$

$$C_{v,i}\frac{\partial\hat{\rho}_i\tilde{T}_i}{\partial t}+C_{v,i}\nabla\cdot\hat{\rho}_i\tilde{T}_i\mathbf{u}_i=-\varepsilon_i\overline{\boldsymbol{\tau}_i:\nabla\mathbf{u}_i}-\varepsilon_i\overline{T_i\frac{\partial P_i}{\partial T_i}\nabla\cdot\mathbf{u}_i}-\nabla\cdot\varepsilon_i\left(\overline{\mathbf{q}}_i+{}^{tur/SG}\mathbf{q}_i\right)+\hat{\rho}_i\tilde{S}_i+{}^{T}H_i$$

where ${}^{T}H_i$ is the mean rate of interfacial heat transfer between phases for the temperature equation and must be defined within a specific context for a specific phase. As usual ${}^{T}H_i$ must comply with the jump condition (i.e., $\sum_{i=1}^{n}{}^{T}H_i=0$) and, in the absence of mass transfer between phases can simply be approached as:

$${}^{T}H_i\approx\sum_{\substack{j=1\\j\neq i}}^{n}Q_j\left(\tilde{T}_j-\tilde{T}_i\right)\quad,\tag{33}$$

where Q_j represents the interfacial heat transfer coefficient, which is usually taken as a function of the Nusselt, Reynolds numbers, and phasic heat conduction coefficients, and R_i represents the total contribution of mass transfer between i and all the other phases. The heat fluxes are defined as:

$$
\begin{aligned}
\overline{\mathbf{q}}_i \quad &\approx -k_i \nabla \tilde{T}_i && \text{molecular heat flux} \\
{}^{tur}\mathbf{q}_i \quad &= \overline{\rho_i T_i'' \mathbf{u}_i''} = \overline{\rho}_i \widetilde{T_i'' \mathbf{u}_i''} && \text{RANS framework} \\
{}^{SG}\mathbf{q}_i \quad &= \overline{\rho}_i \left[\underbrace{\widetilde{\tilde{T}_i \tilde{\mathbf{u}}_i} - \tilde{T}_i \tilde{\mathbf{u}}_i}_{\text{Leonard}} + \underbrace{\widetilde{\tilde{T}_i \mathbf{u}_i''} + \widetilde{T_i'' \tilde{\mathbf{u}}_i}}_{\text{Cross}} + \underbrace{\widetilde{T_i'' \mathbf{u}_i''}}_{\text{"Reynolds"}} \right] && \text{LES framework}
\end{aligned}
\qquad . \qquad (34)
$$

Therefore, in a two-phase flow system, where the gas phase is ideal carrier phase with only one particle size, the PDE of the Temperature must be:

$$
\begin{cases}
C_{v,g} \left[\dfrac{\partial \hat{\rho}_g \tilde{T}_g}{\partial t} + \nabla \cdot \hat{\rho}_g \tilde{T}_g \tilde{\mathbf{u}}_g \right] = -\varepsilon_g \bar{P}_g \, \nabla \cdot \tilde{\mathbf{u}}_g - \nabla \varepsilon_g \left(\overline{\mathbf{q}}_g + {}^{tur/SG}\mathbf{q}_g \right) + \hat{\rho}_g \tilde{S}_g + Q\left(T_s - T_g \right) + \varepsilon_g W_{\boldsymbol{\tau},g} \\
C_{v,g} \left[\dfrac{\partial \hat{\rho}_s \tilde{T}_s}{\partial t} + \nabla \cdot \hat{\rho}_s \tilde{T}_s \tilde{\mathbf{u}}_s \right] = -\nabla \cdot \varepsilon_s \left(\overline{\mathbf{q}}_s + {}^{tur/SG}\mathbf{q}_s \right) + \hat{\rho}_s \tilde{S}_s - Q\left(T_s - T_g \right) + \varepsilon_s W_{\boldsymbol{\tau},s}
\end{cases}
, \qquad (35)
$$

where $\tilde{S}_i$ represents any supplementary heat source terms (i.e., radiation); $W_{\boldsymbol{\tau},i}$ is the viscous dissipation; $\overline{\mathbf{q}}_i$ is the intraphase heat conduction flux; and ${}^{tur/SG}\mathbf{q}_i$ is a supplementary heat flux induced by turbulence (RANS) or by the subgrid (LES). We have neglected in Eq.(35) the supplementary dissipation from turbulence (${}^{tur}W_{\boldsymbol{\tau},i}$) or from the subgrid (${}^{SG}W_{\boldsymbol{\tau},i}$), as it is universally assumed to be negligible with respect to all the other contributions in this equation. Except, perhaps, within highly concentrated (frictional) granular flows, $W_{\boldsymbol{\tau},s}$ should be negligible in most practical cases.

In addition, it can be demonstrated that this model meets the necessary requirement for a well-posed initial value problem and is fully consistent with the second law of thermodynamics [*Dartevelle, 2005*]. The closure laws are systematically given in *Dartevelle et al.* [*2004*] for momentum and energy, in *Dartevelle* [*2005, 2006a,b*] and in Appendix A of this manuscript for turbulence and will not be repeated here.

3. *Phase 2* – The implementation of the multiphase model in the GMFIX codes

In a typical multiphase system, the momentum and energy equations (and also mass if phase transition occurs) are highly coupled through exchange terms. Those exchange terms couple the components of velocity, temperature (and possibly mass) in a given phase to the corresponding variable in the other phase. This property is called the "interequation coupling." In addition, the discretized equations are nonlinear because the coefficients of the discretized equation depend on the values of the variable to be found. Both the interequation coupling and the nonlinearity of the discretized equations must be dealt with some implicitness.

To linearize the equations, GMFIX uses the Patankar and Spalding's SIMPLE algorithm (**S**emi-**IM**plicit for **P**ressure **L**inked **E**quations) [*Patankar, 1980; Spalding, 1981, 1983*; *Patankar et al., 1998; O'Rourke et al., 1998; Syamlal, 1998; Pannala et al., 2003; Dartevelle et al., 2004; Dartevelle, 2006a,b*] as in Table 1. In the SIMPLE algorithm, a system of coupled implicit equations is solved by associating with each equation an independent solution variable and solving implicitly for the value of the associated solution variable that satisfies the equation, while keeping the other solution variables fixed. For instance, pressure appears in all the momentum equations of all the phases (gas pressure in the gas momentum equations and solid pressure in the solid momentum equations), therefore making the velocity components dependent on the pressure value and vice-versa (hence making the momentum equations nonlinear). Therefore, in the gas momentum equations, the pressure is chosen as independent variable and special treatment is used for solving the gas pressure (i.e., the pressure correction equation of *Patankar* [*1980*]; see also *Spalding* [*1983*], *Patankar et al*. [*1998*]; *Syamlal* [*1998*]). In the solid momentum equation, the solid volume fraction is chosen as independent variable (i.e., the solid volume fraction correction equation) [*Syamlal, 1998*]. To help convergence during the SIMPLE iteration process, an under-relaxation technique is used to slow down the changes in the coefficient from iteration to iteration [see Table 1; and *Patankar et al., 1998; Dartevelle et al., 2004; Dartevelle, 2006a,b*].

The interequation coupling must be dealt with some degree of implicitness to ensure fast convergence in anticipating the effects of a change in the local property of one phase on the properties of the other phase at the same location and simultaneously [*Spalding, 1981*]. This is

accomplished with the **P**artial **E**limination **A**lgorithm (PEA) of *Spalding* [*1981*] (see also, *Syamlal* [*1998*]; *Dartevelle,* [*2006a,b*]). With PEA, in a given phase, all the coefficients of the discretized equations involving the exchange terms (e.g., momentum exchange, K, and heat transfer, Q, between phases and the value of the corresponding variable from the other phase (e.g., velocities and temperature) are treated as source terms evaluated from the previous time-step iteration [*Syamlal, 1998; Dartevelle et al., 2004; Dartevelle, 2006a,b*].

Within the SIMPLE algorithm, after decoupling and linearization, GMFIX can solve the discretized equation using a classical linear solver iterative method such as the biorthogonal-conjugate gradient method (BI-CGSTAB of *van der Vorst* [1*992*]) (Table 1). GMFIX uses an automatic time-step adjustment to reduce the total run-time in achieving the best ratio of "time step/number of iteration needed for convergence" at any given simulation time [*Syamlal, 1998*]. Convergence of iterations in the linear equation solvers is judged from the residuals of various equations over the whole computational domain. Convergence is declared whenever each residual of each discretized equation within the same iteration tends to zero. If the residuals are not reduced, a supplementary iteration will be performed. If convergence is not obtained within a specified number of iterations, or if the system is divergent, then "nonconvergence" is declared and the time-step is decreased.

GMFIX uses portable OPEN-MP (for shared memory multiprocessors) and MPI (for distributed memory parallel computers) in a unified source code. The MFIX codes has been ported to a Beowulf Linux cluster, SGI SMP, Compaq SC cluster, IBM SP, and Windows2000/XP workstation (2 to 4 CPUs in SMP) and can be used on hybrid-computer SMP-DMP on a Linux cluster [*Pannala et al., 2003; Dartevelle et al., 2004*].

Table 1

The multiphase SIMPLE algorithm in relation with Partial Elimination Algorithm and linear solver techniques used in the GMFIX codes can be outlined with the following chart (based upon *Dartevelle et al.,* [*2004*] and *Dartevelle* [*2006a,b*]).

---

1. Start of a new time-step iteration. Calculate physical properties, diffusion coefficients, exchange coefficients, and reaction rates (if any).
2. Calculate guessed velocity fields of both solid and gas phase ($^{o}\mathbf{u}_s$ and $^{o}\mathbf{u}_g$) based on the available current pressure fields ($^{o}P_s$ and $^{o}P_g$) and volumetric concentrations ($^{o}\varepsilon_s$ and $^{o}\varepsilon_g$). Use BI-CGSTAB and PEA.
3. Calculate the gas pressure correction with BI-CGSTAB: $\ddot{}P_g$.
4. Update the gas pressure field with under-relaxation technique: $P_g={}^{o}P_g+\varpi_g\ddot{}P_g$, where the under-relaxation factor for the gas phase: $0<\varpi_g<1$.
5. Calculate gas velocity correction fields ($\ddot{}\mathbf{u}_g$) from $\ddot{}P_g$ and update velocity fields: $\mathbf{u}_g={}^{o}\mathbf{u}_g+\ddot{}\mathbf{u}_g$.
6. Calculate tentative estimates of solid velocity field knowing the updated $\mathbf{u}_g$ and P_g values: $^{1}\mathbf{u}_s$.
7. Calculate the solid volumetric concentration correction with BI-CGSTAB: $\ddot{}\varepsilon_s$.
8. Calculate solid velocity correction fields ($\ddot{}\mathbf{u}_s$) and update velocity fields: $\mathbf{u}_s={}^{1}\mathbf{u}_s+\ddot{}\mathbf{u}_s$.
9. Update the solid volumetric concentration: $\varepsilon_s={}^{o}\varepsilon_s+\varpi_s\ddot{}\varepsilon_s$, where the under-relaxation factor for the solid phase:
   - if $\ddot{}\varepsilon_s>0$ (i.e., solid volumetric faction is increasing) and $\varepsilon_s>{}^{f}\varepsilon_s$ (i.e., where the contact between particle is frictional), then $0<\varpi_s<1$.
   - otherwise, $\varpi_s=1$.
10. Update the gas volumetric concentration: $\varepsilon_g=1-\varepsilon_s$.
11. Update the solid pressure field P_s from ε_s.
12. Calculate solid and gas temperatures with BI-CGSTAB and PEA.
13. Calculate the granular temperature (solid-phase turbulence) with BI-CGSTAB.
14. Calculate kappa and, then, epsilon (gas-phase turbulence) with BI-CGSTAB.
15. Check for convergence judged from the normalized residuals of the linear equation solvers used in Step 2, 3, 7, 12, 13, and 14:
    - if reached, start the next time-step (step 1) and automatically adjust the time-step.
    - if not reached, restart the iteration process (step 2) with the new corrected velocity fields, pressure fields, and concentration values.

For the calculation techniques of pressure correction equation, solid volumetric correction equation, velocity field correction equations, under-relaxation factors, and Partial Elimination Algorithm (**PEA**): see *Patankar* [*1980*], *Spalding* [*1983*], *Syamlal* [*1998*], and *Patankar et al*. [*1998*]. For the linear equation solver techniques, such as the biorthogonal-conjugate gradient stable method (BI-CGSTAB), see v*an der Vorst* [*1992*]. Typically, between 5 to 20 iterations are needed before declaring convergence. Note that at convergence the gas pressure ($\ddot{}P_g$) and solid volume fraction ($\ddot{}\varepsilon_s$) corrections must go to zero [*Syamlal, 1998; Dartevelle et al., 2004*].

3.1. Integration of a Control Volume

Let us take an ideal transport equation of a scalar ϕ_i and the continuity of any given phase:

$$\begin{aligned}
&\frac{\partial \varepsilon_i \rho_i}{\partial t} + \frac{\partial \varepsilon_i \rho_i u_i}{\partial x} = R_i \\
&\frac{\partial \varepsilon_i \rho_i \phi_i}{\partial t} + \frac{\partial \varepsilon_i \rho_i \phi_i u_i}{\partial x} = \frac{\partial}{\partial x}\left(\Gamma_i \frac{\partial \phi_i}{\partial x} \right) + \Sigma_{i,\phi} - \sum_{j=1}^{n} Q_{ij} \left(\phi_i - \phi_j \right)
\end{aligned} \tag{36}$$

From left to right, in the left hand side (LHS), we have the rate of change (transient term) and convection; in the right hand side (RHS), a source term (R_i for the continuity equation and $\Sigma_{i,\phi}$ for the scalar equations), a diffusion term (only in the scalar equation), and, if ϕ_i is the phasic temperature (i.e., $\tilde{T}_i$), the very last term on the RHS represents the heat exchange (coupling) between phase (see Eq.(33)). Such coupled interphase source term must be decoupled first with a Partial Elimination Algorithm (PEA) of *Spalding* [*1981*] and [*Syamlal, 1998*]. In Eq.(36), 'x' means any of the three X-, Y-, and Z- directions (Cartesian or Cylindrical).

Let us use the standard nodes and face notations for finite volume scheme: nodal points are denoted with uppercase letters and cell faces between nodes are denoted with lower case letters. Finite volume methods integrate Eq.(36) over an arbitrary control volume (CV) as shown in 2D in Figure 2. The integration over CV of the transient term:

$$\int_{CV} \frac{\partial \varepsilon_i \rho_i \phi_i}{\partial t} dV \approx \left[\left(\varepsilon_i \rho_i \phi_i \right)_P - \left(\varepsilon_i \rho_i \phi_i \right)_P^0 \right] \frac{\Delta V}{\Delta t} \quad , \tag{37}$$

where ΔV is the volume of CV; Δt is the current time interval; the superscript '0' denotes the value at the previous time-step. The integration of the transient term of the continuity equation is obvious.

The integration over CV of the convection term:

$$\int_{CV} \frac{\partial \varepsilon_i \rho_i \phi_i u_i}{\partial x} dV \approx \left(\varepsilon_i \rho_i \phi_i\right)\Big|_e u_{x,i}\Big|_e A_e - \left(\varepsilon_i \rho_i \phi_i\right)\Big|_w u_{x,i}\Big|_w A_w + \left(\varepsilon_i \rho_i \phi_i\right)\Big|_n u_{y,i}\Big|_n A_n - \left(\varepsilon_i \rho_i \phi_i\right)\Big|_s u_{y,i}\Big|_s A_s + \left(\varepsilon_i \rho_i \phi_i\right)\Big|_t u_{z,i}\Big|_t A_t - \left(\varepsilon_i \rho_i \phi_i\right)\Big|_b u_{z,i}\Big|_b A_b \quad , \tag{38}$$

where the indices t and denotes the top and bottom faces of CV (Figure 2); A is the cross-sectional area of CV; and u_x, u_y, and u_z are the x,y, and z components of the velocity vector. Eq.(38) represents convective fluxes of $(\varepsilon_i \rho_i \phi_i)$ across the various faces of CV. Clearly, the discretization of the convective term is critical since it requires the determination of ϕ at the control volume faces instead of the node locations. The integration of the convection term of the continuity equation is similar to Eq.(38).

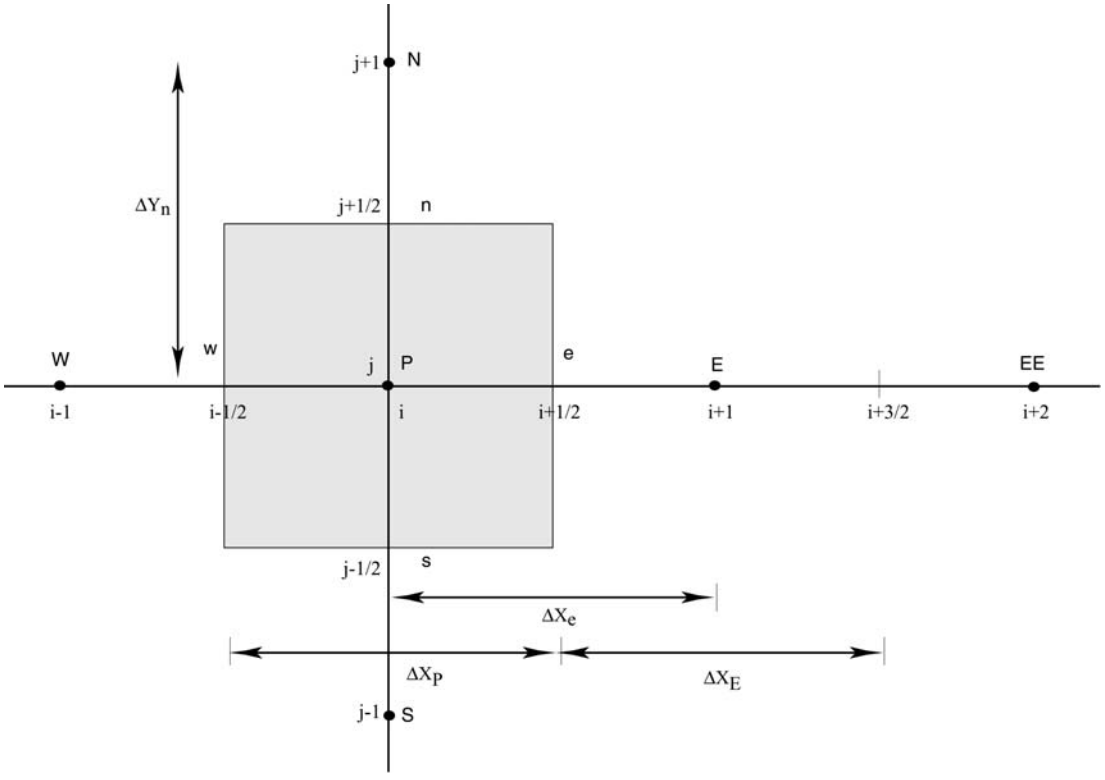

Figure 2

2D control volume, size of faces, and node (uppercase) and face (lowercase) labeling and indexation.

The integration over CV of the diffusion term (scalar equation only):

$$\int_{CV} \frac{\partial}{\partial x}\left(\Gamma_i \frac{\partial \phi_i}{\partial x}\right) dV \approx \left(\Gamma_i \frac{\partial \phi_i}{\partial x}\right)\Big|_e A_e - \left(\Gamma_i \frac{\partial \phi_i}{\partial x}\right)\Big|_w A_w + \left(\Gamma_i \frac{\partial \phi_i}{\partial y}\right)\Big|_n A_n - \left(\Gamma_i \frac{\partial \phi_i}{\partial y}\right)\Big|_s A_s + \left(\Gamma_i \frac{\partial \phi_i}{\partial z}\right)\Big|_t A_t - \left(\Gamma_i \frac{\partial \phi_i}{\partial z}\right)\Big|_b A_b \quad , \tag{39}$$

Eq.(39) represents diffusive fluxes of $\left(\Gamma_i \frac{\partial \phi_i}{\partial x}\right)$ across the various faces of CV, where, for example, the diffusive flux at the east face (Figure 2) is $\left(\Gamma_i \frac{\partial \phi_i}{\partial x}\right)\Big|_e = \left(\Gamma_i\right)\Big|_e \frac{\left(\phi_i\right)_E - \left(\phi_i\right)_P}{\Delta x_e} + O(\Delta x^2)$, which is second order accurate interpolation scheme. The value of the diffusion coefficients at the cell faces, $\left(\Gamma_i\right)\Big|_e$, are calculated using the harmonic mean of the values at the nodes between faces [*Patankar, 1980; Syamlal, 1998*]. For instance, at the east face between nodes P and E, we have (Figure 2), $\left(\Gamma_i\right)\Big|_e \approx \frac{\left(\Gamma_i\right)_P \left(\Gamma_i\right)_E}{\frac{\Delta x_E}{\Delta x_E + \Delta x_p}\left(\Gamma_i\right)_P + \left(1 - \frac{\Delta x_E}{\Delta x_E + \Delta x_p}\right)\left(\Gamma_i\right)_E}$.

In Eq.(36), the source term, R_i and $\Sigma_{i,\phi}$, and the exchange (coupling) between phase term, $\sum_{j=1}^{n} Q_{ij}\left(\phi_i - \phi_j\right)$, pose no difficulty to be integrated over the CV [*Dartevelle, 2006a,b*]. However, $\Sigma_{i,\phi}$ is usually nonlinear and needs to be linearized first following the procedures of *Patankar* [*1980*], *Syamlal* [*1998*] and *Dartevelle* [*2006a,b*], while $\sum_{j=1}^{n} Q_{ij}\left(\phi_i - \phi_j\right)$ needs to be decoupled with the PEA algorithm of *Spalding* [*1981*] (see also, *Syamlal* [*1998*] and *Dartevelle,* [*2006a,b*]):

$$\int_{CV} \Sigma_{i,\phi} dV \approx {}^{b}\Sigma_{i,\phi} \Delta V - \left(\phi_i\right)_p \, {}^{a_p}\Sigma_{i,\phi} \Delta V \tag{40}$$

$$\int_{CV} \left[\sum_{j=1}^{n} Q_{ij} \left(\phi_i - \phi_j\right) \right] dV \approx \left[\sum_{j=1}^{n} Q_{ij} \left(\phi_i - \phi_j\right) \right] \Delta V \tag{41}$$

For stability of all the iteration, the linearization must be properly written so that the first RHS term, ${}^{b}\Sigma_{i,\phi}$, is ≥ 0, and for nonnegative variable (temperature, mass fraction, granular temperature, k and epsilon), it is required that ${}^{a_p}\Sigma_{i,\phi} \geq 0$ [*Patankar, 1980; Symalal, 1998*]. Eq.(41) is written in a compact form but cannot be used as it stands since it must be decoupled first with PEA which is fully detailed in *Dartevelle* [*2006a,b*].

A similar procedure can be applied to the source term of the continuity equation, R_i. Yet it should be recalled that R_i may be negative (mass loss), which can slow down convergence and, in some cases, it would possibly destroy convergence (when it appears in the center coefficients a_p). Let us therefore define R_i as:

$$R_i = \left[\!\left[R_i \right]\!\right] - \left[\!\left[-R_i \right]\!\right] \quad , \tag{42}$$

where the double bracket operator is defined for any positive or negative variable X inside the bracket operator as follow:

$$\left[\!\left[X \right]\!\right] = \begin{cases} 0 & X \leq 0 \\ X & X > 0 \end{cases} \tag{43}$$

And, finally, the integration of Eq.(42) over CV yields:

$$\int_{CV} R_i dV \approx \left[\!\left[R_i \right]\!\right] \Delta V - \left[\!\left[-R_i \right]\!\right] \Delta V \quad , \tag{44}$$

This will guarantee that the central coefficient $(a)_p$ and/or the source term, b, in the discretized continuity equation, in Eq.(53), will be either positive or zero.

3.2. Discretization of the convection terms with the downwind factors

One of the challenging aspects of the convective terms is that their discretization requires the knowledge of ϕ at the faces $(\left(\phi_i\right)\Big|_e, \left(\phi_i\right)\Big|_w, \left(\phi_i\right)\Big|_n, \ldots)$, instead of at the nodes $(\left(\phi_i\right)_E, \left(\phi_i\right)_P, \left(\phi_i\right)_W, \left(\phi_i\right)_N, \ldots)$. A widely used method is the FOU scheme (first order upwinding) which is very stable but only first-order accurate and therefore very diffusive. For instance, at the east-face (see Figure 2), from FOU:

$$\left(\phi_i\right)\Big|_e = \begin{cases} \left(\phi_i\right)_P & \text{if } u_{i,x} \geq 0 \\ \left(\phi_i\right)_E & \text{if } u_{i,x} < 0 \end{cases} \tag{45}$$

Instead, GMFIX uses a second-order scheme. For instance, the upwinding scheme at the downstream face, ‘d’, (see Figure 3) would be:

$$\left(\phi_i\right)\Big|_d = \frac{3\left(\phi_i\right)_C - \left(\phi_i\right)_U}{2} \quad , \tag{46}$$

where the subscripts ‘U’ and ‘C’ denote upstream and central locations and ‘d’ denotes the downstream face of the CV as shown in Figure 3. The second-order schemes are, of course, more accurate but they produce unphysical oscillations which may prevent convergence. A remedy to these possible oscillations and wiggles is to apply the *flux limiter* technique of *Leonard and Mokhtari* [*1990*] [also in *Syamlal, 1998*]. The idea of the flux limiter technique is to bind the value of ϕ_i when its local variation is purely monotonic. Let us define a universal limiter, $\ddot{\phi}_i$, as a function of normalized value of ϕ_i:

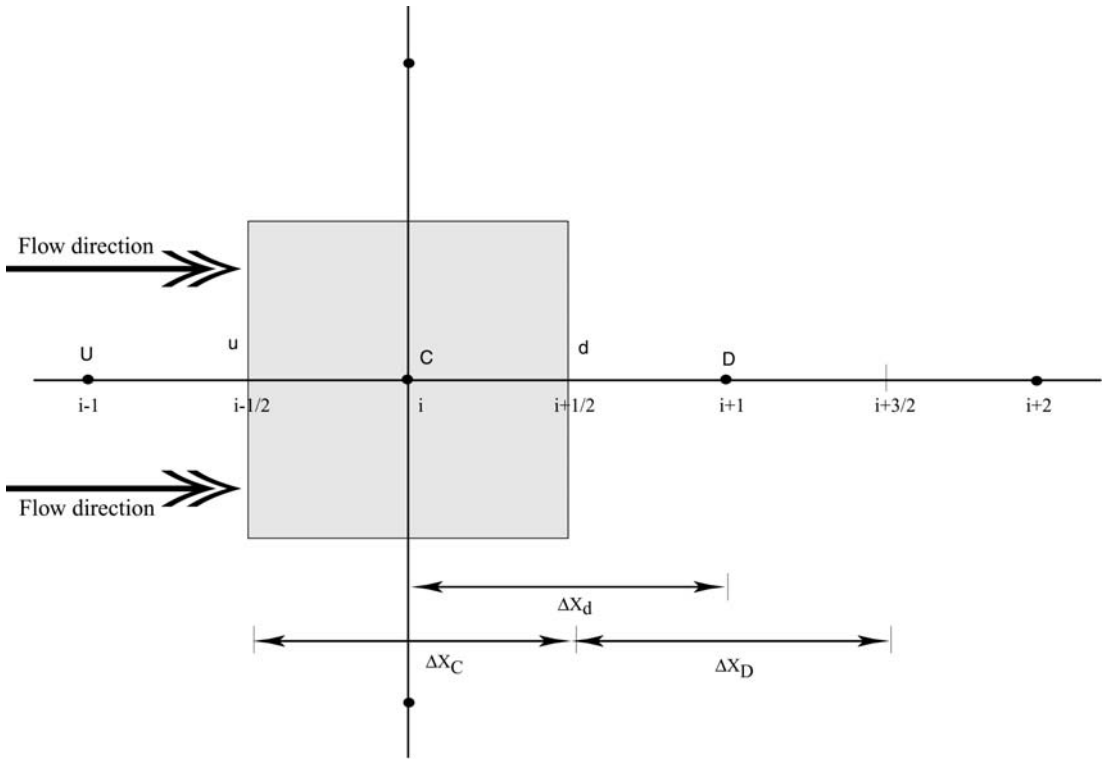

Figure 3

Upstream, central, and downstream nodes indexation (with a "wind" from west to east).

$$\dddot{\phi}_i = \frac{\phi_i - (\phi_i)_U}{(\phi_i)_D - (\phi_i)_U} \quad , \tag{47}$$

where the subscript 'D' denotes the downstream location (Figure 3). We note that by definition, if $\phi_i = (\phi_i)_U$, then $\left(\dddot{\phi}_i\right)_U = 0$ and if $\phi_i = (\phi_i)_D$, then $\left(\dddot{\phi}_i\right)_D = 1$. In Eq.(47), ϕ_i is taken at one of the node locations, either upstream, central, or downstream. Under monotonic conditions, the constraints on $\left(\dddot{\phi}_i\right)\Big|_f$ at the downwind face, 'd', of CV are given in Table 2. Therefore, from *Sweby* [*1984*], *Leonard and Mokhtari* [*1990*] and *Syamlal* [*1998*], the use of the universal limiter is achieved in terms of the downwind weighting factors ('dwf'):

$$\mathrm{dwf} = \frac{\left(\phi_i\right)\Big|_d - \left(\phi_i\right)_C}{\left(\phi_i\right)_D - \left(\phi_i\right)_C} = \frac{\left(\dddot{\phi}_i\right)\Big|_d - \left(\dddot{\phi}_i\right)_C}{1 - \left(\dddot{\phi}_i\right)_C} \tag{48}$$

dwf must follows all the conditions enumerated in Table 2. In Eq.(48), $\left(\dddot{\phi}_i\right)_C$ is evaluated at node C by Eq.(47), i.e., $\left(\dddot{\phi}_i\right)_C = \frac{\left(\phi_i\right)_C - \left(\phi_i\right)_U}{\left(\phi_i\right)_D - \left(\phi_i\right)_U}$. In Eq.(48), an initial estimate of $\left(\phi_i\right)\Big|_d$ or $\left(\dddot{\phi}_i\right)\Big|_d$ is needed in order to find the value of dwf. This estimate can be provided by any first order or second order accurate discretization scheme. For instance, with the upwinding scheme, Eq.(46), with Eq.(47) and Eq.(48), we have $\mathrm{dwf} = \frac{1}{2}\theta$, where $\theta = \frac{\left(\phi_i\right)_C - \left(\phi_i\right)_U}{\left(\phi_i\right)_D - \left(\phi_i\right)_C} = \frac{\left(\dddot{\phi}_i\right)_C}{1 - \left(\dddot{\phi}_i\right)_C}$. Table 3 provides other estimates for dwf (or θ). Finally, within nonmonotonic conditions for all 2nd order schemes (either $\left(\dddot{\phi}_i\right)_C < 0$ or $\left(\dddot{\phi}_i\right)_C > 1$), we have dwf = 0 and with the simple FOU scheme, dwf = 0. Once the value of dwf is known, it is clear that the final value of $\left(\phi_i\right)\Big|_d$ at the downwind face ‘d’ must be then,

$$\left(\phi_i\right)\Big|_d = \mathrm{dwf}\ \left(\phi_i\right)_D + \left(1 - \mathrm{dwf}\right)\left(\phi_i\right)_C \quad . \tag{49}$$

This equation is generalized at all faces (as in Figure 2) throughout GMFIX codes in introducing weighting factors at all faces, ξ:

$$\xi = \begin{cases} \mathrm{dwf} & \text{if } u_i \geq 0 \\ 1 - \mathrm{dwf} & \text{if } u_i < 0 \end{cases} \tag{50}$$

For instance, at the East face, we must have $\left(\phi_i\right)\Big|_e = \xi\Big|_e \left(\phi_i\right)_E + \dddot{\xi}\Big|_e \left(\phi_i\right)_P$ with $\dddot{\xi}\Big|_e = 1 - \xi\Big|_e$.

Table 2

Constraints imposed on $\left(\ddot{\phi}_i\right)\Big|_f$ at the downwind face, 'd', of CV [*Syamlal, 1998*]. All these constraints can be also represented on a normalized variable diagram as shown in Figure 4.

1- $\left(\ddot{\phi}_i\right)_C \le \left(\ddot{\phi}_i\right)\Big|_d \le 1$ for any $0 \le \left(\ddot{\phi}_i\right)_C \le 1$. And, the special case, if $(\phi_i)_C = (\phi_i)_D$, then $\left(\phi_i\right)\Big|_d = \left(\phi_i\right)_C = \left(\phi_i\right)_D$, therefore, $\left(\ddot{\phi}_i\right)\Big|_d = 1$ for $\left(\ddot{\phi}_i\right)_C = 1$.

2- If $(\phi_i)_C = (\phi_i)_U$, then it is required that $\left(\phi_i\right)\Big|_d = \left(\phi_i\right)_C = \left(\phi_i\right)_U$, therefore, $\left(\ddot{\phi}_i\right)\Big|_d = 0$ for any $\left(\ddot{\phi}_i\right)_C = 0$.

3- To prevent nonunique values of $\left(\ddot{\phi}_i\right)\Big|_d$ when $\left(\ddot{\phi}_i\right)_C \to 0$ (see Figure 4), we define $\left(\ddot{\phi}_i\right)\Big|_d = \dfrac{\left(\ddot{\phi}_i\right)_C}{c}$ for $0 \le \left(\ddot{\phi}_i\right)_C \le c$, where 'c' is the normal direction Courant number, e.g., downward, $c = \dfrac{u_{x,i}\Delta t}{\Delta x_C}$. Therefore, when $\left(\ddot{\phi}_i\right)_C = 0$, then $\left(\ddot{\phi}_i\right)\Big|_d = 0$ is uniquely enforced.

4- For nonmonotonic conditions (either $\left(\ddot{\phi}_i\right)_C < 0$ or $\left(\ddot{\phi}_i\right)_C > 1$), the universal limiter does not impose any specific conditions other than the fact that $\left(\ddot{\phi}_i\right)\Big|_d$ must be on the line between (0,0) and (1,1) which has a positive slope as shown in Figure 4.

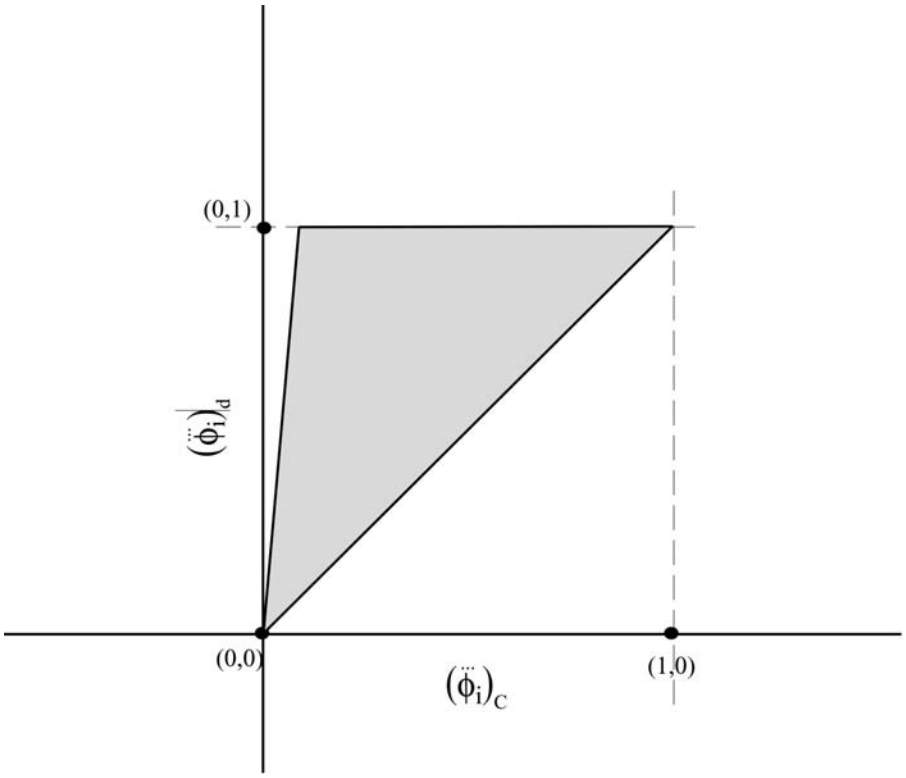

Figure 4

The normalized variable diagram (NVD) of $\left(\ddot{\phi}_i\right)\Big|_d$ at the downwind face 'd'. The allowable values are within the triangular gray area. To prevent any overshoots and undershoots, any values of $\left(\phi_i\right)\Big|_d$ calculated by any higher order scheme should be forced to pass through the triangular gray area.

Table 3

Downwind weighting factors ('dwf')

Scheme	dwf
First order upwinding (FOU)	dwf = 0
2nd order upwinding[1]	$\mathrm{dwf} = \frac{1}{2}\theta$
Monotonic upstream-centered Scheme for Conservation Law (MUSCL)[1] [*van Leer, 1979*]	$\mathrm{dwf} = \frac{1}{2}\max[0, \min(2\theta, \frac{1}{2}+\frac{1}{2}\theta, 2)]$
MinMod[1] [*Sweby, 1984*]	$\mathrm{dwf} = \frac{1}{2}\max[0, \min(1, \theta)]$
van Leer [*Sweby, 1984 after van Leer, 1979*]	$\mathrm{dwf} = \left(\dddot{\phi}_i\right)_C$

Notes

[1]: where, θ, is $\theta = \dfrac{\left(\phi_i\right)_C - \left(\phi_i\right)_U}{\left(\phi_i\right)_D - \left(\phi_i\right)_C} = \dfrac{\left(\dddot{\phi}_i\right)_C}{1-\left(\dddot{\phi}_i\right)_C}$

The weighting factors, ξ, allow computing the dwf once and for all without rechecking the flow directions all the time. And, finally, we may rewrite the convection terms of Eq.(38) with the weighting factors as:

$$\begin{aligned}\int_{CV} \frac{\partial \varepsilon_i \rho_i \phi_i u_i}{\partial x} dV \approx & \left[\xi\big|_e \left(\varepsilon_i\rho_i\phi_i\right)_E + \dddot{\xi}\big|_e \left(\varepsilon_i\rho_i\phi_i\right)_P\right] u_{x,i}\big|_e A_e - \left[\xi\big|_w \left(\varepsilon_i\rho_i\phi_i\right)_P + \dddot{\xi}\big|_w \left(\varepsilon_i\rho_i\phi_i\right)_W\right] u_{x,i}\big|_w A_w \\ & + \left[\xi\big|_n \left(\varepsilon_i\rho_i\phi_i\right)_N + \dddot{\xi}\big|_n \left(\varepsilon_i\rho_i\phi_i\right)_P\right] u_{y,i}\big|_n A_n - \left[\xi\big|_s \left(\varepsilon_i\rho_i\phi_i\right)_P + \dddot{\xi}\big|_s \left(\varepsilon_i\rho_i\phi_i\right)_S\right] u_{y,i}\big|_s A_s \\ & + \left[\xi\big|_t \left(\varepsilon_i\rho_i\phi_i\right)_T + \dddot{\xi}\big|_t \left(\varepsilon_i\rho_i\phi_i\right)_P\right] u_{z,i}\big|_t A_t - \left[\xi\big|_b \left(\varepsilon_i\rho_i\phi_i\right)_P + \dddot{\xi}\big|_b \left(\varepsilon_i\rho_i\phi_i\right)_B\right] u_{z,i}\big|_b A_b\end{aligned} \quad (51)$$

3.3. Final discretized equations

Combining Eq.(37) (transient), Eq.(39) (conduction), Eq.(40) (scalar source) or Eq.(44) (continuity source), and Eq.(51) (convection) altogether in Eq.(36) yields to the following forms:

Continuity equation

$$
\begin{aligned}
&+\left[\left(\varepsilon_i\rho_i\right)_P-\left(\varepsilon_i\rho_i\right)_P^0\right]\frac{\Delta V}{\Delta t}\\
&+\left[\xi\big|_e\left(\varepsilon_i\rho_i\right)_E+\ddot{\xi}\big|_e\left(\varepsilon_i\rho_i\right)_P\right]u_{x,i}\big|_e\,A_e-\left[\xi\big|_w\left(\varepsilon_i\rho_i\right)_P+\ddot{\xi}\big|_w\left(\varepsilon_i\rho_i\right)_W\right]u_{x,i}\big|_w\,A_w\\
&+\left[\xi\big|_n\left(\varepsilon_i\rho_i\right)_N+\ddot{\xi}\big|_n\left(\varepsilon_i\rho_i\right)_P\right]u_{y,i}\big|_n\,A_n-\left[\xi\big|_s\left(\varepsilon_i\rho_i\right)_P+\ddot{\xi}\big|_s\left(\varepsilon_i\rho_i\right)_S\right]u_{y,i}\big|_s\,A_s \quad , \qquad (52)\\
&+\left[\xi\big|_t\left(\varepsilon_i\rho_i\right)_T+\ddot{\xi}\big|_t\left(\varepsilon_i\rho_i\right)_P\right]u_{z,i}\big|_t\,A_t-\left[\xi\big|_b\left(\varepsilon_i\rho_i\right)_P+\ddot{\xi}\big|_b\left(\varepsilon_i\rho_i\right)_B\right]u_{z,i}\big|_b\,A_b\\
&=\\
&+\left[\!\left[R_i\right]\!\right]\Delta V-\left[\!\left[-R_i\right]\!\right]\Delta V
\end{aligned}
$$

which can be written to a classic compact forms:

$$\left(a\right)_P\left(\varepsilon_i\rho_i\right)_P=\sum_{nb}\left(a\right)_{nb}\left(\varepsilon_i\rho_i\right)_{nb}+b \quad , \qquad (53)$$

where the subscript ‘nb’ represents contributions from east, west, north, south, top, and bottom nodes; ‘b’ is the contribution the discretization of the transient term and from the volume integral of the linearized source terms:

$\left(a\right)_E=-\xi\big\|_e\,u_{x,i}\big\|_e\,A_e$	$\left(a\right)_W=+\ddot{\xi}\big\|_w\,u_{x,i}\big\|_w\,A_w$
$\left(a\right)_N=-\xi\big\|_n\,u_{y,i}\big\|_n\,A_n$	$\left(a\right)_S=+\ddot{\xi}\big\|_s\,u_{y,i}\big\|_s\,A_s$
$\left(a\right)_T=-\xi\big\|_t\,u_{z,i}\big\|_t\,A_t$	$\left(a\right)_B=+\ddot{\xi}\big\|_b\,u_{z,i}\big\|_b\,A_b$
$b=\left[\!\left[R_i\right]\!\right]\Delta V+\left(\varepsilon_i\rho_i\right)_P^0\,\frac{\Delta V}{\Delta t}$	
$\left(a\right)_P=\frac{\Delta V}{\Delta t}+\left[\!\left[-R_i\right]\!\right]\frac{\Delta V}{\left(\varepsilon_i\rho_i\right)_P}-\sum_{nb}\left(a\right)_{nb}$	

Scalar equation

$$
\begin{aligned}
&+\left[\left(\varepsilon_i\rho_i\phi_i\right)_P-\left(\varepsilon_i\rho_i\phi_i\right)_P^0\right]\frac{\Delta V}{\Delta t}\\
&+\left[\xi\big|_e\left(\varepsilon_i\rho_i\phi_i\right)_E+\ddot{\xi}\big|_e\left(\varepsilon_i\rho_i\phi_i\right)_P\right]u_{x,i}\big|_e\,A_e-\left[\xi\big|_w\left(\varepsilon_i\rho_i\phi_i\right)_P+\ddot{\xi}\big|_w\left(\varepsilon_i\rho_i\phi_i\right)_W\right]u_{x,i}\big|_w\,A_w\\
&+\left[\xi\big|_n\left(\varepsilon_i\rho_i\phi_i\right)_N+\ddot{\xi}\big|_n\left(\varepsilon_i\rho_i\phi_i\right)_P\right]u_{y,i}\big|_n\,A_n-\left[\xi\big|_s\left(\varepsilon_i\rho_i\phi_i\right)_P+\ddot{\xi}\big|_s\left(\varepsilon_i\rho_i\phi_i\right)_S\right]u_{y,i}\big|_s\,A_s\\
&+\left[\xi\big|_t\left(\varepsilon_i\rho_i\phi_i\right)_T+\ddot{\xi}\big|_t\left(\varepsilon_i\rho_i\phi_i\right)_P\right]u_{z,i}\big|_t\,A_t-\left[\xi\big|_b\left(\varepsilon_i\rho_i\phi_i\right)_P+\ddot{\xi}\big|_b\left(\varepsilon_i\rho_i\phi_i\right)_B\right]u_{z,i}\big|_b\,A_b\\
&=\\
&+\left(\Gamma_i\right)\big|_e\,\frac{\left(\phi_i\right)_E-\left(\phi_i\right)_P}{\Delta x_e}A_e-\left(\Gamma_i\right)\big|_w\,\frac{\left(\phi_i\right)_P-\left(\phi_i\right)_W}{\Delta x_w}A_w\\
&+\left(\Gamma_i\right)\big|_n\,\frac{\left(\phi_i\right)_N-\left(\phi_i\right)_P}{\Delta y_n}A_n-\left(\Gamma_i\right)\big|_s\,\frac{\left(\phi_i\right)_P-\left(\phi_i\right)_S}{\Delta y_s}A_s\\
&+\left(\Gamma_i\right)\big|_t\,\frac{\left(\phi_i\right)_T-\left(\phi_i\right)_P}{\Delta z_t}A_t-\left(\Gamma_i\right)\big|_b\,\frac{\left(\phi_i\right)_B-\left(\phi_i\right)_P}{\Delta z_b}A_b\\
&+{}^{b}\Sigma_{i,\phi}\Delta V-\left(\phi_i\right)_P\,{}^{a_p}\Sigma_{i,\phi}\Delta V-\left[\sum_{j=1}^{n}Q_{ij}\left(\left(\phi_i\right)_P-\left(\phi_j\right)_P\right)\right]\Delta V
\end{aligned}
\qquad (54)
$$

The last term on the RHS, $\sum_{j=1}^{n}Q_{ij}\left(\left(\phi_i\right)_P-\left(\phi_j\right)_P\right)$, represents heat exchanged between phases and need to be decoupled first with PEA. This term only exists when the scalar variable is the temperature. As done to the continuity equation, Eq.(53), we need to rewrite Eq.(54) in a compact form. Before doing so, we must subtract the discretized continuity equation times $(\phi_i)_P$ from the initial discretized scalar equation. The reason of this extra-manipulation is to prevent large variation in the values of ϕ_i potentially induced by small mass imbalances which may occur during the iteration process [*Patankar, 1980*; *Syamlal, 1998; Guenther and Syamlal, 2001; Dartevelle, 2006a,b*]. Finally, the compact form of the scalar equation:

$$
\left(a_\phi\right)_P\left(\phi_i\right)_P=\sum_{nb}\left(a_\phi\right)_{nb}\left(\phi_i\right)_{nb}+b_\phi-\left[\sum_{j=1}^{n}Q_{ij}\left(\left(\phi_i\right)_P-\left(\phi_j\right)_P\right)\right]\Delta V\quad , \qquad (55)
$$

with,

$\left(a_\phi\right)_E = \left[\frac{\left(\Gamma_i\right)\big\vert_e}{\Delta x_e} - \xi\big\vert_e \left(\varepsilon_i\rho_i\right)_E u_{x,i}\big\vert_e\right] A_e$	$\left(a_\phi\right)_W = \left[\frac{\left(\Gamma_i\right)\big\vert_w}{\Delta x_w} + \dddot{\xi}\big\vert_w \left(\varepsilon_i\rho_i\right)_W u_{x,i}\big\vert_w\right] A_w$
$\left(a_\phi\right)_N = \left[\frac{\left(\Gamma_i\right)\big\vert_n}{\Delta y_n} - \xi\big\vert_n \left(\varepsilon_i\rho_i\right)_N u_{y,i}\big\vert_n\right] A_n$	$\left(a_\phi\right)_S = \left[\frac{\left(\Gamma_i\right)\big\vert_s}{\Delta y_s} + \dddot{\xi}\big\vert_s \left(\varepsilon_i\rho_i\right)_S u_{y,i}\big\vert_s\right] A_s$
$\left(a_\phi\right)_T = \left[\frac{\left(\Gamma_i\right)\big\vert_t}{\Delta z_t} - \xi\big\vert_t \left(\varepsilon_i\rho_i\right)_T u_{z,i}\big\vert_t\right] A_t$	$\left(a_\phi\right)_B = \left[\frac{\left(\Gamma_i\right)\big\vert_b}{\Delta z_b} + \dddot{\xi}\big\vert_b \left(\varepsilon_i\rho_i\right)_B u_{z,i}\big\vert_b\right] A_b$
$b_\phi = +\left(\varepsilon_i\rho_i\phi_i\right)_P^0 \frac{\Delta V}{\Delta t} + {}^b\Sigma_{i,\phi}\Delta V + \left(\phi_i\right)_p \left[\!\left[-R_i\right]\!\right]\Delta V + {}^b\mathrm{PEA}_{i,\phi}\Delta V$	
$\left(a_\phi\right)_p = +\left(\varepsilon_i\rho_i\right)_P^0 \frac{\Delta V}{\Delta t} + \left(\phi_i\right)_p {}^{a_p}\Sigma_{i,\phi}\Delta V + \left[\!\left[R_i\right]\!\right]\Delta V - \sum_{nb}\left(a_\phi\right)_{nb} + {}^{a_p}\mathrm{PEA}_{i,\phi}\Delta V$	

We note that the terms for b_ϕ and $(a_\phi)_P$, ${}^b\mathrm{PEA}_{i,\phi}$ and ${}^{ap}\mathrm{PEA}_{i,\phi}$ respectively, are from the partial elimination algorithm (PEA) applied to $-\left[\sum_{j=1}^{n} Q_{ij}\left(\left(\phi_i\right)_p - \left(\phi_j\right)_p\right)\right]$ which is fully described in *Syamlal* [*1998*].

3.4. Discretized scalar equation with deferred corrections

The previous downwind weighting factors method places a large emphasis on the downstream values rather than the upstream, which in some rare instances may slow convergence. Therefore, an alternative method has also been implemented in MFIX/GMFIX, the *deferred correction method* (DCM). The approach is rather simple, an algebraic system as in Eq.(55) is solved first using the stable first order upwinding (FOU) scheme (i.e., Eq.(45)), and then, afterwards, additional source terms are added to capture the accurateness of higher order schemes:

$$\left(a\right)_P \left(\phi_i\right)_P = \sum_{nb} \left(a\right)_{nb} \left(\phi_i\right)_{nb} + b + S_{DCM} \quad , \tag{56}$$

where S_{DCM} is a supplementary source term obtained from the DCM scheme. The convection terms from FOU are implicit in the coefficients $(a)_P$ and $(a)_{nb}$. The additional source term, S_{DCM}, is given by [*Guenther and Syamlal, 2001*]:

$$\begin{aligned} S_{DCM} = & \left(\varepsilon_i \rho_i\right)\Big|_w \left({}^{FOU}\phi_i - {}^{High}\phi_i \right)\Big|_w u_{x,i}\Big|_w A_w - \left(\varepsilon_i \rho_i\right)\Big|_e \left({}^{FOU}\phi_i - {}^{High}\phi_i \right)\Big|_e u_{x,i}\Big|_e A_e \\ & + \left(\varepsilon_i \rho_i\right)\Big|_s \left({}^{FOU}\phi_i - {}^{High}\phi_i \right)\Big|_s u_{y,i}\Big|_s A_s - \left(\varepsilon_i \rho_i\right)\Big|_n \left({}^{FOU}\phi_i - {}^{High}\phi_i \right)\Big|_n u_{y,i}\Big|_n A_n \\ & + \left(\varepsilon_i \rho_i\right)\Big|_b \left({}^{FOU}\phi_i - {}^{High}\phi_i \right)\Big|_b u_{z,i}\Big|_b A_b - \left(\varepsilon_i \rho_i\right)\Big|_t \left({}^{FOU}\phi_i - {}^{High}\phi_i \right)\Big|_t u_{z,i}\Big|_t A_t \end{aligned} \tag{57}$$

It can be seen that the contribution from FOU terms will cancel out because the added FOU terms are implicitly in $(a)_P$ and $(a)_{nb}$, while the subtracted FOU terms are in S_{DCM}. Therefore, at convergence, there is not net contribution of ${}^{FOU}\phi_i$ into Eq.(56). We note that at the east face, we have:

$$\left({}^{FOU}\phi_i \right)\Big|_e = \begin{cases} \left(\phi_i\right)_P & \text{if } u_{i,x} \geq 0 \\ \left(\phi_i\right)_E & \text{if } u_{i,x} < 0 \end{cases} \quad , \tag{58}$$

and,

$$\left({}^{High}\phi_i \right)\Big|_e = \xi\Big|_e \left(\phi_i\right)_E + \ddot{\xi}\Big|_e \left(\phi_i\right)_P \quad , \tag{59}$$

with the weighting factors, ξ, are given by Eq.(50) and $\ddot{\xi}\Big|_e = 1 - \xi\Big|_e$.

The discretization of the three momentum equations ($\mathbf{u}_{x,i}$, $\mathbf{u}_{y,i}$, $\mathbf{u}_{z,i}$) is similar to the scalar equation. However, to enforce stability, the momentum control volume (CV) must be staggered:

the X-momentum CV is shifted half a cell eastward, the Y-momentum CV is shifted northward by half a cell, and the Z-momentum is shifted topward by half a cell. For a full explanation of how the momentum equations are discretized, we refer to *Syamlal* [*1998*] *and Dartevelle* [*2006a,b*]. The final discretization of the pressure correction equation for the fluid phase and of the volumetric concentration correction equation for the dispersed phase can be found in *Syamlal* [*1998*].

Finally, the Partial Elimination Algorithm (PEA) of *Spalding* [*1980*] is entirely described in *Syamlal* [*1998*] and in *Dartevelle* [*2006a,b*]. Such a PEA allows maintaining both the coupling between phases and, at the same time, the standard septadiagonal matrix [*Syamlal, 1998*].

4. *Phase 3* – Assessing the model credibility: the Verification and Validation process

Strictly speaking, the model "credibility" (and thereof the "confidence" we may gain in its numerical results) must be assessed following a strict verification and validation (V&V) process which involves two critical steps [*American Institute of Aeronautics and Astronautics, 1998*]:

Step 1 – Verification, or is the "problem" being correctly solved?

Within the V&V analysis, the first step, the *verification* process, is defined as "the process of determining that a model implementation accurately represents the conceptual description of the model." Therefore a verification analysis requires exact analytical solutions or highly accurate simplified experimental data to test whether the code (i.e., the model "implementation") is an accurate representation of the model designed during the first phase in §2 (i.e., the model "conception"). Strictly speaking, in this verification process, no claim needs to be made of the relationship between the model and its implementation and the "real world." In other words, a well thought out verification test case does not necessarily need to be realistic, it merely needs to provide a rigorous framework to test the accurateness and correctness of the model implementation.

Step 2 – Validation, or is the correct "problem" being solved?

Within the V&V analysis, the second step, the *validation* process is defined as "the process of determining the degree to which a model is an accurate representation of the real world." Therefore, a validation analysis requires complex experimental data of the real world physics. Clearly, the validation analysis does not need to test whether the code is accurate, but rather, must test whether the conception of the model (and its implementation) is a correct representation of the physics of the "real world" aimed to be modeled. In this validation phase, it would be desirable to have well-constrained experimental data, but given the complexity of the "real world," it is acceptable to have less than perfect experimental data as long as there is a clear understanding of the experimental uncertainty and clear quantification of the experimental errors.

Obviously, the validation step must necessarily come after verification. Validation alone –no matter how successful– is not enough to claim confidence in the produced numerical results.

Verification can be a fairly easy exercise: GMFIX results need to be compared to exact analytical solutions from well-known "Riemann problems," e.g., the Sod [*Sod, 1978; Toro, 1999*] and the "123" problems [*Toro, 1999*]. Validation is inherently more challenging because it requires high-quality analog experiments, which somehow represent the "real world" the modeler seeks to model. We have validated GMFIX against two different classes of experiments. One class of validations involves the development of single phase and multiphase jets under supersonic conditions [*Ladenburg et al., 1949; Lewis and Carlson, 1964*]. The second independent class of validation experiments involves the development of single-phase and multiphase confined jets under highly turbulent conditions [*Hishida et al., 1987*]. These two different classes of validation test cases attempt to encompass and capture the "real world" physics of explosive volcanology, viz., shocked, supersonic, turbulent, and single to multiphase flows.

4.1. Verification of the implementation of the model

The *verification* test cases involved two classic shock-tube experiments performed in 1D with a single-phase ideal gas (dry air): the Sod and the "123" problems [*Sod, 1978; Toro, 1999*]. Since all PDEs, in any direction, for any species and phases, use the same numerical solver (e.g., FOU, MUSCL, MINMOD), with the same linear equation solver (BI-CGSTAB), within the same SIMPLE algorithm, it does not matter whether the verification test case involves only one phase or only one dimension. In these two shock tube cases, the verification analysis tests the accurateness and robustness of GMFIX discretized PDEs and of its numerical solvers.

The Sod Problem

The Sod problem (see Figure 5) involves an ideal gas in a one-dimensional shock tube with both ends closed and a diaphragm separating a region of higher pressure, temperature, and density on the left side, named the driver section (10 psi or $6.9 \cdot 10^{4}$ Pa, 288.9 K, $8.3 \cdot 10^{-1}$ kg/m^3), from a region of lower pressure, temperature, and density on the right side, named the driven section (1 psi or $6.9 \cdot 10^{3}$ Pa, 231 K, $1.0 \cdot 10^{-1}$ kg/m^3). This test-case solution consists of a left sonic rarefaction wave, a right traveling contact wave, and a right shock wave.

When the diaphragm is instantaneously broken (Figure 5), a shock wave propagates to the right which increases the pressure behind it and induces a mass motion towards the right with some velocity (Figure 5B). The interface surface between the driver and driven gases also travels at that velocity. Across this interface surface, the internal energy (Figure 5D) changes abruptly but the pressure and velocity are preserved, forming a second step (Figure 5C) in the density profile behind the initial shock front propagating to the right. The expansion wave, which propagates to the left, decreases smoothly and continuously the pressure and the density profiles in the left side of the shock tube (Figure 5A & C). Figure 5 shows an obvious excellent agreement between the exact analytical curve (plain red) and the numerical data obtained from GMFIX. Generally speaking, the higher the grid resolution, the better the agreement (Figure 5).

The 123 Problem

The 123 problem (Figure 6) involves an ideal gas in a one-dimensional shock tube with two opened ends. The tube is emptied in both directions with a constant velocity of ~2.7 times the speed of sound at the initial time. At initial time, pressure (0.4 atm), temperature (500 K) and density (ρ = 0.2824 kg/m^3) are uniform everywhere in the tube with velocities equal but opposite ($\pm$ 1204.4 m/s). This test-case solution consists of two rarefaction waves and a trivial stationary contact discontinuity in the middle of the tube that forms a quasi vacuum. Because the middle of the tube forms a stationary quasi vacuum, with pressure and density going near zero (Figure 6A & C), this 123 Problem tests the capability of a code and its numerical solvers to handle with very low pressures and densities. In other words, it tests the stability of a given numerical scheme under quasi vacuum conditions when the energy has a zero-by-zero division (= P/ ρ). Hence, this verification problem performs a good test of the accurateness and robustness of the energy PDE under those conditions. From Figure 6, there is excellent agreement between the exact analytical curve (plain red) and the numerical data obtained from GMFIX with the MUSCL solver. Specifically, in Figure 6D, one can see that the vacuum conditions in the middle of the shock tube cause the energy equation to produce small (yet negligible) numerical artifacts. The agreement is enhanced when a second-order time-accurate scheme is chosen (e.g., Crank-Nicholson scheme).

Because of the vacuum, this test case is rarely passed by numerical codes because the energy solutions start to produce incorrect results in the middle of the tube, and eventually become unstable. Generally speaking, the higher the grid resolution, the better the agreement (Figure 6).

One should not forget that for all simulations these finite volume methods always require a systematic test of grid size independence. A coarse grid and/or a poor choice of numerical solver (e.g., 1st order vs. 2nd order accurate) can also lead to poor-quality numerical results, even on a fully verified code as show in Figure 7.

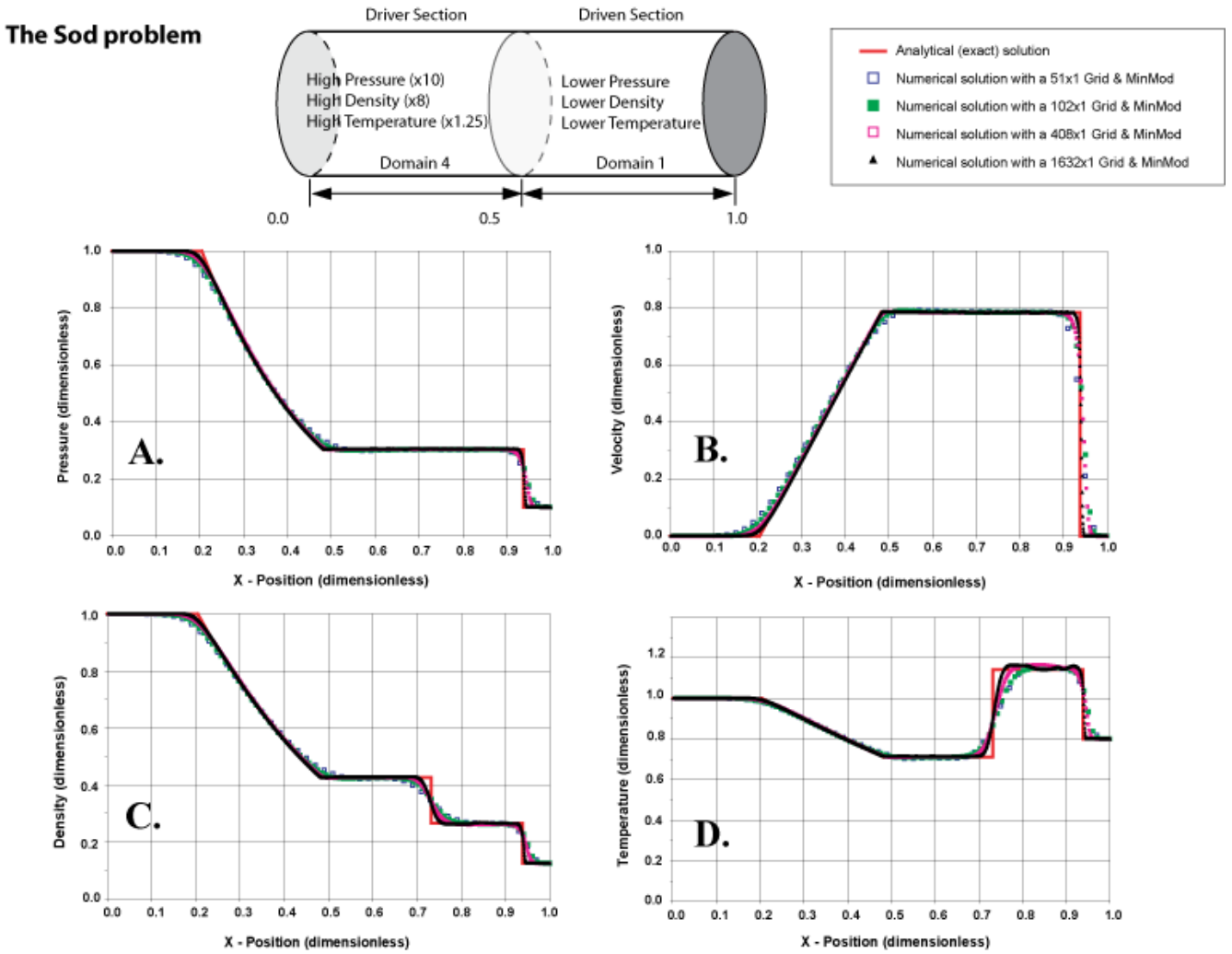

Figure 5

Sock tube problem, the Sod's Verification test case [*Sod, 1978*]. This problems involves an ideal gas in a 1D, closed-ends shock tube with a diaphragm in the middle separating an area of high pressure, density and temperature (the driver section, left) from an area of low P, ρ, T (driven section, right). The plain red curve represents the exact analytical solution compared with the GMFIX solution obtained with MINMOD scheme [*Sweby, 1984*] for different grid resolutions: 1x51, 1x102, 1x408, and 1x1632. All axes are dimensionless. **A**: Pressure vs. position in the shock tube. **B**: Density vs. position. **C**: Velocity vs. position. **D**: Temperature (specific Internal Energy) vs. position.

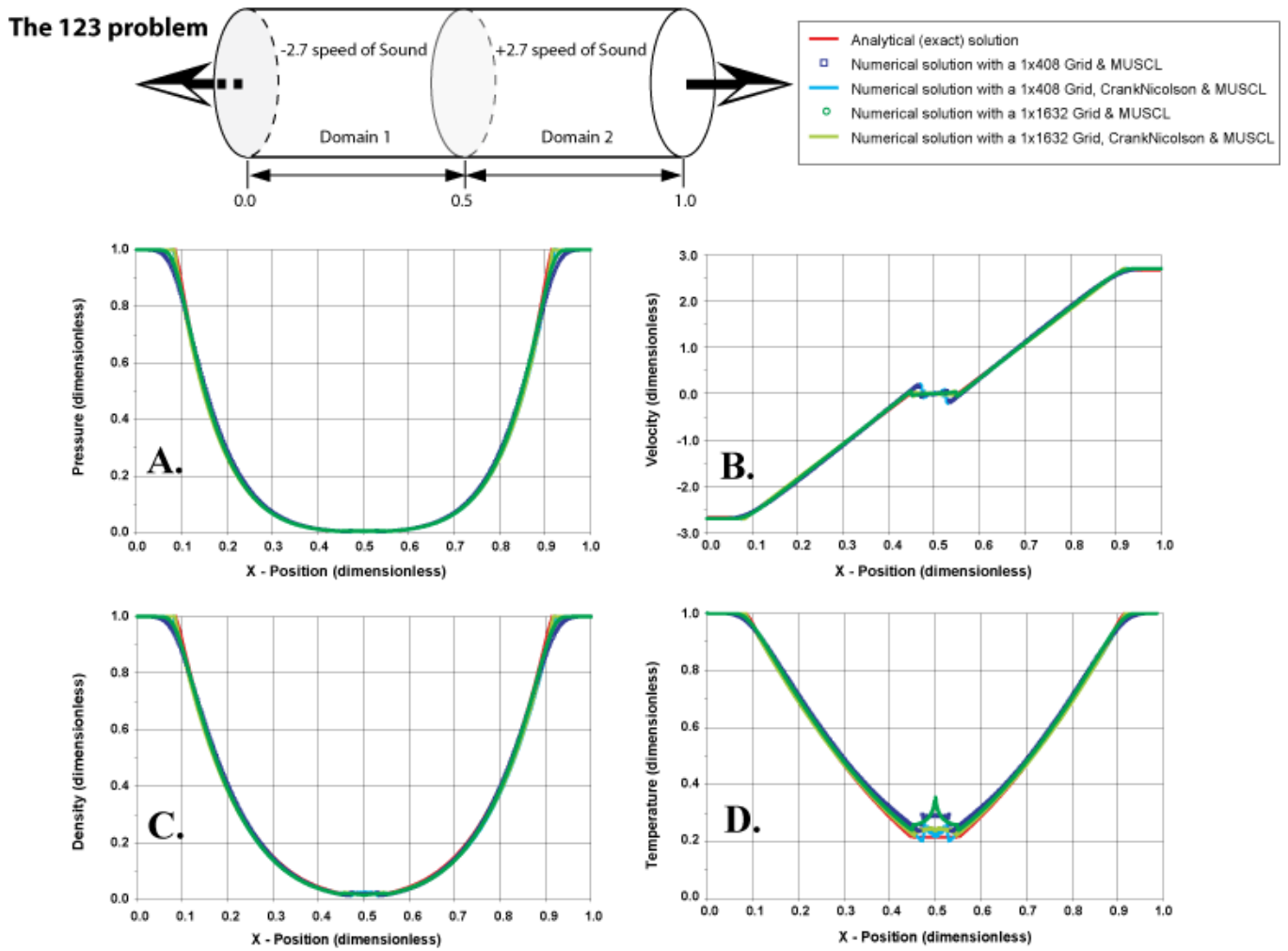

Figure 6

Sock tube verification test-case, the "123" problem [*Toro, 1999*]. This problem involves an ideal gas in a 1D, two opened-ends shock tube, being forcefully emptied at 2.7 times the speed of sound. The plain red curve represents the exact analytical solution compared with the GMFIX solution obtained with MUSCL scheme [*van Leer, 1979*] with two different grid resolutions: 1x408 and 1x1632 and with a 2nd order or 1st order accurate time discretization scheme. As in Figure 5, all axes are dimensionless. **A**: Pressure. **B**: Density. **C**: Velocity. **D**: Temperature (specific Internal Energy) vs. position in the shock tube. Notice the little (minor) over-shoot in the energy numerical solution which is because of the vacuum condition in the middle of the tube (hence creating a zero-by-zero division). The "123" problem typically tests the "robustness" (in addition to accurateness) of numerical schemes applied to the energy PDE under vacuum conditions, which is, in this case, excellent.

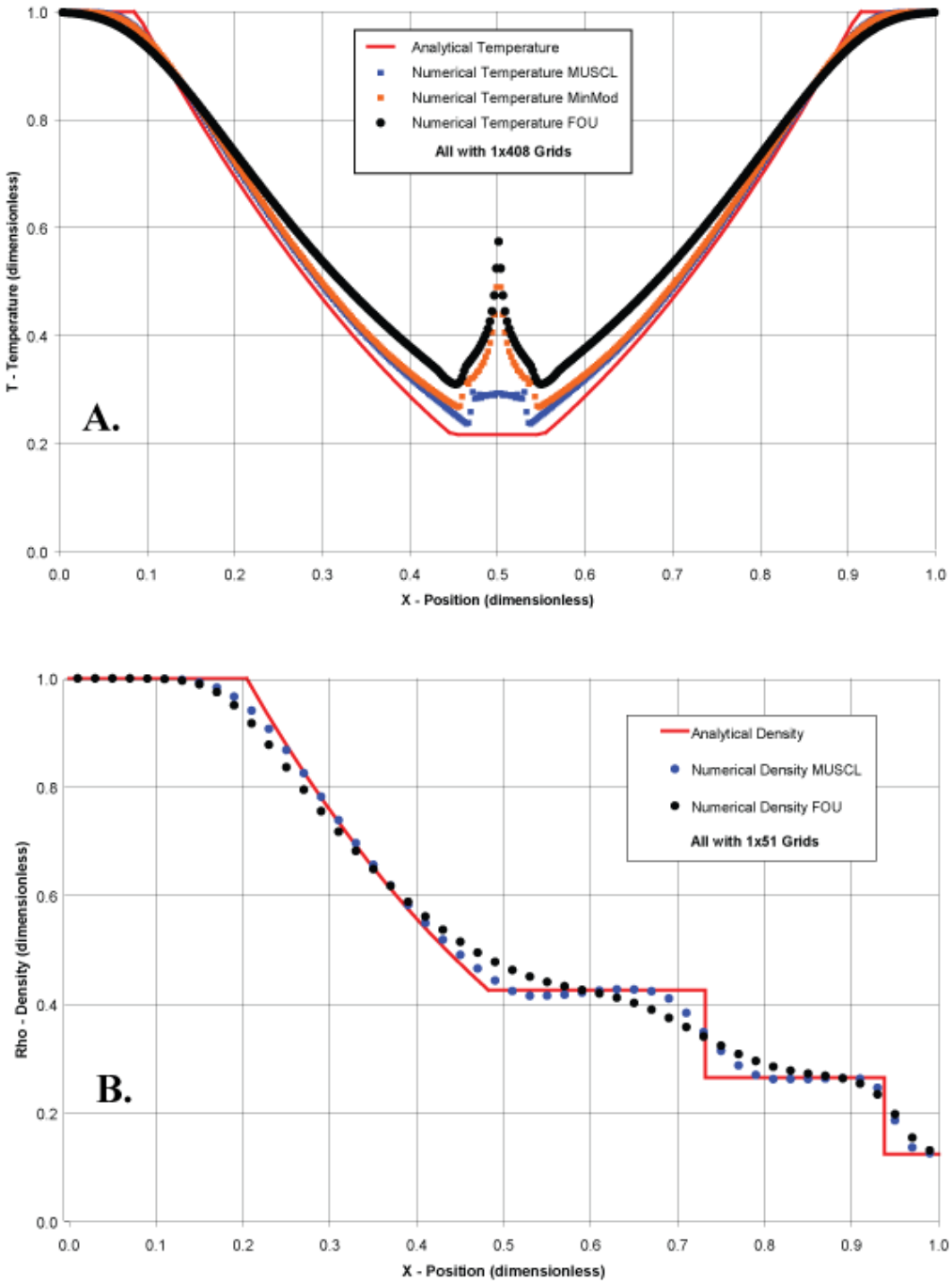

Figure 7

Same as Figure 5 and 6 but applied to numerical conditions where the "quality" of the numerical results is less than ideal. All axes are dimensionless. **A**: The "123" Problem for the temperature numerical results on a 1x488 grid resolution with the 1st order accurate FOU scheme (black plain dot) and with the 2nd order accurate, MINMOD scheme (orange plain square) compared with the 2nd order accurate, MUSCL scheme (blue plain square). As expected the FOU scheme does not produce "accurate" results, but neither the second order accurate scheme MINMOD. For this test-case, it turns out that only MUSCL scheme is robust to handle the vacuum conditions imposed in the middle of the tube. Compared also with Figure 6D. **B**: The Sod Problem for the density numerical results on a 1x51 grid resolution with the 1st order accurate, FOU scheme (black plain dot) compared with the 2nd order accurate, MUSCL scheme (blue plain square). As expected, the FOU scheme produces results off the exact solution (plain red curve). When compared with Figure 5D, clearly, the higher the grid resolution, the more accurate the numerical results, even with a second order accurate scheme.

4.2. Validation of the model

As explained above, the goal of validation analysis is to ensure that the conceptual model and its implementation into a code are the right theoretical and numerical tools for modeling the "real world." In the science of explosive volcanology, "real world" physics covers a wide range of spatial and temporal scales and of flow dynamisms. In addition, given the inherent danger of such events, the physical phenomenology is poorly constrained by *in situ* measurements and real-time field data. A few attempts to *qualitatively* validate the model against geophysical-volcanological flows have been achieved recently, e.g., against the height of plinian columns [*Dartevelle et al., 2004*] or against the 1977 explosive eruption of a basaltic magma through an Icelandic geothermal borehole [*Dartevelle and Valentine, 2007*]. Yet quantitative validations against well-constrained experiments are still needed in order to properly "quantify" the credibility and validity of a conceptual model and its implementation. Rather than validating a model against the whole phenomenology, we suggest validating against small-scale, highly constrained, and well-understood analog experiments covering the same physics as the ones found in the large-scale natural event: viz., supersonic and turbulent dynamisms.

Table 4 and 5 present the geometrical, boundary, and numerical properties used for all the validation simulation test cases (which are also summarized in Figure 8 for the supersonic jet case and Figure 13 for the turbulent jet case). The illustration on the right of Figures 8 and 13 further describes a typical case of jets generated during these validation simulations. Table 6 details the common physical properties used for all simulations.

Table 4

A Cylindrical Geometrical Setup: Validation Against Underexpanded Jets

Radial Length X [m], including the casing wall[1]	0.105
Radial Resolution ΔX [m][1]	0.5×10^{-3}
Number of Grid-Points in the X-Direction	210
Vertical Length Y [m][1]	0.17
Vertical Resolution ΔY [m][1]	0.5×10^{-3}
Number of Grid-Points in the Y-Direction	340
Inlet radius [m][1,2]	3.5×10^{-3}
Top outlet radius [m][1]	0.1045

Notes

[1]: see Figure 8

[2]: All validation test cases were obtained with this exact configuration described here, except, for illustration purposes, the simulations shown on Figure 8 (right side), Figure 9, and Figure 12. For these simulations, the inlet radius was 5 mm. In Figure 11C, the dot for K = 3 is the one from Figure 9.

B Cylindrical Geometrical Setup: Validation Against Turbulent Jets

Radial Length X [m], including the casing wall[1]	3.2×10^{-2}
Radial Resolution ΔX [m][1]	Variable: from 0.61×10^{-3} to 2.0×10^{-3}
Number of Grid-Points in the X-Direction	30
Vertical Length Y [m][1]	0.52
Vertical Resolution ΔY [m][1]	Variable: from 2.8×10^{-3} to 1.3×10^{-2}
Number of Grid-Points in the Y-Direction	50
Core inlet radius [m][1]	1.1×10^{-2}
Top outlet radius [m][1]	3.0×10^{-2}

Notes

[1]: see Figure 13

Table 5

Numerical Properties for all Validation Simulations

	Underexpanded Jets	**Turbulent Jets**
Geometry	Cylindrical	
Spatial Discretization	MUSCL (2^{nd} order accurate)	
Time Discretization	1^{st} order accurate	
Linear-Equation Solver	BI-CIGSTAB	
Inlet boundary	constant Mass Flux inflow (MI)	
Outlet boundary	constant Pressure & Temperature outflow (PO)	adaptive Pressure[1] outflow (OF)
Wall	Free-slip wall (all phases)	No-slip wall (all phases)

Notes

[1]: the turbulent jet is treated as an isothermal flow, hence only the pressure changes at the outlet.

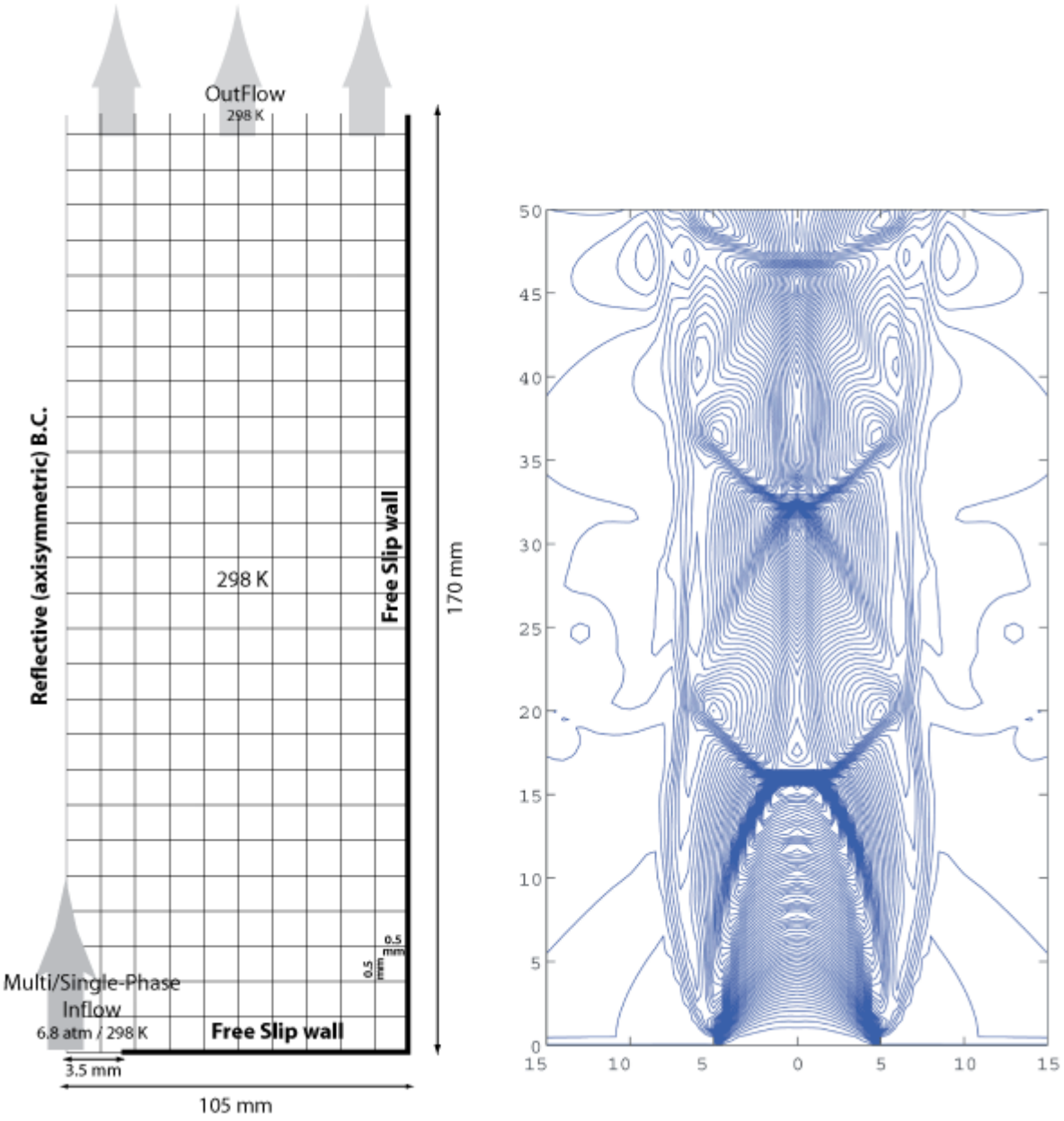

Figure 8

Validations against supersonic and under-expanded single- to multi-phase jet analog experiments. Left: Cylindrical geometry, grid configuration, initial and boundary conditions. All simulations were performed on a uniform grid of 0.5 x 0.5 mm (see Table 4A & 5). Right: A typical jets which show three Mach disk. Note all the classical structure of these jets: incidents, reflected shocks, slip lines, and expansion fans (see also Figure 9). Only the exact position of the first Mach disk is relevant for the validation tests.

Table 6

Initial and Boundary Physical Properties for All Validation Simulations

	Simulations	Underexpanded & supersonic Jets	Turbulent Jets (light particles)	Turbulent Jets (heavy particles)
Domain	Pressure [Pa]	Variable (depends on the simulation)[1]	$1.01x10^5$	$1.01x10^5$
	Temperature [K]	298	298	298
	Volumetric Solid Concentration [vol.%][2]	0	$1x10^{-8}$	$1x10^{-8}$
	Kappa (gas phase turbulent production) [m^2/s^2]	NA[3]	0.1	0.1
	Epsilon (gas phase turbulent dissipation) [m^2/s^3]	NA[3]	1.6	1.6
	Theta (granular temperature) [m^2/s^2]	NA[3]	0.01	0.01
Inlet	Temperature [K]	298	298	298
	Gas Pressure [Pa]	6.90×10^5	$1.01x10^5$	$1.01x10^5$
	Grain Diameter[4] [m]	$25x10^{-6}$	$81x10^{-6}$	$64x10^{-6}$
	Grain Density[4] [kg/m^3]	2,500	280	2,590
	Volumetric Solid Concentration[4] [vol.%]	Variable (depends on the simulation)[1]	Variable (depends on the radial position)[5]	
	Gas Vertical Speed [m/s]	346	Variable (depends on the radial position)[5]	

	Simulations	Underexpanded & supersonic Jets	Turbulent Jets (light particles	Turbulent Jets (heavy particles)
Inlet (cont.)	Particle Vertical Speed [m/s]	173	Variable (depends on the radial position)[5]	
	Theta, Granular Temperature (solid phase turbulent production) [m^2/s^2]	NA[3]	Variable (depends on the radial position)[5]	
	Solid Inelastic Collisional Dissipation coefficient	NA[3]	0.8	
	Kappa (gas phase turbulent production) [m^2/s^2]	NA[3]	Variable (depends on the radial position)[5]	
	Epsilon (gas phase turbulent dissipation) [m^2/s^3]	NA[3]	Variable (depends on the radial position)[5]	
Outlet	Gas Pressure [Pa]	Variable (depends on the simulation)[1]	NA	
	Gas Temperature [K]	298	NA	

Notes

[1]: The underexpanded and supersonic jet simulation have been performed in maintaining the pressure at the nozzle (P_n) the same for all experiments but in changing the pressure in the domain (P_∞) so that $K = P_n / P_\infty = 2$, 5, 10, 20, and 30

[2]: A volumetric concentration of 1.0×10^{-8} is equivalent to no particle in the domain, yet this low concentration is nevertheless specified to maintain a smoother and easier convergence of the turbulence PDEs.

[3]: The particle-gas turbulence model is not used for the supersonic underexpanded jets

[4]: This is only for the multiphase flow cases, all experiments were also achieved for single phase case (pure gas, no grains)

[5]: Instead of one fixed value, these are radial profiles given by Figure 14 and 15.

Validation against under-expanded jets

Thorough laboratory studies of momentum-driven single- to multi-phase supersonic and under-expanded jets [e.g., *Ladenburg et al., 1949; Lewis and Carlson, 1964; Kieffer, 1984*] provide quality and well-constrained analog experimental data to validate numerical codes against such phenomenology.

An under-expanded jet is defined by a pressure at the nozzle, P_n, higher than the pressure in the expansion room, P_∞:

$$K = \frac{P_n}{P_\infty} \tag{60}$$

Similarly, an over-expanded jet is when $K < 1$, and a matched jet is when $K = 1$.

On a qualitative level, Figure 9 shows all the classic properties of under-expanded jets one would expect from a code like GMFIX. As the gas leaves the overpressurized nozzle, it over-expands to form the expansion fans. The ambient gas in the chamber then acts as a piston and pushes the jet gas backwards along characteristic paths towards the centerline of the jet to form a converging conical shock called the *incident shock*. If the value of K is close to one, this incident shock reaches the jet axis at some punctual position. The incident shock thereafter undergoes a regular reflection to form a diverging outward shock called the *reflected shock*. However, if $K<<1$ or $K>>1$ as in Figure 9, then, rather than converging to a unique point on the jet axis, this incident shock reflects itself at the edge of the Mach disk. The Mach disk, which is a shock normal to the flow direction, can only be found in strongly under-expanded/over-expanded jets. As soon as this reflected shock reaches the jet boundary, it pushes outward the jet boundaries to create new rarefaction (expanding) fans and to cause the process to begin again (see Figure 8 & 9). In Figure 9, a clear and important property of these jets is the emergence of *slip discontinuities* from the *shock triple point* where the Mach, the incident, and reflected shocks all meet. This discontinuity arises because the thermodynamical pathway through the incident and reflected shocks does not equal the pathway through the sole Mach disk. Consequently, the flow velocity, density, and temperature are not equal across the slip discontinuity.

From the Bernoulli's principle, the total specific energy (i.e., kinetic and internal) along any streamline must remain equal. In addition, at any downstream location, two adjacent fluid parcels along a streamline must also have the same pressure. However, a fluid parcel which crossed the Mach disk is much more shock-heated along a Hugoniot than a fluid parcel crossing the weaker incident and reflected shocks. Hence, the Mach-heated fluid parcel has higher internal specific energy; in order to preserve the total specific energy (Bernoulli's principle), it must have lower kinetic specific energy than the adjacent fluid parcel on the other side of the slip discontinuity. Hence this discontinuity results from a velocity difference on each of the slip lines.

On a quantitative validation level, the position of the first Mach disk for under-expanded jets is known empirically as a function of both the pressure ratio, K, and the particle mass fraction at the nozzle, χ:

$$\chi = 1 - \left[\frac{\frac{\overline{\rho}_s \, \overline{\rho}_g}{\overline{\rho}_{mix}} - \overline{\rho}_g}{\overline{\rho}_s - \overline{\rho}_g} \right] \quad , \tag{61}$$

where the mixture density of a two-phase dust-gas flow must be, $\overline{\rho}_{mix} = \hat{\rho}_s + \hat{\rho}_g$. *Ladenburg et al.* [*1949*] and *Lewis and Carlson* [*1964*] have experimentally showed that the higher the value of K, the further downstream (i.e., the further away from the nozzle) the position of the first Mach disk. The higher the value of χ, the further upstream (i.e., the closer to the nozzle) the position of the first Mach disk. In our validation experiment we used values for K of 2, 5, 10, 20, and 30, where the inlet pressure (P_n) remains the same ($6.9 \cdot 10^5$ Pa) for all experiments; i.e., the pressure in the domain decreases as K increases (see Table 6 and Figure 8).

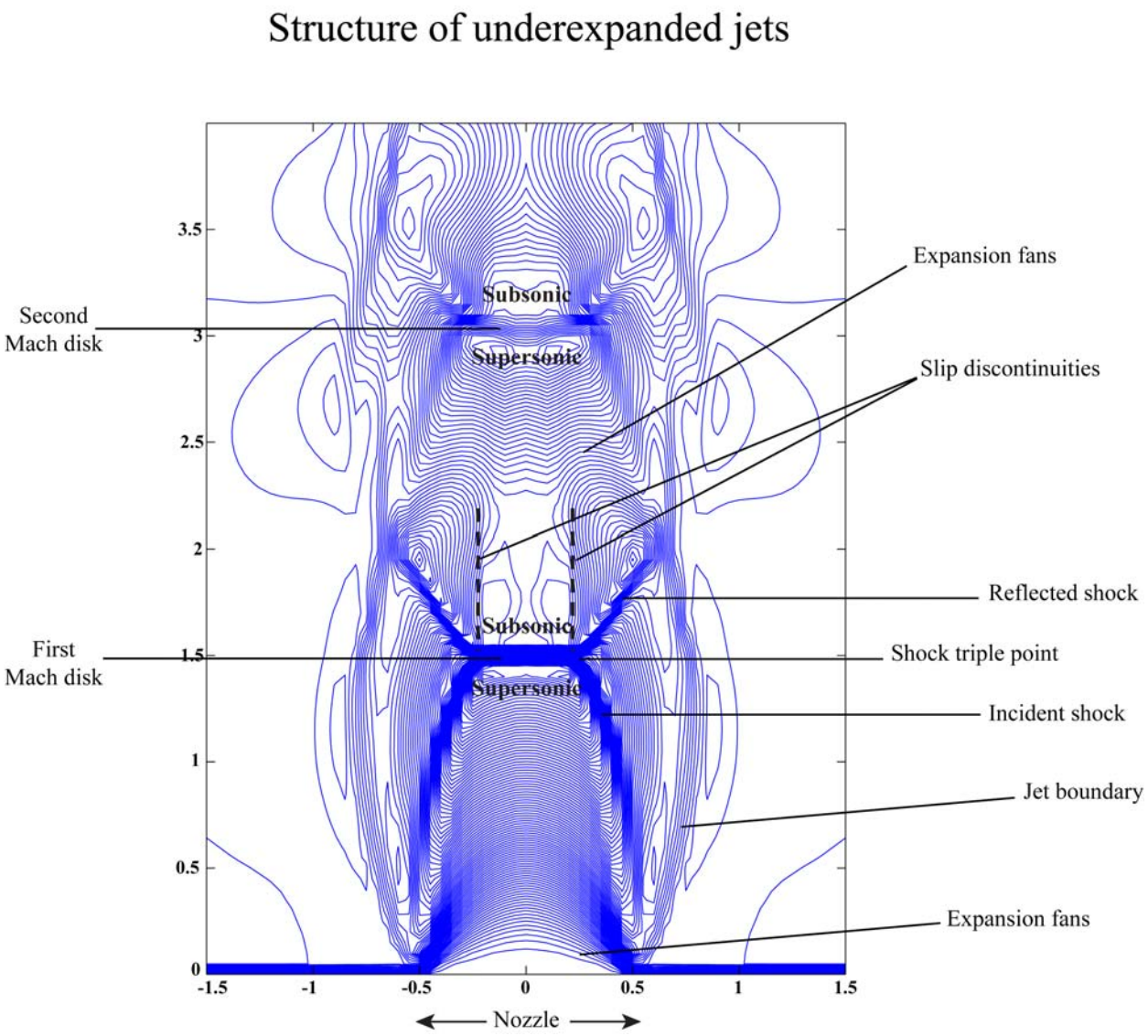

Figure 9

Qualitative properties of an under-expanded jet obtained by GMFIX. Inlet has a radius of 5 mm with a pressure of $5.52 \cdot 10^5$ Pa (the pressure in the chamber is 3 times lower). Axes are dimensionless (normalized by the diameter of the inlet).

Figure 10 shows the shape and size of single-phase (gas) jets fully developed along with the position of their first Mach discs. As expected, as K increases, the position of the first Mach disk moves downstream and the overall jets becomes, wider and higher [*Ladenburg et al., 1949; Lewis and Carlson, 1964*]. This is further illustrated in Figure 11C which shows the downstream position of the first Mach disk *vs*. K empirically obtained from analog experiments of *Lewis and*

Carlson [*1964*] (plain blue curve) and numerically obtained from GMFIX codes (red dot). The agreement is clearly excellent.

Another important feature of under-expanded jets (especially in the volcanological context) is the exact effects of particles upon the position and shape of the Mach disk within the jet. Figure 11A shows the identical jet (K = 10) in the single-phase case (left) and in the multiphase case (right with χ=0.7). GMFIX simulations clearly show that not only the particles pull "down" the first Mach disk further upstream, but also change its overall shape: the Mach disk becomes wider and rounder.

On a quantitative level, Figure 11B shows the first Mach disk position *vs*. χ empirically obtained from the analog experiments of *Lewis and Carlson* [*1964*] (plain blue curve) and numerically calculated by GMFIX codes (red dot). The "error bars" around each red dot indicate the small uncertainty in exactly measuring the position of the Mach disk because of the tendency of the jet and its Mach disk to wiggle and fluctuate around an average position (shown by the dot itself). Within this uncertainty range, the agreement between analog and numerical experiments is again excellent.

Last but not least, it is important to keep in mind that even though the verification test cases have shown a clear independence between grid resolution and numerical results (Figure 5, 7B, and 6), the quality of the numerical results is nevertheless dependent on the chosen grid size (viz., the coarser, the poorer). As a corollary (Figure 12), one should always attempt to demonstrate the quality expectancy of a given simulation in reproducing the same simulation upon different grid sizes.

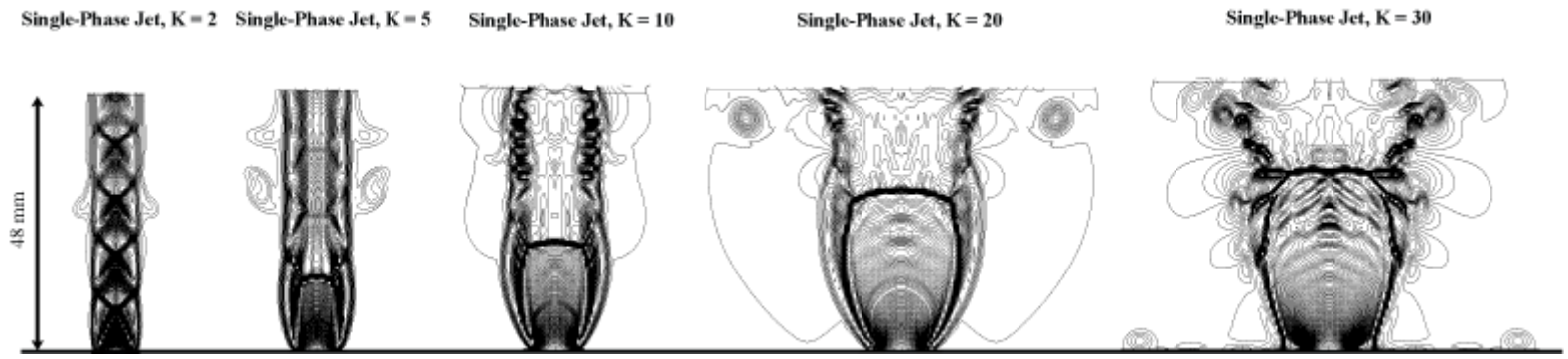

Figure 10

Different single-phase jets obtained with different K, viz., 2, 5, 10, 20, and 30. Notice how the first Mach disk moves downstream and becomes wider as K increases (see Table 4A & 6 for the initial and boundary conditions for these simulations).

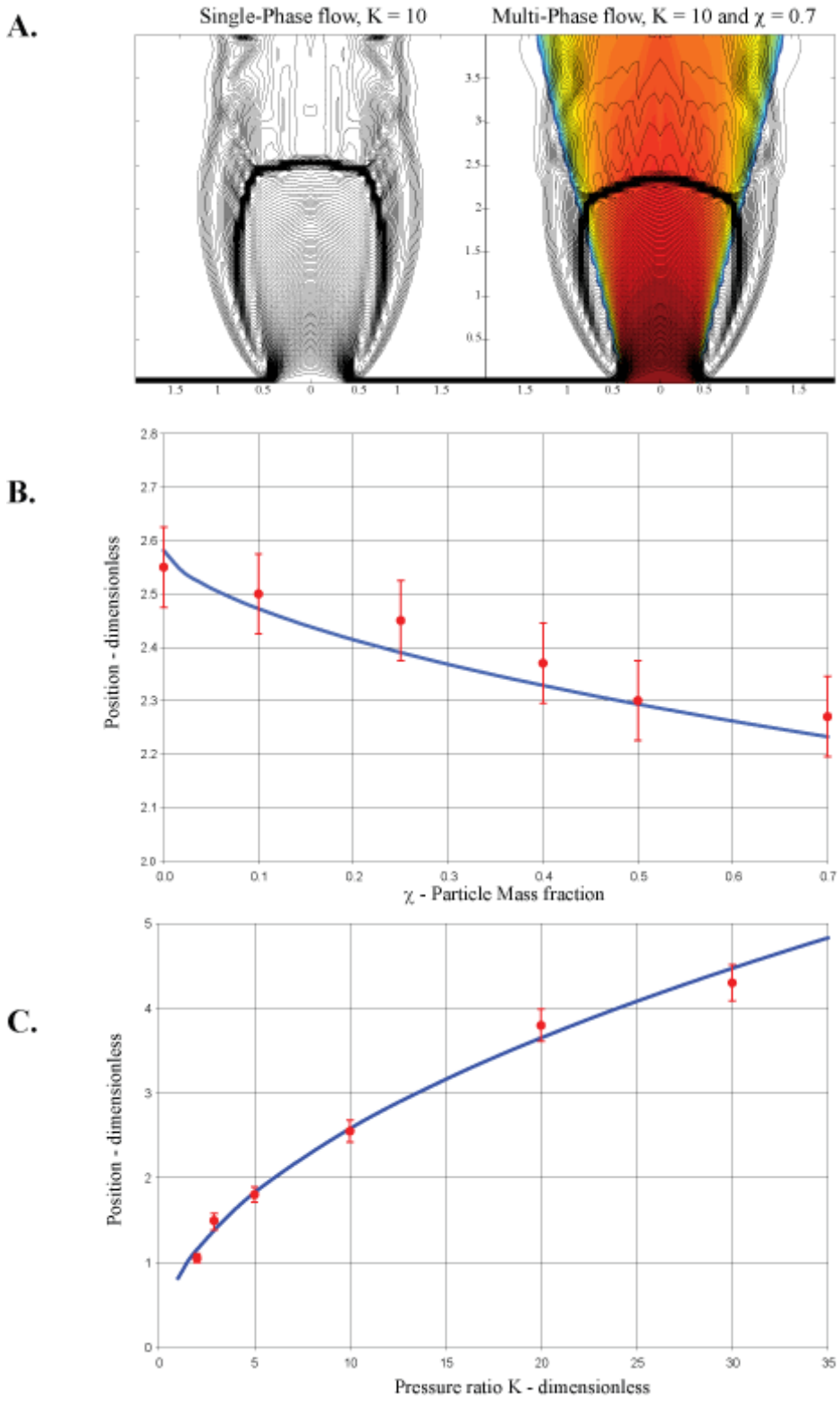

Figure 11

A: Two jets obtained with a Pressure ration of K = 10. Left-side, for a single phase flow (pure gas); right-side, for a multiphase flow (gas and particles) made of particles of 2500 kg/m^3, 25 µm, and a particle mass ratio, χ = 0.7. Notice how the first Mach disk, in the multiphase case, moved upstream and became wider and rounder. Axes are dimensionalized by the diameter length of the inlet. **B**: Position (dimensionless) of the first Mach disk *vs*. the mass fraction of particles in the jet (from 0, pure gas to 0.7). Blue plain curve is the position given by *Lewis and Carlson* [*1964*]'s empirical formula, red plain dot are the position given by GMFIX codes. The errors bars reflect the fact that there is no definitive stead-state and the Mach disk tends to slightly fluctuates around an averaged position. **C**: Position (dimensionless) of the first Mach disk *vs*. the pressure ratio at the nozzle, K. Note that the red dot at K = 3 is represented in Figure 9. The Higher K, the further away (downstream) the Mach disk. Same legend as in B. The agreement between experimental and numerical data is excellent.

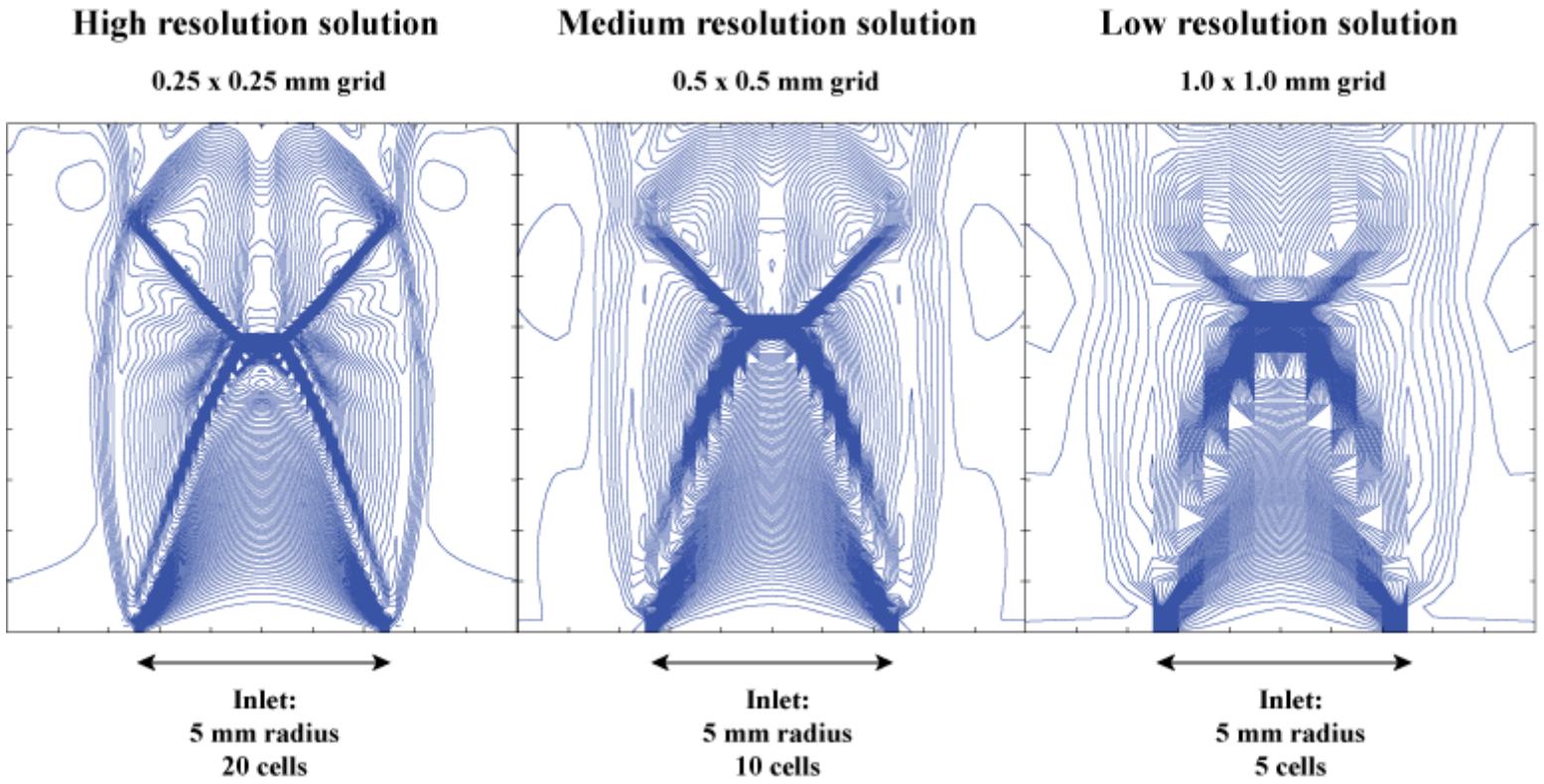

Figure 12

Effects of different grid-resolutions upon a same simulation's numerical solution. As already demonstrated in the Verification test cases, the solution (i.e., in this Figure, the position of the Mach disk) is independent of the grid resolution. However, the quality (rather than the accurateness) of the numerical solutions overall depends on the grid-size chosen. Axes are dimensionless.

Validation against turbulent jets

These validation test cases show the technical and physical adequacy of GMFIX for calculating the correct velocity and turbulent energy coupling between the gas phase and the dispersed phase within a matched, single to two-phases, highly turbulent (Re ~ 22,000), cylindrical, confined jet [*Hishida et al., 1987; Viollet et al., 1992*]. The experimental data were obtained by laser Doppler velocimetry measurements of a particle-laden jet discharged in a clean-gas stagnant surrounding. This Doppler technique is capable of particle-size discrimination in order to measure two-component velocities of gas and particles, and their fluctuations [*Hishida et al., 1987*]. The GMFIX turbulence model is based on separate transport equations for the components of the particulate stress tensor, and takes the inter-particle collisions into account using granular kinetic theory (as detailed in Appendix A, in *Dartevelle* [*2006a,b*], and in *Dartevelle and Valentine* [*2007*]).

Three sets of experiments were performed, viz., single phase gas, multiphase with low- and high-density particles but with particles within the same size range (i.e., 80 mm, 280 kg/m^3 and 64.4 mm, 2590 kg/m^3), with velocity and turbulent energies sampled at various downstream locations (viz., 0 cm, 6.5 cm, 13 cm, and 26 cm). The initial and the boundary conditions are set to exactly match the ones given by *Hishida et al.* [*1987*] (see Table 6, Figure 13). The experimental error measurements for both mean and fluctuating velocities are ~5% at the centerline of the jet and ~10% at the edges of the jet [Hishida, personal communication, 2006]. Therefore, the experimental error upon the turbulent energy is anywhere between 25% and 100%. The reader ought to be careful in the reading of Figure 14 & 15 as the error bars on the analog experimental data can be rather large. The analog experimental turbulent energy production for a given phase was calculated by:

$$k = \frac{v_r''^2 + 2 \cdot v_y''^2}{2} \quad , \tag{62}$$

where v_r'' and v_y'' are the measured velocity fluctuation of a given phase in the radial and axial direction respectively [Hishida, personal communication, 2006].

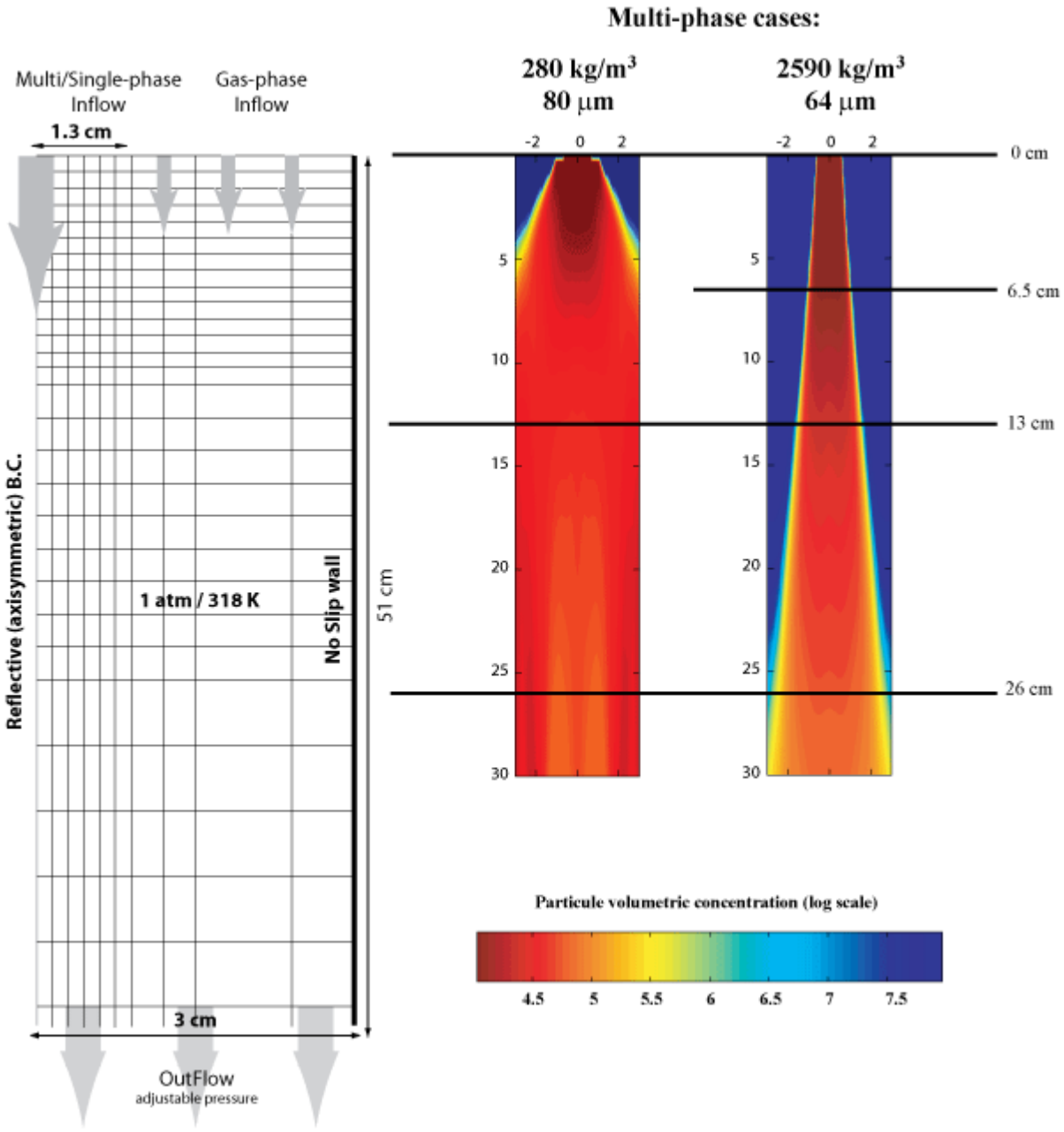

Figure 13

Validations against turbulent single- to multiphase jet analog experiments. Left: Cylindrical geometry, grid configuration, initial and boundary conditions. Note that the grid is non uniform (see Table 4B & 5) and the jet is falling down under gravity. Right: Snapshot of the jets in the multiphase case with low- (left, 280 kg/m^3, 80 μm) and high-inertial (right, 2590 kg/m^3, 64 μm) particles. The horizontal lines at positions 0 cm, 6.5 cm, 13 cm, and 26 cm represent the sampling positions in the analog experimental and numerical experiments (sampling at 6.5 cm was only achieved in the high-inertial particles case). Note: the redder, the more particles concentrated.

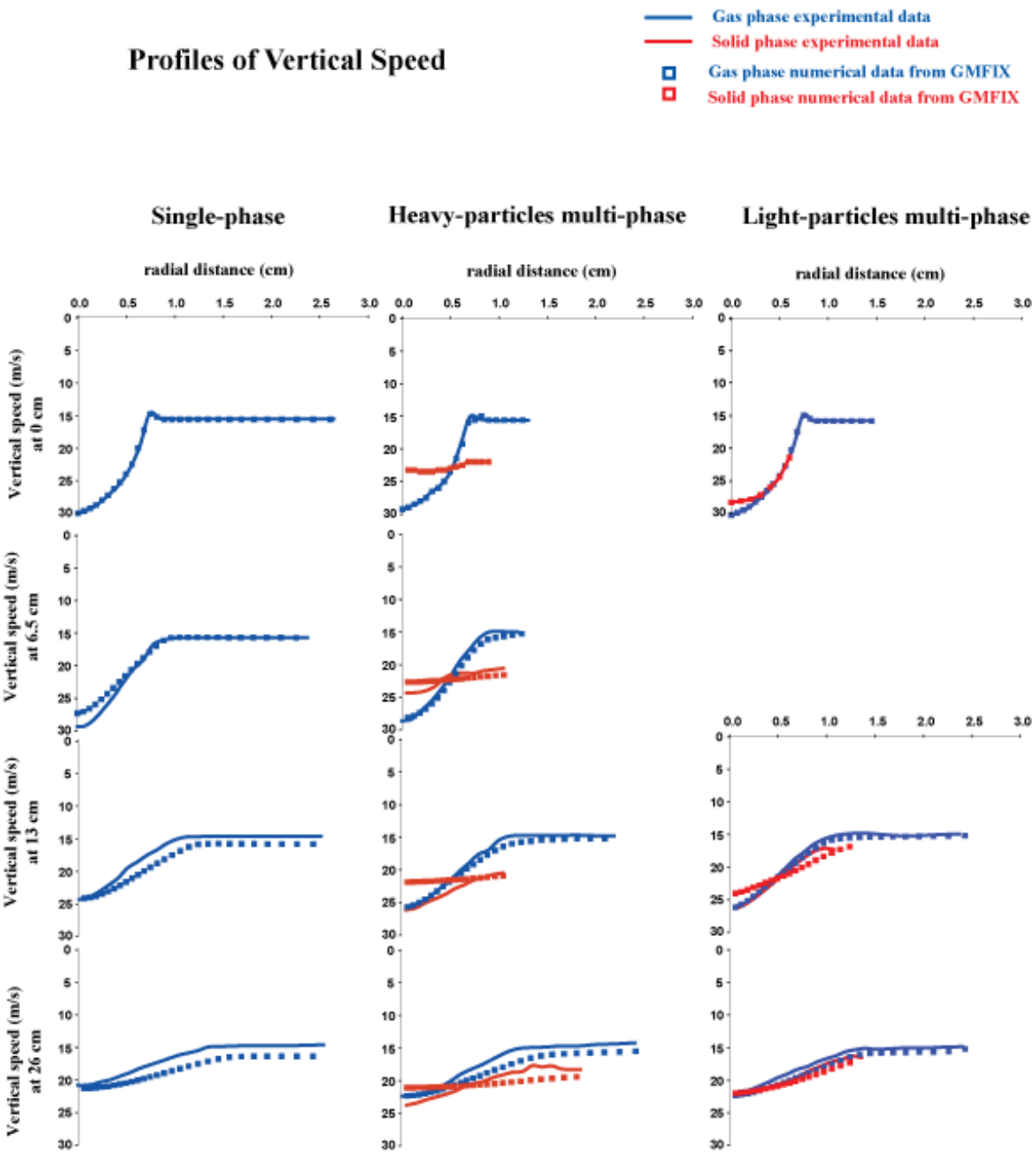

Figure 14

Profiles of axial speeds along the radial direction within the jet. Left, single-phase (gas) flow; Middle, for multiphase flow with high-inertial particles; Right, for multiphase flow with low inertial particles. Samplings at 0 cm (inlet), 6.5 cm, 13 cm, and 26 cm downstream. Blue is the gas phase, red is the particle phase, plain curve from the analog experiments, opened square from GMFIX numerical codes. Note: the striking difference in the coupling between the gas phase with the low-inertia particle (tightly coupled) or high-inertia particles (loosely coupled). Generally speaking, the agreement between numerical and experimental data is excellent and within 10 %. The only exception is at 13 cm for the high-inertia particles. The experimental errors on speed is 5 % within the jet core and up to 10 % towards its edges {Hishida, personal communication, 2006].

The comparison of mean axial gas and particle speed distribution with the experimental data (Figure 14) show excellent agreement within ~10 % at all downstream locations for the single-gas phase and multiphase, except small discrepancies at the 13 cm downstream location for the heavy particle case. One can also note that the light particles have a better coupling than the heavy particles, which is also well-captured by GMFIX. In addition, as experimentally [*Hishida et al., 1987*] and numerically confirmed (Figure 14), the addition of particles (particularly high-density particles) tends to increase the axial speed of the gas phase, particularly, at downstream locations.

In Figure 15, we compare the experimental data (plain curve) with GMFIX numerical data (opened square) of turbulent kinetic energy for both the gas phase (blue) and dispersed phase (red). If one keeps in mind the rather large error bar upon the kinetic energy measurements (~25% to ~100%), the numerical data agrees very favorably with the experimental ones. As in the analog experiments [*Hishida et al., 1987*], GMFIX also predicts –perhaps, even exacerbates– the reduction of the production rate of the gas phase turbulent energy when mixed with particles; the solid particles tend to disturb the production rate of the turbulent energy from the gas mean flow; this is particularly true for the heavy particles (Figure 15). However, because of the large experimental errors, one can also argue that for the multiphase cases, GMFIX may underestimate the production of kinetic energy, especially for the particulate phase. This underestimate could be mostly due because of an underprediction of the velocity fluctuation in the axial direction exacerbated by (i) the assumption that the local shaking of particles is “only” due to the gas phase turbulence [*Viollet et al., 1992*] (see Eq.(A.2) in Appendix A) and (ii) a simplistic (and questionable) approximation of the particle-gas covariance model as in the current version of GMFIX 1.62 [*Dartevelle, 2006a,b*]. Indeed, the production of fluctuating velocity cross-correlation turbulent energy, $k_{12}=\langle u'_g \cdot u'_s \rangle$ (see Eq.(A.3) in Appendix A), is not resolved by a full PDE approach but by a more simplistic algebraic expression. Obviously, in order to improve the multiphase turbulent prediction, it will be required to set a full PDE for the gas-particle covariance model.

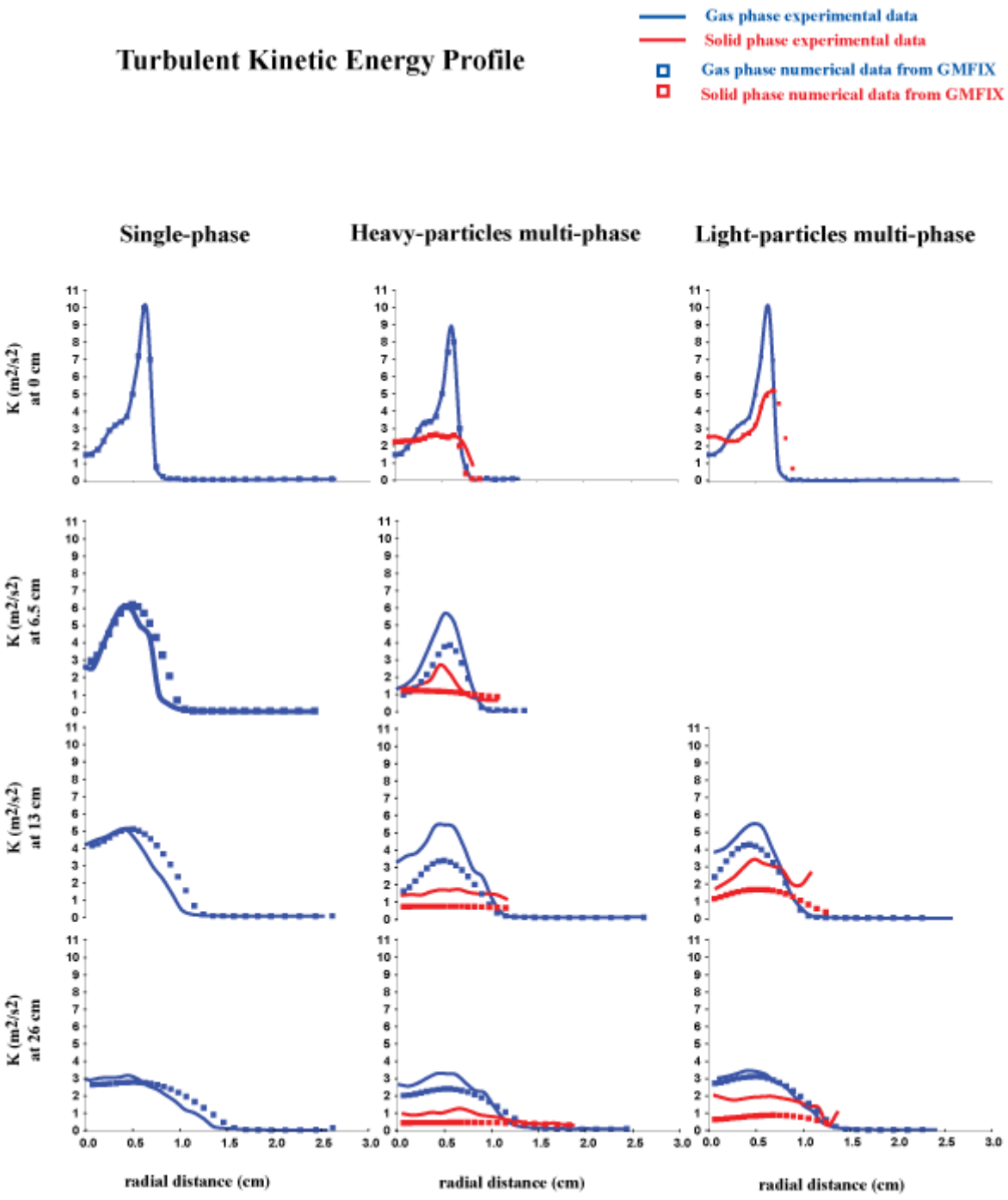

Figure 15

Profiles of the turbulent kinetic energy along the radial direction within the jet. Left, for a single-phase (gas) flow; Middle, for multiphase flow with high inertial particles; Right, for multiphase flow with low inertial particles. Samplings at 0 cm (inlet), 6.5 cm, 13 cm, and 26 cm downstream. Blue is the gas phase (k_1), red is the particle phase (k_2), plain curve from the analog experiments, opened square from GMFIX numerical codes. Generally speaking, the agreement between numerical and experimental data is excellent and within 10 % for single-phase flow. There is more discrepancy for k_2 between numerical and analog data however. However, one should keep in mind that the experimental errors in the determination of k_1 and k_2 is between 25% and 100%. This is because the turbulent energy is not directly measured but rather indirectly inferred from the fluctuating velocity fields which is measured with experimental errors between 5 to 10%.

5. Conclusions

This manuscript has reviewed the process of streaming a conceptual multiphase model into a multiphase code, verify the implementation, and validate the model against experiments representing the driving physics in explosive volcanology: turbulent and shock dynamics.

The first stage in the process was to conceptualize a multiphase flow hydrodynamic and thermodynamic model within both the RANS and the LES frameworks following *Dartevelle* [*2005*]. Within this conceptual model, the basic Partial Differential Equations are essentially the same for RANS and LES approaches to turbulence, even though the mathematical and physical meaning of these PDEs is radically different: *ensemble-averaged* (RANS) vs. *filtered* (LES) fields. Yet, because the hydrodynamic and thermodynamic PDEs share essentially the same basic "structure," they may be discretized within the same computer code with appropriate subroutines for turbulence/subgrid closures and for interfacial closures. *Dartevelle* [*2005*] also demonstrated that this model meets the necessary requirement for a well-posed initial value problem and is fully consistent with the second law of thermodynamics. The main asset of this model is its versatility with respect to the multiphase turbulence approaches; therefore, it would be possible to apply this model to different multiphase geophysical flows: gravity currents within the atmospheric boundary layer (near/at the ground) or "boundary-free" flows within the atmosphere (e.g., dusty plumes and jets).

The second stage was to correctly implement the conceptual model into a computer code. We have used GMFIX which is co-developed with the MFIX team (http://www.mfix.org). Both MFIX and GMFIX are general-purpose hydrodynamic codes for describing chemical reactions, heat transfer, particulate transport in dense or dilute fluid-solids flows under transient conditions. These codes are written in FORTRAN for multiple particle types, three-dimensional Cartesian or Cylindrical coordinate systems on uniform or non uniform grids, energy balances, and gas and solids species balances. MFIX/GMFIX calculations give time-dependent information on pressure, temperature, composition, and velocity distributions in the reactors. GMFIX uses portable OPEN-MP (for shared memory multi processors) and MPI (for distributed memory parallel computers) in a unified source code.

The last and third stage was to thoroughly verify the model implementation and validate the whole model within turbulence or shock dynamics for single- to multiphase flows. We have shown that the model implementation (i.e., the codes) passes the verification phase and, although there is room for improvement (especially for multiphase turbulence), the model as a whole favorably passes the validation phase, indicating that it is capable to qualitatively and accurately capture the essential features of multiphase and single-phase turbulence and shock dynamics. In addition, we have also shown within both the verification and validation context that the accurateness of the numerical results tends to be independent on the chosen grid-resolution, even though the “quality” (rather than the precision) of the numerical solution tends to lessen with coarser and coarser grid-size.

Overall, a passing V&V analysis is a fundamental requirement to quality assure, not only a model and its implementation, but also all its subsequent numerical results. This provides a powerful argument to scientists and volcanologists to convince policy makers and the public of the soundness and trustworthiness of their numerical results.

Appendix A: RANS turbulence PDE

Note: The following, in both MFIX and GMFIX codes, is generalized to many particle-phases (different density and/or size). However, since the validation test-cases of this turbulent model were achieved within a two-phase system, we only present this model for a system made of gas and one particle phase. For a generalization to i particle-phases, see *Dartevelle* [*2006a,b*].

The two-phase flow turbulence model can be understood as a competition between different time scales defined from key physical phenomenology between the gas and the dispersed phases [*Simonin, 1996; Ferschneider and P. Mege, 2002; Benyahia, 2005*], viz.:

• The gas-phase turbulence, which is characterized by gas phase turbulence time-scale (Lagrangian time-scale or eddy-turn over time-scale), t_1;

• The coupling between the fluctuating motion of the gas and the agitation of the particles, characterized by the fluctuation time of the fluid as seen by the particles ("eddy-particle interaction time"), t^t_{12};

• The entrainment of the solid particles by the motion of the gas, characterized by the *particle relaxation time* t^x_{12}, direct function of the inertia of the particles and the drag. At the limit, if $t^x_{12}>>$, particles are ballistic and if $t^x_{12}<<$, the particles are passive tracers;

• The collisions between particles, characterized by the characteristic time between the collisions ("inter-*particle collision time*"), t^c_2;

• The last two mechanisms are in competition and can be characterized by the *particle dissipation time*, t_2, defined as the harmonic mean of the particle relaxation time and of the particle collision time, $\frac{1}{t_2} \sim \frac{1}{t^x_{12}} + \frac{1}{t^c_2}$.

In order to quantify the importance of the different physical mechanisms involved in gas–solid flow turbulence, their time-scales can be compared:

• $t_1 \leq t_2$, the dominant mechanisms are inherent to the gas phase. The time between two collisions is large; therefore, the motion of the particles is considered to be statistically independent. This

regime is called the *dilute regime* and is encountered only at low solid volume fractions ε_s<0.1 vol.%. Depending on their relaxation times the particles behave differently from the gas turbulence. If t^x_{12}>>, particles are not affected by the gas turbulence (whether collisions exist or not); but if $t_1<t^x_{12}<t^c_2$, the main dissipative scale is the gas turbulence and the drag between the particle and the gas (particle collision is non existent).

• $t_1 \gtrsim t_2$, this situation emerges at large solid volumetric fractions ε_s>10 vol.%. This is the *collisional regime*. In this case, the internal momentum transport in the solid phase is dominated by particle–particle collisions. The granular motion is only *slightly* perturbed by the presence of the gas. Indeed, if t^x_{12}> and t^c_2<, then the gas–particle interactions are small; if $t^x_{12} \approx t_2$ and t^c_2<<, then the motions of the two-phases are coupled but collisions is the only dissipative mean.

• $t_1 \approx t_2$, the gas–particle and particle–particle interactions are in competition. This intermediate regime is called the *kinetic regime*. The granular motion is *highly* perturbed by the presence of the gas. If $t^x_{12}<<t_1<<t^c_2$, the motion of the particles is controlled by the turbulence of the gas (barely by collisions). In the opposite case, $t^c_2<<t_1<<t^x_{12}$, each phase's behavior seem to be uncorrelated, but the gas must influence the transport properties of the particles in limiting the mean-free path.

It can be easily seen that eddy-viscosities of the gas and dispersed phases can be written as functions of these time scales and the amount of turbulent kinetic energies.

Granular temperature equation (or k_2-equation)

Let k_2 be the fluctuating kinetic energy of the dispersed phase, then

$$\left[\frac{\partial \hat{\rho}_s k_2}{\partial t} + \nabla \cdot \hat{\rho}_s k_2 \tilde{\mathbf{u}}_s\right] = \hat{\rho}_s\left(-\tilde{\mathbf{T}}_s : \nabla \tilde{\mathbf{u}}_s\right) - \nabla \cdot \mathbf{q}_\Theta + \Pi_\Theta - \Sigma_\Theta \qquad \text{(A.1)}$$

where the granular temperature, Θ is defined as $\Theta = \frac{2}{3} k_2$ and $k_2 = \left\langle \mathbf{u}''_s \cdot \mathbf{u}''_s \right\rangle$ [*Dartevelle, 2004*].

The first term on the RHS is the production of granular temperature through viscous dissipation; $\mathbf{q}_\Theta$ is the conduction of granular temperature; Π_Θ and Σ_Θ are respectively the source and sink terms of k_2. With the exception of a new source term (from gas phase turbulence), Π_Θ, all the

other granular temperature terms are thoroughly defined in *Dartevelle* [*2004; 2006a,b*] and will not be repeated herewith:

$$\Pi_{\Theta} = K_{sg}\left(k_{12} - 2k_2\right) \tag{A.2}$$

where K_{sg} is the drag function and k_{12} is the gas-solid covariance (turbulent) energy.

Gas-solid covariance (k_{12}-equation)

Let k_{12} be the production of fluctuating gas-solid dispersed phase kinetic energy given by:

$$k_{12} \approx \frac{2\,\dfrac{t^t_{12}}{t^x_{12}}}{1+\dfrac{t^t_{12}}{t^x_{12}}\left(1+X_{12}\right)}\left(k_1 + X_{12}k_2\right) \tag{A.3}$$

where $k_{12} = \left\langle \mathbf{u}''_s \cdot \mathbf{u}''_g \right\rangle$ and $X_{12} = \hat{\rho}_s \big/ \hat{\rho}_g$. In GMFIX 1.62, only an algebraic expression is solved instead of a full PDE. In this equation, t^t_{12} is the crossing trajectory time scale (the eddy-particle interaction time); t^x_{12} is the particle relaxation time scale; X_{12} is the mass-weighted concentration ratio; and k_1 is the turbulent kinetic energy of the carrier phase. This model is based on a competition between different time scales seen and/or induced by the presence of the particles and seen by the carrier phase. The turbulent eddy characteristic time-scale of the carrier phase:

$$t_1 = \frac{3}{2} C_{\mu} \frac{k_1}{\varepsilon_1} \tag{A.4}$$

which is based on a competition between production of turbulent kinetic energy of the gas phase (k_1) and its dissipation (ε_1). The particle relaxation time-scale:

$$t^x_{12} = \frac{\varepsilon_s \overline{\rho}_s}{K_{sg}}\left(\frac{\overline{\rho}_g}{\overline{\rho}_s} + C_{\upsilon}\right) \tag{A.5}$$

The fluid Lagrangian integral time scale along the particle trajectories (characteristic time scale of the fluid turbulent motion viewed by the particle or eddy-particle interaction time):

$$t_{12}^{t} = \frac{t_1}{\sqrt{1+\frac{3}{2}C_\beta \frac{\left|\tilde{\mathbf{u}}_g - \tilde{\mathbf{u}}_s\right|^2}{k_1}}} \tag{A.6}$$

In these time-scales, C_v is the added mass coefficient; C_μ and C_β are turbulence constants [*Dartevelle, 2006a,b*].

Gas turbulent kinetic energy (k_1-equation)

Let k_1 be the turbulent kinetic energy of the carrier phase, then:

$$\left[\frac{\partial \hat{\rho}_g k_1}{\partial t} + \nabla \cdot \hat{\rho}_g k_1 \tilde{\mathbf{u}}_g\right] = \varepsilon_g \left(-\mathbf{R}_g : \nabla \tilde{\mathbf{u}}_g\right) - \nabla \cdot \varepsilon_g \mathbf{q}_{k1} + \Pi_{k1} - \Sigma_{k1} \tag{A.7}$$

where $k_1 = \left\langle \mathbf{u}_g'' \cdot \mathbf{u}_g'' \right\rangle$. The first term on the RHS is the production of k_1 through viscous dissipation; $\mathbf{R}_g$ is the Reynolds stress tensor; $\mathbf{q}_{k1}$ is the conduction of k_1; Π_{k1} and Σ_{k1} are respectively the source and sink terms of k_1:

$$\mathbf{q}_{k1} = -\frac{{}^{tur}\mu_g}{\sigma_{k1}} \nabla k_1 \tag{A.8}$$

$$\Pi_{k1} = X_{12} K_{sg} \left(k_{12} - 2k_1\right) \tag{A.9}$$

$$\Sigma_{k1} = \varepsilon_g \rho_g \ \varepsilon_1 \tag{A.10}$$

$$\mathbf{R}_g = 2\,{}^{tur}\mu_g \overset{\circ}{\mathbf{D}}_g + \frac{2}{3} k_1 \mathbf{I} = -{}^{tur}\mu_g \left[\nabla \tilde{\mathbf{u}}_g + \nabla \tilde{\mathbf{u}}_g{}^{T}\right] + \frac{2}{3}\left({}^{tur}\mu_g \nabla \cdot \tilde{\mathbf{u}}_g + k_1\right)\mathbf{I} \tag{A.11}$$

Gas turbulent dissipation (ε_1-equation)

Let ε_1 be the dissipation of the turbulent kinetic energy of the carrier phase, then:

$$\left[\frac{\partial \hat{\rho}_g \varepsilon_1}{\partial t} + \nabla \cdot \hat{\rho}_g \varepsilon_1 \tilde{\mathbf{u}}_g \right] = \varepsilon_g C_{1\varepsilon} \frac{\varepsilon_1}{k_1} \left(-\mathbf{R}_g : \nabla \tilde{\mathbf{u}}_g \right) - \nabla \cdot \varepsilon_g \mathbf{q}_{\varepsilon_1} + \Pi_{\varepsilon 1} - \Sigma_{\varepsilon 1} \tag{A.12}$$

where $\mathbf{q}_{\varepsilon 1}$ is the conduction of ε_1; $\Pi_{\varepsilon 1}$ and $\Sigma_{\varepsilon 1}$ are respectively the source and sink terms of ε_1:

$$\mathbf{q}_{\varepsilon 1} = -\frac{^{tur}\mu_g}{\sigma_{\varepsilon 1}} \nabla \varepsilon_1 \tag{A.13}$$

$$\Pi_{\varepsilon 1} = C_{3\varepsilon} \frac{\varepsilon_1}{k_1} X_{12} K_{sg} \left(k_{12} - 2k_1 \right) \tag{A.14}$$

$$\Sigma_{\varepsilon 1} = \varepsilon_g \rho_g \; C_{2\varepsilon} \frac{\varepsilon_1}{k_1} \varepsilon_1 \tag{A.15}$$

This model uses the following turbulence constants:

$C_\mu = 0.09$

$\sigma_{k1} = 1.00$

$\sigma_{\varepsilon 1} = 1.30$

$C_{1\varepsilon} = 1.44$

$C_{2\varepsilon} = 1.92$

$C_{3\varepsilon} = 1.20$

$C_\beta = 0.45$

$C_\nu = 0.50$

For a complete description of all the closures and constants used in this model, see *Dartevelle* [*2006a,b*].

Appendix B: Common operators, tensors and invariants

Operators

$\overset{\circ}{=}$		deviatoric part (traceless) of a symmetric tensor
$\circ$		spherical part (trace) of a symmetric tensor
$\tilde{\cdot}$		mean (RANS) or filtered (LES) part of a variable obtained by Favre *mass*-weighted decomposition
$\bar{\cdot}$		mean (RANS) or filtered (LES) part of a variable obtained by Favre *phasic*-weighted decomposition
$\breve{\cdot}$		obtained from or after a filtering process (LES framework)
:		scalar product of two tensors
.		scalar product of two vectors
$\| \ \|$		Euclidian norm of a tensor
$[\![\mathrm{X}]\!] = \begin{cases} 0 & \mathrm{X} \le 0 \\ \mathrm{X} & \mathrm{X} > 0 \end{cases}$		double bracket operator
$\langle \ \rangle$		ensemble-average (RANS) or filtering (LES) operator
tr		trace operation of tensors
T		transposed operation of matrices
∇	1/m	gradient operator
$\nabla\cdot$	1/m	divergence operator
$\frac{\mathrm{d}}{\mathrm{dt}} = \frac{\partial}{\partial \mathrm{t}} + \mathbf{u}\cdot\nabla$	1/s	material (Lagrangian) time-derivative

Tensors, invariants, and work terms

Rate-of-strain tensor:

$$\mathbf{D} = -\frac{1}{2}\left[\nabla\mathbf{u} + \nabla\mathbf{u}^{\mathrm{T}}\right] \qquad 1/\mathrm{s}$$

Deviator of the rate-of-strain:

$$\overset{\circ}{=}\mathbf{D} = \mathbf{D} + \frac{1}{3}\nabla\cdot\mathbf{u}\,\mathbf{I} \qquad 1/\mathrm{s}$$

First invariant of the rate-of-strain tensor:

$$\mathrm{I_D} = \mathrm{tr}(\mathbf{D}) = \sum_{\mathrm{i}=1}^{3}\mathrm{D_{ii}} = -\nabla\cdot\mathbf{u} \qquad 1/\mathrm{s}$$

Second invariant of the rate-of-strain tensor:

$$\mathrm{II_D} = \mathrm{tr}(\mathbf{D}\cdot\mathbf{D}) = \sum_{\mathrm{i}=1}^{3}\sum_{\mathrm{j}=1}^{3}\mathrm{D_{ij}D_{ji}} = \mathrm{D_{11}^2} + \mathrm{D_{22}^2} + \mathrm{D_{33}^2} + 2\,\mathrm{D_{12}^2} + 2\,\mathrm{D_{13}^2} + 2\,\mathrm{D_{23}^2} \qquad 1/\mathrm{s}^2$$

Second invariant of the deviator of the stress tensor:

$$\mathrm{II_{dT}} = \frac{\left(\mathrm{T_{11}} - \mathrm{T_{22}}\right)^2 + \left(\mathrm{T_{22}} - \mathrm{T_{33}}\right)^2 + \left(\mathrm{T_{33}} - \mathrm{T_{11}}\right)^2}{6} + \mathrm{T_{12}^2} + \mathrm{T_{13}^2} + \mathrm{T_{23}^2} \qquad \mathrm{Pa}^2\ (\mathrm{kg}^2/\mathrm{m}^2\,\mathrm{s}^4)$$

Second invariant of the deviator of the rate-of-strain tensor:

$$\mathrm{II_{dD}} = \frac{\left(\mathrm{D_{11}} - \mathrm{D_{22}}\right)^2 + \left(\mathrm{D_{22}} - \mathrm{D_{33}}\right)^2 + \left(\mathrm{D_{33}} - \mathrm{D_{11}}\right)^2}{6} + \mathrm{D_{12}^2} + \mathrm{D_{13}^2} + \mathrm{D_{23}^2} \qquad 1/\mathrm{s}^2$$

Total stress tensor:

$$\mathbf{T} = \mathrm{P}\,\mathbf{I} + \boldsymbol{\tau} = \mathrm{P}\,\mathbf{I} + 2\,\mu\,\overset{\circ}{=}\mathbf{D} - \mu^{\mathrm{b}}\,\nabla\cdot\mathbf{u}\,\mathbf{I} \qquad \mathrm{Pa}\ (\mathrm{kg/m\,s}^2)$$

Viscous dissipation (irreversible work):

$$\mathrm{W_{\boldsymbol{\tau}}} = -\boldsymbol{\tau} : \nabla\mathbf{u} = -\left(\nabla\cdot\left(\boldsymbol{\tau}\cdot\mathbf{u}\right) - \mathbf{u}\cdot\nabla\cdot\boldsymbol{\tau}\right) = 2\,\mu\,\mathrm{II_D} + \lambda\,\mathrm{I_D^2} \qquad \mathrm{J/m^3\,s}\ (\mathrm{kg/m\,s}^3)$$

Work of all surface forces:

$$W_{\mathbf{T}} = -\mathbf{T} : \nabla \mathbf{u} = -\left(P\mathbf{I} : \nabla \mathbf{u} + \boldsymbol{\tau} : \nabla \mathbf{u} \right) = -P \nabla \cdot \mathbf{u} - \nabla \cdot \left(\boldsymbol{\tau} \cdot \mathbf{u} \right) + \mathbf{u} \cdot \nabla \cdot \boldsymbol{\tau} = P\ I_D + W_{\boldsymbol{\tau}} \qquad J/m^3\ s\ (kg/m\ s^3)$$

Reynolds stress tensor:
(RANS framework only, where 'k' represents a production of turbulence kinetic energy)

$$\mathbf{R} = 2\,{}^{tur}\mu\, \mathring{\mathbf{D}} + \frac{2}{3} \rho\, k\, \mathbf{I} \qquad Pa\ (kg/m\ s^2)$$

Appendix C: Notations, units, constants, and acronyms

Latin

A_i		1/m (m^2/m^3)	"volumetric concentration" of interfacial area of phase i
a			advection term in the discretized equation
b			source term in the discretized equation
C_d		dimensionless	drag coefficient
$C_{i,j}$		kg/m^3 s	rate of interfacial mass transfer between species j and all other species within phase i
Cp		J/kg K(m^2/s^2 K)	specific heat at constant pressure
Cv		J/kg K (m^2/s^2 K)	specific heat at constant volume
d		m	particle diameter
dwf			downwind factor
D		1/s	rate-of-strain tensor
$\overset{\circ}{=}$ **D**			deviatoric part of the rate-of-strain tensor
E		J/kg (m^2/s^2)	total energy per unit of mass (internal + kinetic energy)
E_Θ		m^2/s^2	volume averaged granular fluctuating energy
G		m/s^2	body force
g	(0,0,-9.80665)	m/s^2	gravity vector
${}^{h}H_i$		J/s m^3 (kg/m s^3)	rate of interfacial enthalpy between phase i and all other phases
h		J/kg (m^2/s^2)	enthalpy per unit of mass
I		J/kg (m^2/s^2)	internal energy per unit of mass
I		dimensionless	unit tensor
k		W/m K (kg m/K s^3)	thermal conductibility coefficient
k_1		J/kg (m^2/s^2)	turbulent kinetic energy of the carrier phase
k_2		J/kg (m^2/s^2)	turbulent kinetic energy of the dispersed phase
k_{12}		J/kg (m^2/s^2)	covariant turbulent kinetic energy of the dispersed and gas phase
K		kg/m^3 s	momentum transfer (drag) function between phase
m		kg	mass of grain
M_a	28.9644	kg/kmol	molar weight of dry air
M_j		kg/kmol	molar weight of any gas species
$\mathbf{M}_i$		Pa/m (kg/m^2 s^2)	rate of interfacial momentum transfer between phase i and all other phases
M_w	18.0152	kg/kmol	molar weight of water
n		$1/m^3$	number of grains per unit of volume
Nu		dimensionless	Nusselt number
P		Pa (kg/m s^2)	pressure
${}^{tur}P_s$		Pa (kg/m s^2)	granular pressure (usually understood as a kinetic and collisional within RANS)
${}^{mol}Pr$		dimensionless	"molecular" (not induced by turbulence) Prandtl number
${}^{tur}Pr$	0.95	dimensionless	turbulent Prandtl number
q		kg/s^3	thermal-heat flux or granular-heat flux vector
r		m	position vector
Q		W/m^3 K (kg/s^3 K)	gas-solid heat transfer function
R	8314.56	J/kmol K (kg m^2/s^2 kmol K)	universal gas constant
$\ddot{\ddot{R}}$		J/kg K (m^2/s^2 K)	mixture gas constant
Re		dimensionless	particle Reynolds number
R_i		kg/m^3 s	rate of interfacial mass transfer between phase i and all other phases
R		Pa m^3/kg (m^2/s^2)	specific Reynolds stress tensor (RANS)
S		J/kg s (m^2/s^3)	rate of heat/energy supplementary source
t		s	time
T		K	temperature
T		Pa (kg/m s^2)	total stress tensor
u		m/s	velocity vector
$\mathbf{u}_{Int}$		m/s	bulk velocity vector of all the interfaces
U_x		m/s	mean mixture horizontal/radial-speed of all phases
V_y		m/s	mean mixture vertical-speed of all phases

V		m^3	volume of a cell
$W_{\mathbf{T}}$		$J/m^3\ s\ (kg/m\ s^3)$	total work done by all the surface forces
$W_{\boldsymbol{\tau}}$		$J/m^3\ s\ (kg/m\ s^3)$	irreversible work done by the surface forces (viscous dissipation)
X_i	1 or 0	dimensionless	function of presence of the i^{th} phase
y		dimensionless	species mass fractions

Greek

Δ		m	3D geometric mean of the computational grid-size
ε		dimensionless	phasic volumetric concentration
ε_1		$J/kg\ s\ (m^2/s^3)$	dissipation of the turbulent kinetic energy of the carrier phase
$^{max}\varepsilon_s$	0.64	dimensionless	maximum solid volumetric concentration
$\boldsymbol{\Phi}$		$kg/K\ s^3$	entropy flux
ϕ			a scalar dummy function (temperature, energy, dissipation)
$\ddot{\phi}$			normalized universal limiter of ϕ
Γ		$k/s\ m^3$	source/sink of a given species
Γ			some "dummy" diffusion coefficients
ι		s or m	generic symbol for the time- or a space-variable
$\lambda = \mu^b - \frac{2}{3}\mu$		Pa s (kg/m s)	second coefficient of viscosity
μ		Pa s (kg/m s)	shear viscosity
μ^b		Pa s (kg/m s)	bulk viscosity
η		$J/kg\ K\ (m^2/s^2\ K)$	entropy per unit of mass
Θ		$J/kg\ (m^2/s^2)$	granular temperature
ρ		kg/m^3	microscopic weight density
$\hat{\rho}$		kg/m^3	macroscopic weight density
ρ_m		kg/m^3	mean mixture weight density between all phases
Σ		$kg/m\ s^3$	sink of turbulent energy or of dissipation of the turbulent energy
$\boldsymbol{\tau}$		Pa $(kg/m\ s^2)$	viscous stress tensor
ϖ_j		m^2/s	diffusion coefficient of species j in the whole mixture
ξ			weighting factor equal to dwf
$\ddot{\xi}$			weighting factor equal to 1-dwf

Subscripts-Superscripts

0	previous time step
1	pertains to the carrier phase
2	pertains to the dispersed (particle or tephra) phase
12	pertains to both the carrier phase and dispersed phase (e.g., covariance turbulent kinetic energy)
$'$	fluctuating (RANS) or unresolved (LES) part of a variable obtained by Favre phasic-weighted decomposition
$''$	fluctuating (RANS) or unresolved (LES) part of a variable obtained by Favre mass-weighted decomposition
a	dry air
b	bulk viscosity
$\|_b$	Bottom face
$)_B$	Bottom node
c	collisional
C	Cross-terms
$)_C$	Central location
$\|_d$	Downwind face
$)_D$	Downstream location
$\|_e$	East face
$)_E$	East node
g	gas phase
Int	denotes an interface or all the interfaces
Int,i	denotes the interface between phase i and all the other phases

K	kinetic
L	Leonard terms
m	mixture
mol	“molecular” (i.e., not induced by turbulence)
nb	any cell face or any cell node
$\|_n$	North face
$)_N$	North node
$)_P$	Central node
R	Reynolds terms
s	solid phase
$\|_s$	South face
$)_S$	South node
SG	induced by the subgrid and/or referred to a LES model
t	relative to time
$\|_t$	Top face
$)_T$	Top node
tur	induced by turbulence and/or referred to a RANS model
tur/SG	any generic term either calculated by a RANS model (turbulence) or by a LES model (subgrid)
k^{th}	some X-, Y-, Z-directions
x	X-direction (radial or horizontal) or relative to space
y	Y-direction (vertical)
$\|_u$	Upwind face
$)_U$	Upstream location
w	water vapor (steam)
$\|_w$	West face
$)_W$	West node

Acronyms

BI-CGSTAB	biorthogonal-conjugate gradient stable method
CV	control volume
DCM	differed correction method
DOE	US Department of Energy
dwf	downwind weighting factors
EOS	equation of state
FOU	first order upwinding
GMFIX	geophysical multiphase flow with interphase exchange
IMF	implicit multifield
LANL	Los Alamos National Laboratory
LES	large eddy simulation
LHS	left-hand side
MFIX	multiphase flow with interphase exchange
MUSCL	monotonic upstream-centered scheme for conservation law
NETL	National Energy Technology Laboratory
NVD	normalized variable diagram
ORNL	Oak Ridge National Laboratory
PDE	partial differential equation
PEA	partial elimination algorithm
RANS	Reynolds Averaged Navier-Stokes
RHS	right-hand side
SG	sub-grid
SGH	sub-grid heat (flux)
SGS	sub-grid stress (flux)
SIMPLE	semi-implicit for pressure linked equations
V&V	verification and validation

References

American Institute of Aeronautics and Astronautics AIAA (1998), Guide for the Verification and Validation of Computational Fluid Dynamics Simulations, *AIAA, G-077-1998,* Guide, pp.19, Reston, Virginia, USA.

Benyahia S., M. Syamlal, and T.J. O'Brien (2005), Evaluation of boundary conditions used to model dilute turbulent gas/solid flows in a pipe, *Powder Technology*, 156, 62-72.

Bird, R.B., W.E. Stewart, and E.N. Lightfoot (1960), Transport phenomena, pp. 780, *John Wiley & Sons,* New York.

Bird, R.B., R.C. Armstrong, and O. Hassager (1977), Dynamics of polymeric liquids. *Volume 1. Fluid Mechanics*, pp. 470, *John Wiley and Sons,* New York.

Dartevelle S. (2004), Numerical modeling of geophysical granular flows: 1. A comprehensive approach to granular rheologies and geophysical multiphase flows, *G-cubed*, 5, Q08003, doi:10.1029/2003GC000636.

Dartevelle S., W.I Rose, J. Stix, K. Kelfoun, and J.W. Vallance (2004), Numerical modeling of geophysical granular flows: 2. Computer simulations of plinian clouds and pyroclastic flows and surges, *G-cubed*, 5, Q08004, doi:10.1029/2003GC000637.

Dartevelle S. (2005), Comprehensive Approaches to Multiphase Flows in Geophysics. Application to non-isothermal, non homogenous, unsteady, large-scale, turbulent dusty clouds. I. Basic RANS and LES Navier-Stokes equations, *Los Alamos National Laboratory, LA-14228, pp.51,* Los Alamos, New Mexico.

Dartevelle S. and G.A. Valentine (2005), Early-time multiphase interactions between basaltic magma and underground repository openings at the proposed Yucca Mountain radioactive waste repository, *Geophysical Research Letters*, 32, L22311, doi:10.1029/2005GL024172.

Dartevelle S. (2006a), Geophysical Multiphase Flow with Interphase eXchanges. Hydrodynamic and Thermodynamic Models and Numerical Techniques. Version GMFIX-1.62, pp. 62, Design Document Attachment 1, *U.S. Department of Energy, Office of Repository Development, 11192-DD-1.62-00*.

Dartevelle S. (2006b), GMFIX, Geophysical Multiphase Flow with Interphase eXchanges. Manual. Version GMFIX-1.62, pp. 62, Design Document Attachment 2, *U.S. Department of Energy, Office of Repository Development, 11192-DD-1.62-00*.

Dartevelle S. and G.A. Valentine (2007), Transient multiphase processes during the explosive eruption of basal through a geothermal borehole (Námafjall, Iceland, 1977) and implications for natural volcanic flows, *Los Alamos National Laboratory, LA-UR-07-1414*, Los Alamos, New Mexico.

Dobran F., A. Neri, and G. Macedonio (1993), Numerical simulations of collapsing volcanic columns, *J. Geophy. Res.*, 98, 4231-4259.

Drew, D.A. (1983), Mathematical modeling of two-phase flow, *Ann. Rev. Fluid Mech.*, 15, 261–291.

Drew, D.A., and S.L. Passman (1999), Theory of multicomponent fluids, pp. 308, *Springer, New York*.

Druitt T.H. (1998), Pyroclastic density currents, *in* The physics of explosive volcanic eruptions (J.S. Gilbert and R.S.J. Sparks, eds.), *Geol. Soc.*, 145, 145-182, Special Publications, London.

Esposti, O.T., A. Neri, M. Todesco, and G. Macedonio (2002), Pyroclastic flow hazard assessment at Vesuvius (Italy) by using numerical modeling. I. Analysis of flow variables, *Bull. Volcanol.*, 64, 178-191, doi:10.1007/s00445-001-0190-1.

Favre, A. (1965), Equations des gaz turbulents compressibles, *J. Mécaniques*, 4, 361–390.

Ferschneider G. and P. Mege (2002), Dilute gas-solid flow in a riser, *Chem. Eng. J.*, 87, 41-48.

Ferziger, J.H. (1997), Large eddy simulation: an introduction and perspective (Lecture 2), *in* New tools in turbulence modeling (O. Metais and J. Ferziger, eds.), 29–47, Les Houches School, May 1996, *Les Editions de Physique (Les Ulis, France) & Springer-Verlag (Berlin).*

Galdi, G.P. (1994), An introduction to the mathematical theory of the Navier-Stokes equations, Volume I. Linearized steady problems, pp. 450, *Springer-Verlag*, New York.

Gatski, T.B. (1997), Modeling compressibility effects on turbulence (Lecture 4), *in* New tools in turbulence modeling (O. Metais and J. Ferziger, eds.), 73–104, Les Houches School, May 1996, *Les Editions de Physique (Les Ulis, France) & Springer-Verlag (Berlin).*

Guenther, C., and M. Syamlal (2001), The effects of numerical diffusion on simulation of isolated bubbles in a gas-solid fluidized bed, *Powder Technology*, 116, 142-154.

Harlow F.H. and A. Amsden (1975), Numerical calculation of multiphase flow, *J. Comput. Phys.*, 17, 19-52.

Hishida K., K. Takemoto, and M. Maeda (1987), Turbulence characteristics of gas-solids two-phase confined jet (effect of particle density), *Japanese J. Multiphase Flow*, 1, 56-68.

Ishii, M. (1975), Thermo-fluid dynamic theory of two-phase flow, pp. 248, *Eyrolles*.

Kashiwa, B.A (2001), A multifield model and method for fluid-structure interaction dynamics, pp. 61, *Los Alamos National Laboratory LA-UR-01-1136*, Los Alamos, New Mexico.

Kieffer, S.W. and B. Sturtevant (1984), Laboratory studies of volcanic jets, *J. Geophy. Res.*, 89, 8253-8268.

Ladenburg, R., C.C. van Voorhis, and J. Winckler (1949), Interferometric studies of faster than sound phenomena. Part II. Analysis of supersonic air jets, *Physical Review*, 76, 662-677.

Lewis, C.H. Jr. and D.J. Carlson (1964), Normal shock location in underexpanded gas and gas-particle jets, *AIAA Journal*, 2, 776-777.

Leonard, B.P., and S. Mokhtari (1990), Beyond first-order upwinding: the ultra-sharp alternative for non oscillatory steady-state simulation of convection, *Int. J. Num. Meth. Eng.*, 30, 729-766.

Lhuillier, D. (1996), The macroscopic modeling of multiphase mixture, *in* Flows of particles in suspensions (U. Schaflinger ed.), 39–91, *Springler-Verlag, Wien, New York.*

Neri, A., T.E. Ongaro, G. Macedonio, and D. Gidaspow (2003), Multiparticle simulation of collapsing volcanic pyroclastic flow, *J. Geophys. Res.*, 108, 2202, doi:10.1029/2001JB000508.

Oberhuber, J.M., M. Herzog, H.-F. Graf, K. Schwanke (1998), Volcanic plume simulation on large scales, *J. Volcanol. Geotherm. Res.*, 87, 29-53.

O'Rourke, P.J., D.C. Haworth, and R. Ranganathan (1998), Three-dimensional computational fluid dynamic, *Los Alamos National Laboratory, LA-13427-MS.*

Pannala, S., E. D'Azevedo, M. Syamlal, T. O'Brien (2003), Hybrid (OpenMP and MPI) Parallelization of MFIX: a multiphase CFD code for modeling fluidized beds, *Proceedings of ACM SAC 2003*, Melbourne, Florida.

Patankar, S. (1980), Numerical heat transfer and fluid flow, pp. 197, *Hemisphere Publishing, New-York.*

Patankar, S., K.C. Karki, and K.M. Kelkar (1998), Finite volume method, *in The Handbook of Fluid Dynamics*, R.W. Johnson ed., 27-1-27-26, *CRC Press, Boca Raton*.

Rivard, W.C. and M.D. Torrey (1979), THREED: An extension of the K-FIX code for three-dimensional calculations, *Los Alamos National Laboratory, LA-NUREG-6623 Suppl. II*.

Sagaut, P. (1998), Large eddy simulation for incompressible flows. An introduction, 2nd ed.., pp. 426, *Springer-Verlag, Berlin*.

Simonin, O. (1996), Continuum modeling of dispersed two-phase flows. Combustion and turbulence in two-phase flows, Von Karman Institute of Fluid Dynamics, *VKI Lecture Series*, pp.1-47, Belgium, Rhodes-St-Geneses.

Sod, G.A. (1978), A survey of several finite difference methods for system of nonlinear hyperbolic conservation laws, *J. Comput. Phys.*, 27, 1-31.

Spalding, D.B. (1981), Numerical computation of multiphase fluid flow and heat transfer, *in Numerical computation of multiphase flows*, J.M. Buchlin and D.B. Spalding (eds.), Lecture Series 1981-2, *von Karmán Institute for Fluid Dynamics, Rhode-Saint-Genèse, Belgium*.

Spalding, D.B. (1983), Developments in the IPSA procedure for numerical computation of Multiphase-flow phenomena with interphase slip, unequal, temperature, etc., *in Numerical properties and methodologies in heat transfer, Proc. 2nd National Symp.*, T.M. Shih (ed.), 421-436, *Hemisphere Publishing Corp., Washington*.

Suzuki, Y.J., T. Koyaguchi, M. Ogawa, and I. Hachisu (2005), A numerical study of turbulent mixing in eruption clouds using a three-dimensional fluid dynamics model, *J. Geophy. Res.*, 110, B08201, doi:10.1029/2004JB003460.

Sweby, P.K. (1984), High-resolution schemes using flux limiters for hyperbolic conservation laws, *SIAM J. Numer. Anal.*, 21, 995-1011.

Syamlal, M., W. Rogers, and T.J. O'Brien (1993), MFIX documentation. Theory Guide, pp. 49, *U.S. Dept. of Energy*, DOE/METC-94/1004, DE94000097.

Syamlal, M. (1998), MFIX documentation. Numerical Technique, pp. 80, *U.S. Dept. of Energy*, DOE/MC/31346-5824, DE98002029.

Todesco, M., A. Neri, T. Esposti O., P Papale, G. Macedonio, R. Santacroce, and A. Longo (2002), Pyroclastic flow hazard assessment at Vesuvius (Italy) by using numerical modeling. I. Large-scale dynamics, *Bull. Volcanol.*, 64, 155-177, doi:10.1007/s00445-001-0189-7.

Toro, E.F. (1999), Riemann solvers and numerical methods for fluid dynamics, A practical introduction, 2nd ed., pp. 624, *Springer-Verlag, Berlin*.

Valentine, G.A. and K.H. Wohletz (1989), Numerical models of Plinian eruption columns and pyroclastic flows, *J. Geophys. Res.*, 94, 1867-1887.

Valentine, G.A., K.H. Wohletz, and S.W. Kieffer (1991), Sources of unsteady column dynamics in pyroclastic flow eruptions, *J. Geophys. Res.*, 93, 21887-21892.

Valentine, G.A. (1998), Eruption column physics, *in From Magma to Tephra: Modeling physical processes of explosive volcanic eruptions* (A. Freundt and M. Rosi, eds.), 91-138, Elsevier Science.

Veynante, D., and T. Poinsot (1997), Reynolds averaged and large eddy simulation modeling for turbulent combustion (Lecture 5), *in* New tools in turbulence modeling (O. Metais and J. Ferziger, eds.), 105–140, Les Houches School, May 1996, *Les Editions de Physique (Les Ulis, France) & Springer-Verlag (Berlin).*

Viollet, P.L., O. Simonin, J. Olive, and J.P. Minier (1992), Modeling turbulent two-phase flows in industrial equipments, *in Computational Methods in Applied Sciences* (C. Hirsch, ed.), Elsevier science.

van der Vorst, H.A. (1992), BI-CGSTAB: A fast and smoothly converging variant of BI-CG for the solution of non-symmetric linear systems, *SIAM J. Sci. Stat. Comput*., 13, 631-644.

van Leer, B. (1979), Towards the ultimate conservative difference scheme. V. A second-order sequel to Godunov's method, *J. Comput. Physics*, 32, 101-136.

Wohletz, K.H., T.R. McGetchin, M.T. Standford II, and E.M. Jones (1984), Hydrodynamics aspects of caldera-forming eruptions: Numerical models, *J. Geophys. Res.*, 89, 8269-8286.


Los Alamos
NATIONAL LABORATORY
EST. 1943